POLITECNICO DI MILANO

SCHOOL OF INDUSTRIAL AND INFORMATION ENGINEERING

DEPARTMENT OF ELECTRONICS, INFORMATION AND BIOENGINEERING

Master of Science in Biomedical Engineering

COMPARATIVE ANALYSIS OF CBCT RECONSTRUCTION METHODS: EVALUATION OF CLINICAL PRACTICE AT CNAO AND INVESTIGATIONS ON IMAGE QUALITY IMPROVEMENT

Supervisor: Guido BARONI, PhD

Co-supervisor: Chiara PAGANELLI, PhD

Master Thesis of

Samantha SALSANO

ID: 876408

ACADEMIC YEAR 2017 – 2018

I. INDEX

II. LIST OF FIGURES

III. LIST OF TABLES

SOMMARIO

La radioterapia è una pratica clinica che utilizza radiazioni ionizzanti per il trattamento di lesioni tumorali, sfruttando la capacità di tali radiazioni di danneggiare il DNA delle cellule bersaglio in maniera irreparabile e impedire così che proliferino. L'efficacia di questa tecnica risiede nella capacità di rilasciare la dose di radiazione sufficiente a garantire un controllo locale del tessuto tumorale, senza danneggiare i tessuti sani e gli organi a rischio circostanti. Nella radioterapia convenzionale le radiazioni utilizzate sono i fotoni, che mostrano un decadimento esponenziale dell'energia rilasciata in funzione della profondità dei tessuti attraversati. Una tecnica di radioterapia avanzata che negli ultimi anni sta acquistando sempre più importanza è l'adroterapia, una forma di trattamento che impiega particelle cariche – anche dette adroni – al posto dei fotoni. A differenza dei fotoni, le particelle cariche (come i protoni, o gli ioni carbonio) rilasciano una piccola quantità di energia a livello degli strati più superficiali di tessuto, per poi depositare una dose molto elevata in corrispondenza di una determinata profondità – che corrisponde al picco di Bragg – la quale può essere regolata agendo sull'energia iniziale del fascio, e a cui non segue nessuna ulteriore dose somministrata agli strati più profondi. Tali proprietà intrinseche degli adroni permettono di conformare la dose al tumore con maggiore precisione, consentendo la formulazione di piani terapeutici tali da garantire la riduzione dell'esposizione di strutture critiche vicine al target dell'irradiazione: questo li rende elettivi per la cura di alcune specifiche tipologie di tumori, ad esempio i tumori profondi e quelli radio-resistenti. Tuttavia, comporta la necessità di una maggiore attenzione nell'allineamento tra il fascio e il bersaglio, poiché un errore di posizionamento in questo caso provoca un danno maggiore al paziente. La maggiore selettività degli adroni non può essere pienamente sfruttata senza un'elevata accuratezza nell'individuazione del target.

Per rispondere a tale necessità, è uso comune l'adozione di sistemi di imaging in-room per la verifica quotidiana del corretto posizionamento del paziente. Infatti, un trattamento adroterapico è costituito da più sedute, o frazioni, somministrate in giorni diversi, in numero variabile. Il razionale della radioterapia guidata dalle immagini (Image-Guided Radiotherapy, IGRT) è quindi correggere gli errori di posizionamento prima di ogni frazione per riprodurre il più accuratamente possibile il piano di trattamento. In Italia il

Centro Nazionale di Adroterapia Oncologica (CNAO), situato a Pavia, rappresenta un centro di eccellenza per il trattamento con adroni. Inaugurato nel 2010, oggi è marcato come dispositivo CE, ha trattato più di 1600 pazienti ed è ancora uno dei pochi centri in Europa cosiddetti "duali", ovvero che somministrano trattamenti sia con fasci di protoni che ioni carbonio. A CNAO la verifica del setup del paziente viene effettuata attraverso un sistema di posizionamento che comprende un lettino a 6 gradi di libertà, un sistema di tracking ottico a infrarossi che, se necessario, calcola un vettore di correzione applicato al paziente tramite il lettino, e un secondo sistema di verifica del posizionamento basato su imaging Cone-Beam CT (CBCT), che calcola un secondo vettore di correzione basato sulla registrazione dell'anatomia ossea rispetto alla CT di pianificazione.

Tra i sistemi in-room, la CBCT è una tecnica di imaging tomografico con geometria di acquisizione conica, basata cioè sull'acquisizione di proiezioni bidimensionali a diverse angolazioni per mezzo di un fascio conico, le quali permettono la ricostruzione di un volume tridimensionale mediante appropriati algoritmi. Il metodo di ricostruzione più comunemente impiegato è l'algoritmo Feldkamp-Davis-Kress (FDK) (Feldkamp et al., 1984), che è l'estensione al caso tridimensionale del metodo di Filtered Back-Projection (FBP) utilizzato comunemente per ricostruire slice 2D nella CT convenzionale. Tale metodo non è esatto, poiché si basa su alcune approssimazioni, ma per gli angoli di apertura del raggio comunemente impiegati in clinica tali differenze sono piccole e spesso accettabili. Tuttavia, ci sono molte questioni ancora da risolvere, soprattutto per quanto riguarda la qualità della CBCT: spesso sono presenti artefatti che possono corrompere l'immagine, inoltre tavolta per ridurre la dose somministrata al paziente viene ridotto il numero di proiezioni acquisite e questo complica la ricostruzione. L'interesse della ricerca si sta muovendo verso metodi di ricostruzione alternativi per cercare di compensare i limiti e migliorare la qualità della ricostruzione 3D di CBCT.

Un altro approccio per migliorare la qualità dell'immagine ricostruita è agire sulle singole proiezioni attraverso un'elaborazione a posteriori. In particolare, una strategia che ha suscitato particolare interesse è utilizzare la CT di pianificazione come informazione a priori per correggere le proiezioni cone-beam. Un limite di questo approccio risiede nell'accuratezza della registrazione non-rigida che deve essere effettuata fra CT e CBCT, che risulta essere limitata in presenza di grandi variazioni anatomo-patologiche, come per

esempio nel distretto pelvico, dove sono presenti organi come il retto o la vescica che subiscono variazioni importanti in funzione del loro riempimento.

Lo scopo di questo lavoro di tesi consiste nel valutare l'algoritmo di ricostruzione attualmente implementato nella pratica clinica del Centro, e confrontarlo con alcuni algoritmi alternativi per testare il comportamento di questi ultimi sui dati CNAO. In secondo luogo, viene testato un metodo di correzione delle proiezioni CBCT a posteriori presente in letteratura per investigarne le potenziali applicazioni pratiche.

Le valutazioni sono state fatte a posteriori su dati acquisiti a CNAO, dapprima su fantoccio e poi su dati appartenenti a pazienti che sono stati trattati al Centro. Il database si compone di un set di proiezioni CBCT appartenenti al Catphan© 600, e dei dati appartenenti a 13 pazienti, che comprendono una scansione CT di pianificazione e un set di proiezioni CBCT. Tutti i pazienti sono stati trattati in distretti extra-cranici, in particolare 12 di questi in distretto pelvico, e uno in distretto toracico. Le CT sono state acquisite con uno scanner convenzionale (Siemens SOMATOM Sensation Open CT scanner), e il sistema di imaging CBCT utilizzato è composto da un braccio a 6 gradi di libertà su cui è stato installato un C-arm, il quale integra una sorgente a raggi X nell'ordine dei kV ad uso diagnostico (Varian A-277) e un detettore planare (Varian PaxScan 4030D). Il C-arm ruota attorno al gantry con un angolo di 220° e acquisisce circa 600 proiezioni che poi vengono elaborate per ottenere la ricostruzione tomografica.

Nella prima fase del lavoro sono state valutate le performance del metodo implementato attualmente a CNAO – l'algoritmo FDK – e di quattro metodi alternativi, tutti iterativi: (i) il metodo SART (Simultaneous Algebraic Reconstruction Technique), (ii) la sua variante OS-SART (Ordered Subset SART), e il metodo ADMM (Alternating Direction Method of Multipliers) (iii) sia con regolarizzazione Total Variation (ADMM–TV), e (iv) sia con regolarizzazione Wavelet (ADMM–W). Per ciascuna ricostruzione CBCT sono state valutate su fantoccio diverse caratteristiche: Signal-Noise Ratio (SNR), Contrast-Noise Ratio (CNR), non-uniformità di campo, risoluzione spaziale. In seguito, l'analisi è proseguita con i dati dei pazienti. Per i pazienti si è effettuato un confronto tra la CT di pianificazione e ciascuna delle ricostruzioni CBCT, utilizzando tre metriche principali: la Mutua Informazione (MI), la sua versione normalizzata (Normalised-MI, NMI), e il coefficiente di correlazione di Pearson (PCC). Tali indici sono tra quelli che si sono

dimostrati più informativi nella valutazione delle immagini CBCT cosiddetta “full reference”, ovvero in quei casi in cui si utilizza un’immagine di riferimento per valutare la qualità della ricostruzione, in questo caso la CT di pianificazione. Il PCC è stato valutato, oltre che a livello globale, anche all’interno di alcuni organi di interesse, come la regione da irradiare (Planned Target Volume, PTV), e per i pazienti pelvici anche vescica, retto e sigma, sulla base del suggerimento di clinici esperti. Sia gli indici globali che gli indici calcolati a livello degli organi di interesse non hanno mostrato miglioramenti significativi nei metodi iterativi rispetto al metodo FDK attualmente implementato, anche se i risultati a livello dei tessuti molli hanno suggerito che regolare in maniera appropriata i parametri dei metodi ADMM – regolazione che rappresenta di per sè un ambito di ricerca aperto – potrebbe restituire un contrasto migliore in corrispondenza di tali regioni.

Nella seconda parte del lavoro è stato testato un metodo di correzione delle proiezioni CBCT a posteriori che sfrutta la CT di pianificazione come informazione a priori, presente in letteratura. Il metodo sfrutta la scansione CT di pianificazione, precedentemente registrata sulla CBCT, per generare delle proiezioni virtuali secondo la stessa geometria della CBCT corrispondente, in modo da ottenere un set di coppie di proiezioni corrispondenti. L’ipotesi alla base del metodo, che si propone di correggere unicamente gli artefatti dovuti allo scattering, è che le differenze tra una proiezione CBCT reale e la sua proiezione CT virtuale corrispondente siano dovute unicamente a tale fenomeno, e che quindi la componente di scattering possa essere calcolata come una versione opportunamente scalata e “smoothed” della differenza tra le due proiezioni. Tale componente di errore viene quindi sottratta dalle proiezioni originali, e le proiezioni così ottenute vengono ricostruite per ottenere un volume “corretto”. I risultati di questa seconda parte rappresentano delle conclusioni preliminari, dal momento che tutti gli step del metodo devono essere ulteriormente analizzati e ottimizzati sulla base dei dispositivi utilizzati, a partire dalla qualità della registrazione deformabile tra CT e CBCT, fino alla necessità di stabilire una calibrazione affidabile tra i valori CBCT e i valori Hounsfield Unit (HU) riportati nella CT. Inoltre, per rivalutare le ricostruzioni corrette sono stati impiegati indici di similarità analoghi a quelli considerati nella prima parte, i quali per loro natura sono caratterizzati da un bias. Infatti, utilizzare la CT come informazione a priori comporta di per sè con alta probabilità un incremento di tali metriche, e la ricerca di un indice affidabile e informativo in questo senso rappresenta un problema aperto. Tuttavia, i

risultati preliminari sono promettenti, e sembrano mostrare che il metodo, opportunamente sviluppato, potrebbe rappresentare un valido aiuto nella pratica clinica di CNAO.

In conclusione, nessuno dei metodi iterativi si è dimostrato significativamente migliore di quello attualmente impiegato a CNAO, sebbene le ricostruzioni siano fortemente dipendenti da artefatti presenti a priori sulle proiezioni stesse. Un ulteriore sviluppo potrebbe essere rivolto ad indagare le cause di tali artefatti e possibili soluzioni per evitare la loro presenza. Si sottolinea anche l'esigenza di stabilire metriche di qualità della ricostruzione che non abbiano un'immagine di riferimento. Il metodo di correzione delle proiezioni risulta essere promettente, ma è necessario mettere a punto l'intero processo, attraverso una calibrazione della conversione da valori CBCT a HU, che in questo momento è assente, l'ottimizzazione degli algoritmi di deformable registration, e la regolazione dei parametri che guidano la correzione. Tale algoritmo di correzione potrebbe, in questo modo, migliorare in maniera significativa la qualità della ricostruzione.

SUMMARY

Radiotherapy is a clinical treatment that uses ionising radiation to treat cancer, exploiting the ability of such radiation to irreparably damage the DNA of the target cells and thus prevent them from proliferating. The strength of this technique lies in the ability to release the radiation dose sufficient to guarantee local control of the tumour, without damaging healthy tissues and organs at risk. In conventional radiotherapy photons are used, which show an exponential decay of the energy released as a function of the depth. An advanced radiotherapy technique that is gaining more and more importance in recent years is hadrontherapy, a treatment that uses charged particles - also called hadrons - instead of photons. Unlike photons, charged particles (such as protons, or carbon ions) release a small amount of energy at the level of the most superficial layers of tissue, to then deposit a very high dose at a given depth - which corresponds to Bragg peak - which can be regulated by acting on the initial energy of the beam, followed by no further dose delivery. These intrinsic properties of hadrons lead to greater precision in dose conformality, allowing the formulation of therapeutic plans that guarantee the reduction in exposure of critical structures close to the irradiation target: this makes them elective for treating specific types of tumours, such as deep tumours and radio-resistant tumours. However, greater attention in the alignment between the beam and the target is here fundamental, since a positioning error causes higher damage to the patient. The greater selectivity of hadrons cannot be fully exploited without increasing accuracy in target identification.

To meet this need, it is common to use in-room imaging systems for daily verification of correct patient positioning. In fact, an adrotherapeutic treatment consists of several sessions, or fractions, administered on different days, in a variable number. The rationale of Image-Guided Radiotherapy (IGRT) is therefore to correct positioning errors before each fraction, to reproduce the treatment plan as accurately as possible.

In Italy, the National Centre for Oncological Hadrontherapy (CNAO), located in Pavia, represents a centre of excellence for treatment with hadrons. Inaugurated in 2010, today it is marked as a CE device, it has treated more than 1600 patients and it is still one of the few so-called "dual" centres in Europe, i.e. in performs treatments both with protons and

carbon ions. At CNAO the verification of the patient's daily setup is carried out through a positioning system that includes a 6-degrees of freedom couch, an infrared optical tracking system that, if necessary, calculates a correction vector applied to the patient through the couch, and a second verification system based on Cone-Beam CT (CBCT) imaging, which calculates a second correction vector based on the registration of bony anatomy with respect to the planning CT.

Among the in-room systems, CBCT is a tomographic imaging technique based on the acquisition of two-dimensional projections at different angles by means of a conical beam, which allow the reconstruction of a three-dimensional volume using appropriate algorithms. The most commonly used reconstruction method is the Feldkamp-Davis-Kress algorithm (FDK) (Feldkamp et al., 1984), which is the extension to the three-dimensional case of the Filtered Back-Projection (FBP) method commonly used to reconstruct 2D slices in conventional CT. This method is not exact, since it is based on some approximations, but for the opening angles commonly used in clinics these differences are small and often acceptable. However, there are many issues still to be solved, especially with regard to the quality of CBCT: artefacts that can corrupt the image are often present, and moreover, to reduce the dose administered to the patient the number of acquired projections is sometimes reduced and this complicates the reconstruction. The interest of research is moving towards alternative reconstruction methods, trying to compensate for the limits of the 3D CBCT reconstruction and to improve the image quality.

Another approach to improve the quality of the reconstructed image is to act on the projections through a post-processing technique. In particular, a strategy that has aroused particular interest is to use the planning CT as a priori information to correct cone-beam projections. A limitation of this approach lies in the accuracy of the non-rigid registration that must be performed between CT and CBCT, which appears to be limited in presence of large anatomo-pathological changes, as in the pelvic district, where there are organs such as the rectum or bladder that undergo important changes as a function of their filling.

The purpose of this thesis work is to evaluate the reconstruction algorithm currently implemented and clinically used in the Centre, and to compare it with some alternative algorithms to test the behaviour of the latter on CNAO data. Secondly, a method for a

posteriori correction of CBCT projections present in the literature is tested to investigate its potential practical applications.

Evaluations were made *a posteriori* on data acquired at CNAO, first on a phantom and then on patients' data. The database consists of a set of CBCT projections belonging to Catphan © 600, and data belonging to 13 patients, which include a planning CT scan and a set of CBCT projections. All patients were treated in extra-cranial districts, in particular 12 of these in the pelvic district, and one in the thoracic district (patient P7). The CTs were acquired with a conventional scanner (Siemens SOMATOM Sensation Open CT scanner), and the CBCT imaging system is composed of a 6-degree freedom robot on which a C-arm is installed. The C-arm integrates a kV X-ray source for diagnostic purposes (Varian A-277) and a planar detector (Varian PaxScan 4030D). The C-arm rotates around the gantry covering a 220° angle and it acquires about 600 projections that are then processed to obtain the tomographic reconstruction.

In the first phase of the work the performances of the method currently implemented at CNAO – the FDK algorithm – and of four alternative methods, all iterative, were evaluated: (i) the SART (Simultaneous Algebraic Reconstruction Technique) method, (ii) its variant OS-SART (Ordered Subset SART), and the ADMM method (Alternating Direction Method of Multipliers) (iii) both with Total Variation regularization (ADMM – TV), and (iv) and with Wavelet regularization (ADMM – W). For each CBCT reconstruction different characteristics have been evaluated on the phantom: Signal-Noise Ratio (SNR), Contrast-Noise Ratio (CNR), field non-uniformity, spatial resolution. The analysis continued with patient data. For all the patients a comparison was made between the planning CT and each of the CBCT reconstructions, using three main metrics: Mutual Information (MI), its normalised version (Normalised-MI, NMI), and the Pearson correlation coefficient (PCC). These indexes have proved to be more informative in the so-called "full reference" evaluation of the CBCT images, i.e. when a reference image is used to assess the quality of the reconstruction, in this case the planning CT. The PCC has been evaluated, as well as globally, also within certain organs of interest, such as the region to be irradiated (Planned Target Volume, PTV), and for pelvic patients also bladder, rectum and sigma, relying on the suggestion of expert clinicians. Both the global indices and the indices calculated at the level of the organs of interest showed no significant improvements in the iterative methods compared to the currently implemented FDK method, although the

results at the level of soft tissues suggested that properly adjusting ADMM methods parameters – regulation that represents an open field of research itself – could return a better contrast in such regions.

In the second part of the work a CBCT projection correction method that uses the planning CT as a priori information, present in literature, was tested. The method uses the planning CT scan, previously registered on the CBCT, to generate virtual projections according to the same geometry as the corresponding CBCT, in order to obtain a set of pairs of corresponding projections. The hypothesis underlying the method, which aims to correct only the artefacts due to scattering, is that the differences between a real CBCT projection and its corresponding virtual CT projection are due solely to this phenomenon, and that therefore the scattering component can be calculated as a properly scaled and smoothed version of the difference between the two projections. This error is then subtracted from the original projections, and the projections thus obtained are reconstructed to finally obtain a "corrected" volume. The results of this second part are preliminary, since all the steps of the method must be further analysed and optimised on the basis of the devices used, starting from the quality of the deformable registration between CT and CBCT, until the need to establish a reliable calibration between the CBCT values and the Hounsfield Unit (HU) values reported in the CT. Furthermore, similarity metrics considered in the first part have been used to also reassess the corrected reconstructions, but by their nature these are characterized by a bias. In fact, using CT as a priori information obviously leads with a high probability to an increase of such metrics, and finding a reliable and informative index represents an open problem. However, the preliminary results are promising, and seem to show that an appropriately developed method could be a valid aid in the clinical practice of CNAO.

In conclusion, none of the iterative methods proved to be significantly better than the one currently used at CNAO, although the reconstructions are strongly dependent on a priori artefacts that are present on the projections themselves. A further development could be aimed at investigating the causes of such artefacts, and possible solutions to avoid them. We underline also the need to establish reconstruction quality metrics that do not refer to another image. The correction method for the projections turns out to be promising, but it is necessary to accurately tune the whole process, through a calibration of the conversion from CBCT values to HU, that is absent at present, the optimisation of the deformable

registration algorithms, and the adjustment of parameters that guide the correction. This correction algorithm could, in this way, significantly improve the quality of the reconstruction.

1. RADIOTHERAPY AND HADRONTHERAPY

Hadrontherapy, also known as "particle therapy", is a specific type of oncological radiotherapy – i.e. the medical use of ionising radiation to treat cancer – which makes use of hadrons such as protons or heavy ions (e. g. carbon ions) to treat cancer. The appropriate application of hadrontherapy has led to better dose deposition with fewer adverse effects when compared with the ones of X-rays used in conventional radiotherapy. Thus, facilities for this clinical treatment are being built worldwide, despite the requirement for costly equipment.

Over the past decades, with an increasing number of applications all over the world, the number of new programs under development is constantly growing (Fig. 1).

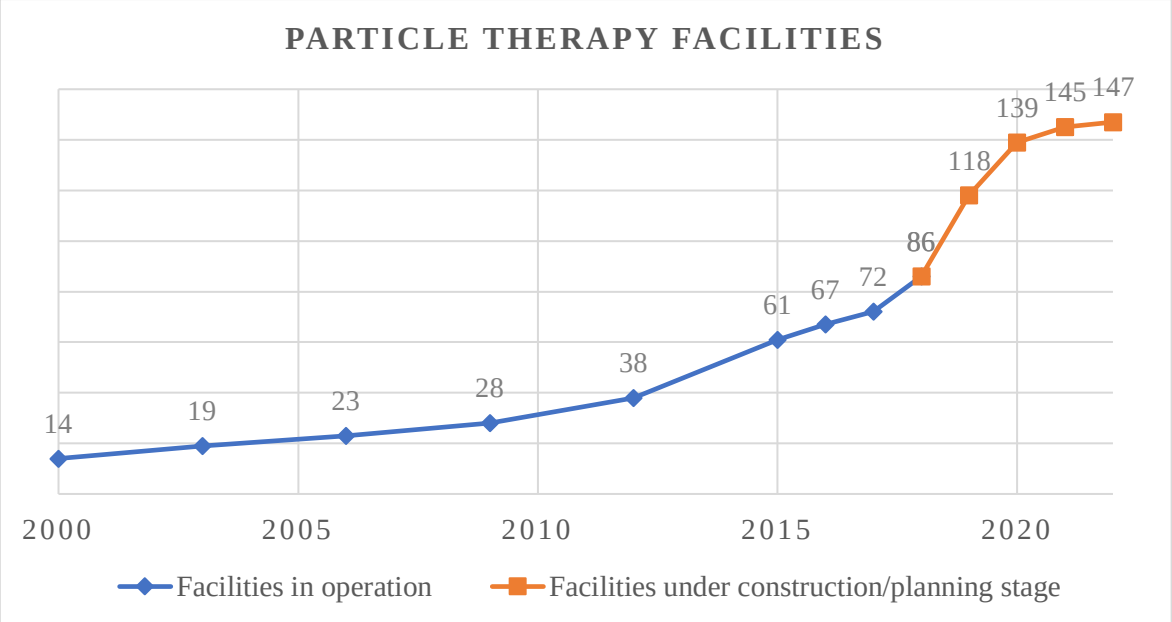

Figure 1. **Temporal evolution of the number of centres delivering charged-particle therapy to patients with cancer.** Updated February 2019. Source: www.ptcog.ch

The strength of hadrontherapy lies in the unique physical and radiobiological properties of these particles; they can penetrate the tissues with little diffusion and deposit the maximum energy just before stopping. This allows a precise definition of the specific region to be irradiated. The peaked shape of the hadron energy deposition is called Bragg peak. Unlike

X-ray irradiation, with charged particle therapy the energy deposited per unit track increases with depth, reaching a sharp and narrow maximum peak close to the end of the range.

Today, both protons and heavy ions (typically carbon) are used for irradiating tumours. Out of the approximately two-thirds of patients with cancer who are treated with radiotherapy, more than 80% receive X-rays and only about 0.8% receive radiation from high-energy charged particles, a proportion that is rapidly increasing (Jermann, 2015).

In Appendix 1 it is possible to see the updated list of centres currently in operation.

1.1 RADIOTHERAPY VS. HADRONTHERAPY: PHYSICAL ASPECTS

Hadrons are heavy charged particles. The large mass and acceleration applied gives each particle a specific momentum, that is mostly dissipated after traveling a defined distance, and then slowed down by interactions with the target, which causes a sharp rise in energy deposition at the end of the path of the particle, followed by no further dose delivery, which is referred to as the Bragg peak. This individual physical property provides superior dosimetric advantages over photons or electrons. Therefore, rather than traversing the target, protons are stopped at an energy-dependent depth in the target and have no exit dose, which completely spares the downstream normal tissue. Particle beams are generated by a cyclotron or synchrotron, and then accelerated to the desired target. Fig. 2 depicts the depth-dose distribution curves of particles vs. photon beam, demonstrating that, at the prescribed depth, the particle beam does not deliver a dose, whereas the photon beam does.

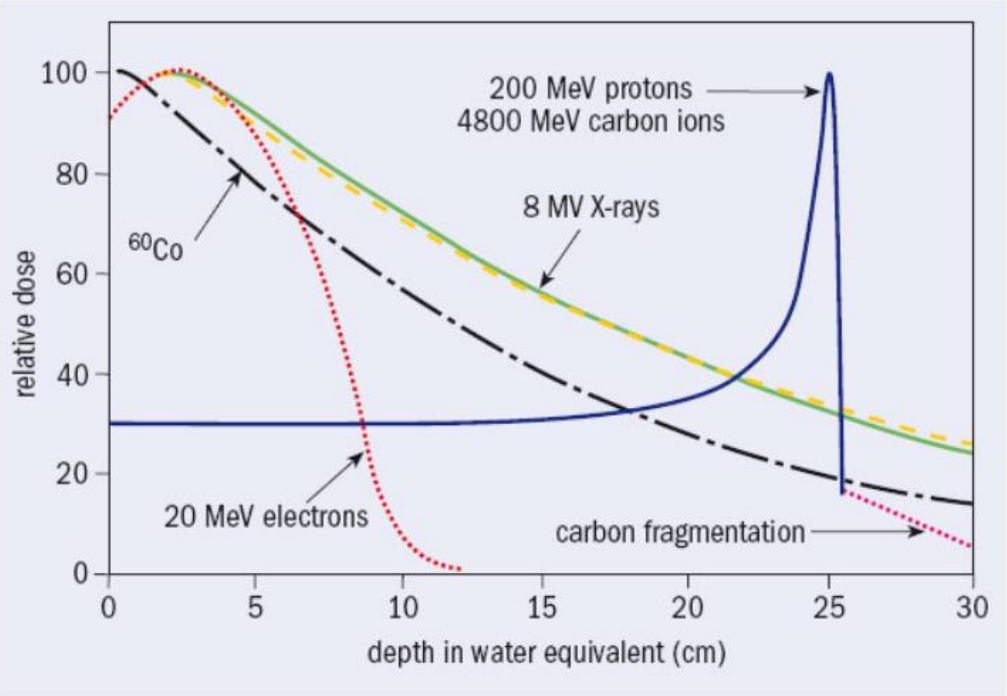

Figure 2. **Depth dependence of the deposited dose for different radiations.** Because of the Bragg peak it is said that the dose distribution is 'inverted' with respect to the almost exponential, and much less favourable, behaviour produced by X-rays. Source: Amaldi & Kraft, 2005.

1.2 RADIOTHERAPY VS. HADRONTHERAPY: BIOLOGICAL ASPECTS

The best patient-stratification strategies should be based on the potential biological advantages derived from physical dose distributions. The radiobiology of a response to charged particles is, indeed, different from that of X-rays (Durante et al., 2017).

In conventional radiotherapy, the effective dose is determined from multiplying the physical dose by the relative biological effectiveness (RBE). Therefore, the clinical and biological effect may differ when the physical dose remains constant and the radiation quality changes. The RBE is used to link the biological effect to a reference radiation:

$$RBE = \frac{D_{control}}{D_{test}}$$

In this equation $D_{control}$ is the physical dose of a known radiation modality (i.e. X-rays) and D_{test} is the physical dose of the radiation modality being investigated (Valentin, 2003), given the same amount of absorbed energy.

For external beam radiotherapy, which uses photons and electrons, the RBE is generally to be considered 1 (Jakel & Kramer, 2008, Paganetti, 2012).

Protons are light particles and their RBE is low, except at the end of the particle range in the tissue. The Linear Energy Transfer (LET) of protons, i.e. the energy deposited per unit track, is around 1 keV/µm in the entrance channel, similar to that of X-rays, and increases up to 2-6 keV/µm in the spread-out Bragg peak (SOBP) (Durante et al., 2017). In clinical practice, a fixed RBE value of 1.1 is used, therefore slightly different from that of conventional radiation, but RBE changes along the Bragg curve, and accelerated protons in the distal part of the pathway may have RBE over 1.65 (Coutrakon et al., 1997).

A substantial increase in RBE and in other effects of high-LET radiation in the tumour volume can be achieved using radiation from heavier ions as carbon ions, in which the LET reaches values close to the maximum level of effectiveness. For this reason, carbon ions are considered the most advanced ionising radiation tool for the treatment of radioresistant tumours. The dose distribution of carbon ions is slightly better than that of protons. In addition, carbon ions accelerated at therapeutic energies (200-400 MeV/n) have a LET in the entrance channel of 11-13 keV/µm, and a fairly high LET on the SOBP (40-90 keV/µm) (Durante et al., 2017). Even if a unique clinical RBE value shall still be specified (Karger & Peschke, 2018), such LETs differentiate the therapeutic properties of carbon ions from those of X-rays or protons.

1.3 HADRONTHERAPY: CURRENT NATIONAL AND INTERNATIONAL STATUS

The idea of using protons for cancer treatment was first proposed in 1946 by the physicist Robert Wilson (Wilson, 1946), who later became the founder and first director of the Fermi National Accelerator Laboratory (Fermilab) near Chicago. The first patients were treated in the 1950s in nuclear physics research facilities by means of non-dedicated accelerators. Initially, the clinical applications were limited to few parts of the body, as accelerators were not powerful enough to allow protons to penetrate deep in the tissues.

In the late 1970s improvements in accelerator technology, coupled with advances in medical imaging and computing, made proton therapy a viable option for routine medical

applications. However, it has only been since the beginning of the 1990s that proton facilities have been established in clinical settings, the first one being in Loma Linda, USA.

Although protons are used in several hospitals, the next step in radiation therapy is the use of carbon and other ions. These have some clear advantages even over protons in providing both a local control of very aggressive tumours and a lower acute or late toxicity, thus enhancing the quality of life during and after cancer treatment. Since the birth of hadrontherapy, more than 120,000 patients have been treated globally with hadrons, including 20,000 with carbon ions.

In Europe, the interest in hadrontherapy has been growing rapidly and the first dual ion (carbon and protons) clinical facility in Heidelberg, Germany started treating patients at the end of 2009.

Globally there is a huge momentum in particle therapy, especially treatment with protons. By 2020 it is expected there will be almost 100 centres around the world, with over 30 of these in Europe, as reported by the European Network for Light Ion Hadrontherapy (ENLIGHT, www.enlight.web.cern.ch). A brief recap of hadrontherapy history is reported in Fig. 3.

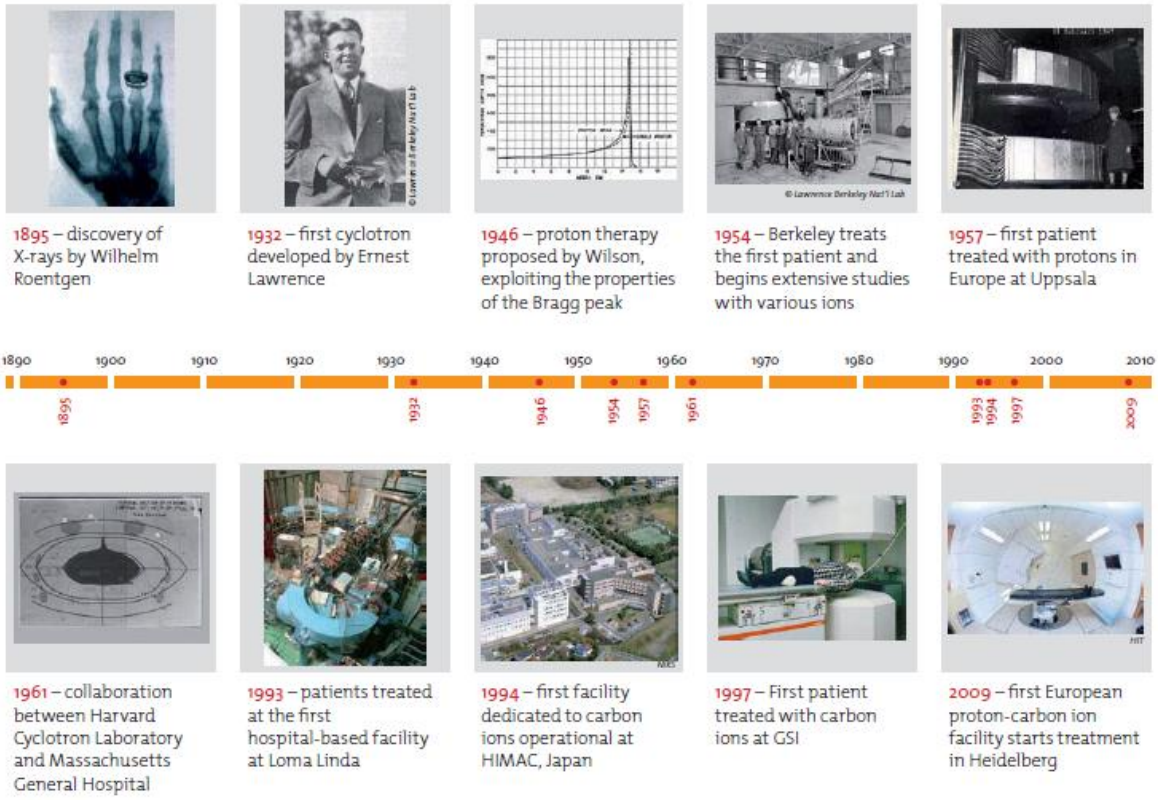

Figure 3. History of hadrontherapy. Source: www.enlight.web.cern.ch

The current state of hadrontherapy in the world shows a situation of strong expansion, with 86 operating centres as reported by the site of PTCOG (www.ptcog.ch), updated to February 2019. Most of these have protons available (80 in total, of which 31 in the USA, 27 in Europe, 14 in Japan and 8 in various parts of the world). Twelve centres provide carbon ions (6 in Japan, 4 in Europe and 2 in China). It should be remarked that six of these centres – Heidelberg, Pavia, Marburg, Wiener Neustadt, Shanghai and Hyogo – have "dual accelerators", which can accelerate both protons and carbon ions.

An impressive data concerns the exponential growth in the number of patients treated. At the end of 2007 they were 61.855 (53.818 with protons and 4.450 with carbon ions). At the end of 2017 the number had grown to 170.925 (149.345 with protons, 21.580 with carbon ions). This is due primarily to the greater availability of centres able to meet to a greater extent the growing demand for this particular form of radiotherapy. The trend is steadily increasing and obviously it is going to increase further, with the upcoming opening of new centres.

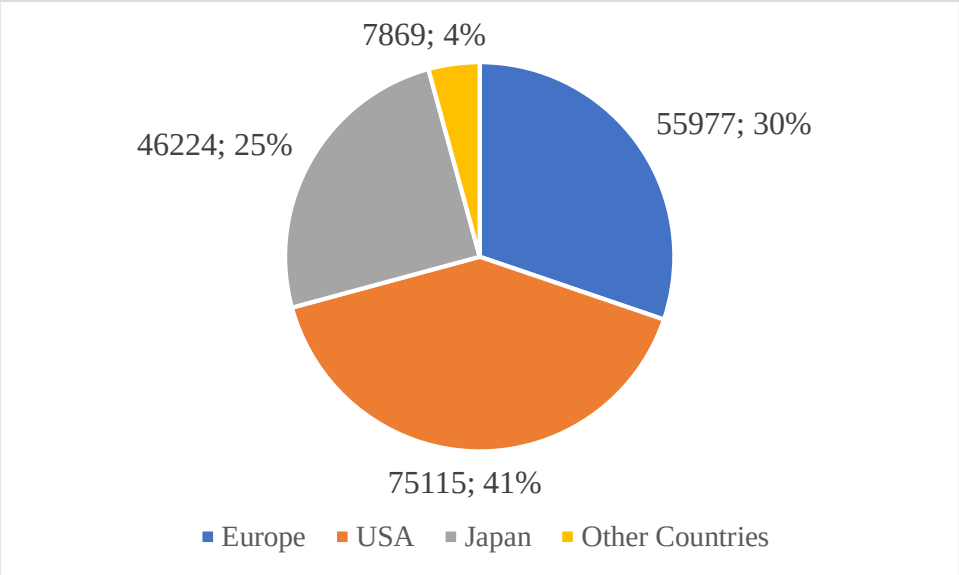

Figure 4. **Hadrontherapy patient's distribution in the world.** Updated February 2019. Source: www.ptcog.ch

1.4 CNAO: THE ITALIAN HADRONTHERAPY PROJECT

In Italy, the publication, in May 1991, of the report "For a centre of teletherapy with hadrons" signed by Ugo Amaldi and Giampiero Tosi (Amaldi & Tosi, 1991) started the history of the National Center for Oncological Hadrontherapy (CNAO) (Amaldi & Magrin, 2010).

In our own Country, the activity with protons has been underway in the INFN laboratories of the South for many years (Cuttone et al., 2011), although limited to ocular pathology, and more recently in the Centre of Trento. In this frame, CNAO completed the experimental phase and started in 2014 the patient's treatments within the National Health System. As reported on CNAO website (www.fondazionecnao.it), at the end of 2017, more than 1600 patients had been treated.

Presently, the centre is a CE labelled medical device and this unique qualification has been obtained through a long and strictly ruled experimental path.

1.5 Image-Guided Radiotherapy and Adaptive Radiotherapy: paradigms of clinical radiotherapy advancement

Central to the advances in radiotherapy delivery is the development of medical imaging technologies that provide the 3D contours of the volumes of interest, as the region to be irradiated or the organs at risk (OARs) located near the volume to treat that could suffer from radiation-induced toxicity.

However, the definition of tumour and OARs on a planning 3D image suffers from anatomical and pathological variations that occur during treatment delivery.

The rationale of Image-Guided Radiotherapy (IGRT) is therefore to reduce the irradiated volume by managing tumour motion and provide optimal treatment plans using images with the patient in the treatment position immediately prior to or during the treatment; in fact, an adrotherapeutic treatment is typically composed by many sessions, or fractions, performed in different days.

For example, treatment plans make assumptions about consistent anatomical alignment between the initial images used to design the treatment and the patient's actual anatomical shape and position at the time of each radiation treatment, but this is never completely true (positional and set-up errors, as well as anatomo-pathological variations). These assumptions have driven the development of imaging subsystems for radiotherapy machines with the sole purpose of guiding the treatment on a daily basis, thereby increasing the accuracy and precision in dose placement within the body.

In addition to positional/set-up errors, the geometric variations of target and critical normal organs can also have a negative impact on the outcome of radiotherapy. Volumes of interest may change from one treatment fraction to another due for example to mass shrinking (inter-fractional changes). Random shifts in internal anatomy also occur from day-to-day with magnitudes typically less than 1 cm. For example, the prostate is frequently displaced – up to 1 cm – by changes in rectal content (Langen & Jones, 2001). The anatomy of the patient could also change during a single fraction: sources of motion include respiration, peristalsis, swelling, muscle flexure, cardiac function, and voluntary movements – possibly due to pain or treatment-related tensions (intra-fractional changes).

The scale of this motion ranges from typically a few mm to as much as several cm in the extreme.

In order to compensate for these variations, treatment volumes have been defined for treatment planning in ICRU report 50 and 62. Not only the Gross Tumour Volume (GTV) is irradiated, i.e. position and extent of the primary tumour, but a set of safety margins is added (Fig. 5). First, the Clinical Target Volume (CTV) surrounds the GTV and describes the extent of microscopic, un-imageable tumour spread; then, the CTV together with the second margin constitute the Internal Tumour Volume (ITV), that accounts for uncertainties in size, shape, and position of the CTV within the patient. Last, the Planned Target Volume (PTV) is a geometrical concept introduced for treatment planning and evaluation. It is the recommended tool to shape absorbed-dose distributions to ensure that the prescribed absorbed dose will actually be delivered to all parts of the CTV, despite geometrical uncertainties such as organ motion and setup variations. This margin considers both the internal margin (IM) and the setup uncertainties. The setup margin (SM) accounts specifically for uncertainties in patient positioning and alignment of the therapeutic beams during the treatment planning, and through all treatment sessions.

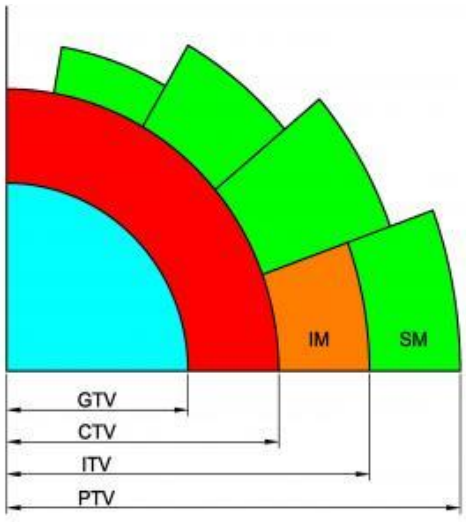

Figure 5. **Different clinical volumes in radiotherapy.** GTV = Gross Tumour Volume. CTV = Clinical Target Volume (GTV + subclinical involvement). ITV = Internal Tumour Volume. PTV = Planning Target Volume. IM = Internal Margin (physiological variations, as breathing, tumour shrinkage, weight loss...). SM = Setup Margins (set-up uncertainties, ineffective immobilisation). Source: http://oftankonyv.reak.bme.hu

With advanced imaging techniques, any possible variations in the beam geometry or patient geometry become measurable during the process of treatment. This process of radiation treatment during which the treatment plan can be modified just before each treatment fraction based on the current anatomy is known as “Adaptive Radiotherapy” or ART (Lim-Reinders et al, 2017, Dickie et al, 2017, Castelli et al, 2018).

Although the concept of integrating imaging technologies directly into the treatment plan is not novel, the last years have seen a rapid expansion in the availability and adoption of IGRT systems directly in the treatment room. Correcting for anatomical shifts each day before treatment follows a process as depicted in Fig. 6.

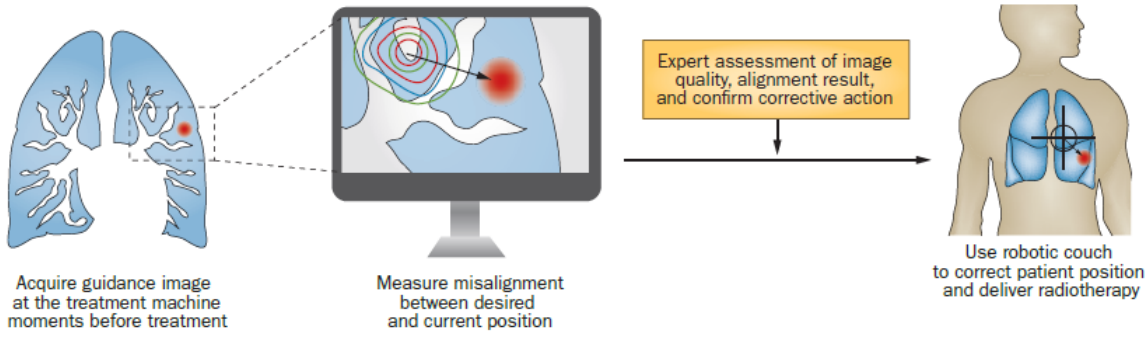

Figure 6. **Targeting radiotherapy before each fraction.** Current IGRT practice focuses on the use of images acquired at the time of treatment to direct the placement of radiation fields within the body. These systems need to be highly integrated given the large number of patients who are treated on a typical radiotherapy unit per day. Observed changes in disease and anatomy detected in these images drive the adaptation paradigm of image-guided radiotherapy. Source: Jaffray et al., 2012.

As confidence in these systems increases, opportunities arise to plan treatments with much ‘tighter’ or ‘more-aggressive’ margins. The ability to reduce these safety margins has interesting collateral effects across the field of radiotherapy. These effects include (i) the reduction in dose to surrounding normal tissues, due to the fact that higher precision in tumour localisation allows to reduce the safety margins and therefore the irradiated volume; (ii) the pursuit of higher total dose to the tumour; (iii) the reduction in the number of fractions used to deliver a therapeutic effect linked to an increase of the effectiveness in each single treatment; (iv) the interest in nonuniform dose patterns according to intra-tumoral heterogeneity which could be put into practice once the appropriate degree of

accuracy and resolution have been achieved; and, finally, (v) the image-based detection and quantification of anatomical or biological changes during treatment in order to correct for deviations with respect to the plan. These different paradigms enable highly personalized interventions that exploit the flexibility of radiations as a therapeutic agent (Jaffray, 2012).

Physicists and engineers continue to advance the technology of radiotherapy. Acting on the imaging information in a precise and effective manner is critical. State-of-the-art radiation treatment machines have adopted robotic technologies and control systems that enable robust manipulation of radiation production, shielding, and positioning of the patient to generate highly conformal dose distributions within the body.

In addition to hardware-related developments, there has also been advancement in development of software tools for designing and adapting radiation treatments. The past twenty years have seen substantial advancements in the modelling of anatomical deformation, to enable the accumulation of radiation dose over the course of treatment despite the observed anatomical changes (Yan et al., 1999, Brock et al., 2005). These advances will also synergise with the conformity advantages intrinsic to particle therapy. Indeed, the integration of other imaging modalities to guide and adapt the treatment will be even more important in particle therapy, in which geometric changes affect the placement of the Bragg peak within the patient through 3D displacements and variations in the amount and type of tissues the particle transits through within the patient (Paganetti, 2012).

1.6 Cone-Beam CT: an imaging technique for Adaptive-Radiotherapy

Accurate patient positioning and beam placement is crucial for achieving desired treatment outcomes. However, patient set-up variations and errors can occur during the course of treatment. In order to ensure proper patient positioning relative to the treatment beam IGRT is used, to correct for any changes in patient position and target localization before each treatment session as mentioned in the previous chapter. Traditionally, radiographic films were placed beyond the patient to produce an image. This method was time consuming in terms of development and evaluation of the films and was limited to a set-up

accuracy of about 5 mm (Barry et al., 2012). Later, Electronic Portal Imaging Devices (EPIDs) mounted on a linear accelerator (LINAC) using robotic arms were introduced into clinical practice. EPIDs produce digital images that allow for online treatment verification and automatic analysis. Additionally, these digital images can be readily deployed and shared via networks improving data flow in the Radiation Oncology departments.

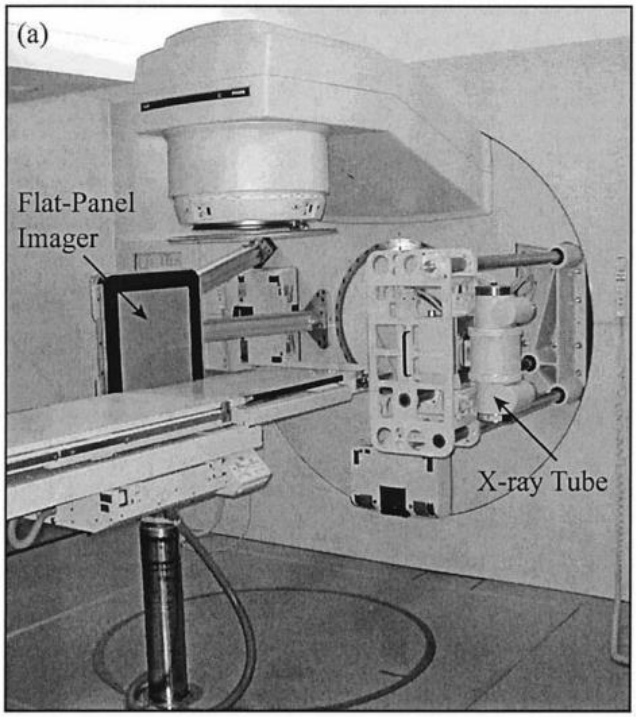

Figure 7. **Medical LINAC modified for CBCT.** A kV X-ray tube has been mounted on a retractable arm at 90° with respect to the treatment source. Source: Jaffray et al., 2002.

However, since EPIDs use LINAC beams in the megavoltage energy range, poor contrast images are obtained due to Compton Scattering, i.e. the scattering of a photon by a charged particle, usually an electron, that prevails when high energies are involved. This resulted in a trend to use diagnostic (kV) X-rays to the target area to provide images with higher contrast. In practice this was achieved by mounting an X-ray tube and Flat Panel Imager (FPI) onto the LINAC gantry such that they share a common isocentre with the treatment unit (Fig. 7). The placement of a kV source/imager on the LINAC gantry opened up the possibility of obtaining tomographic slices through the patient by rotating the LINAC gantry with the kV source/imager. However, as the LINAC treatment couch typically cannot move when the beam is on, a cone-shaped rather than fan-shaped kV beam is employed to enable the acquisition of a volumetric data set in one gantry rotation. The 3D volumetric data is obtained directly from a reconstruction of its 2D projections. This imaging approach is an example of Cone Beam Computed Tomography (CBCT) (Jaffray et al., 2002).

Currently IGRT can be performed using many systems and techniques. Depending on the structure of interest, the clinical objectives and the desired level of precision, a suitable IGRT tool should be chosen. The use of CBCT with kV x-rays (30–140kV) offers superior

low contrast resolution when compared to EPIDs. Additionally, high spatial resolution (Groh et al., 2002) and high quantum efficiency (~60%) have made CBCT a popular choice in radiotherapy applications.

1.7 Outline of the thesis

This thesis work is organised as it follows:

- In Chapter 2, CNAO and the global framework are presented;
- In Chapter 3, a brief review on CBCT shows its basic features, main applications in modern radiotherapy, as well as its limits;
- In Chapter 4, the experimental part is deployed. This includes a validation of the CBCT reconstruction software currently used at CNAO using a virtual phantom, a further analysis through a physical phantom, as well as a comparative analysis of this same physical phantom and also real patients' 3D volumes reconstructed using different algorithms. After, a post-processing shading correction method on 2D projections of patient data is deployed and tested.
- In Chapter 5, results coming from the experimental part are presented and discussed.
- In Chapter 6, conclusions and future perspectives are reviewed.

2. CNAO

2.1 National Centre of Oncological Hadrontherapy

The National Centre of Oncological Hadrontherapy (CNAO) is a non-profit Foundation located in Pavia (Fig. 8, 9, 10). The Italian Health Minister, which in 2001 created the CNAO foundation to build and administer the facility, contributed to most of the project. The founding members are five Hospitals in Milan and Pavia and the TERA foundation led by Amaldi, one of the main promoters of CNAO.

In 2006 about 65 engineers, physicists and technicians, of which at least 40 belonged at CNAO, worked on the project to follow and coordinate over 80 contracts, participants in the construction of the building and electronic components. In this way, it was possible to unite around a single project a set of experts in the field of nuclear physics, that have followed the whole construction and commissioning phase of the devices, and which will guarantee the functioning of the accelerators in the future.

The design of CNAO was aimed at achieving the following objectives:

- The structure should be able to treat deep tumours up to 23 cm of water-equivalent path length (WEPL) with light ion proton beams and mainly carbon ions, ensuring access to clinical and radiobiological research projects;
- For the first phase, three treatment rooms will be set up with four fixed beams, three horizontal and one vertical. At full capacity, there will be five treatment rooms, two of which equipped with a gantry and one research room (Fig. 8).

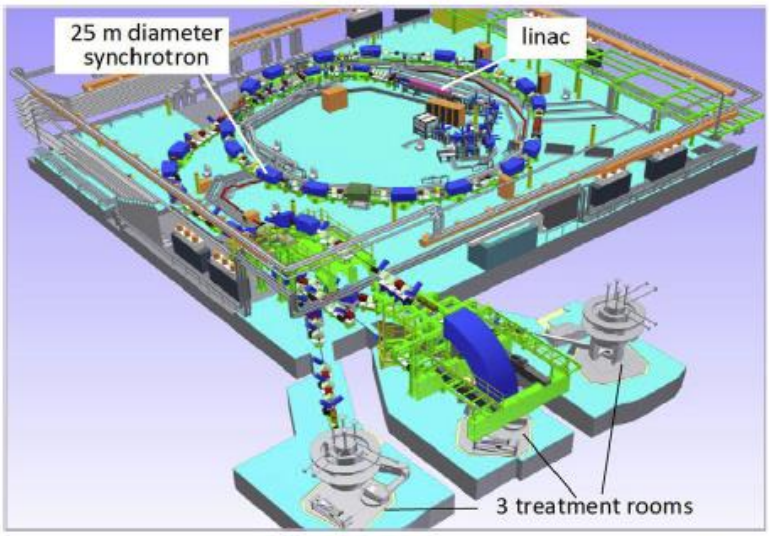

Figure 8. **Organization of CNAO centre**.

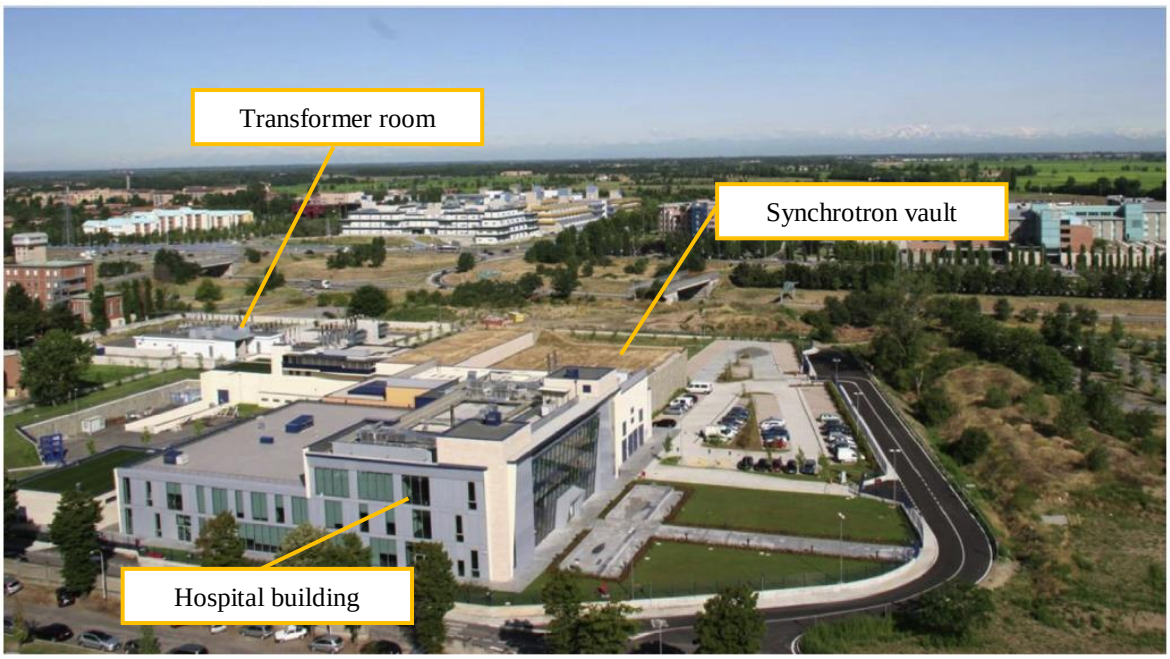

Figure 9. **Top view of the area occupied by CNAO.** In front the hospital building and the entrance, in the back the power station and the roof of synchrotron vault. Adapted by Rossi, 2015.

The technological design has been guided by the requirements of the therapeutic beam defined by radiotherapists, sanitary physicists, and physicians, and widely discussed in detail by the international community. The basic design of the accelerators and the transport line of the beams to treatment rooms was conducted at CERN as part of the

PIMMS project (Badano et al., 1999, Badano et al., 2000). In the years 1999 to 2003, TERA changed the PIMMS project trying to get the most compact design possible, reducing costs and spaces until reaching the PIMMS/TERA project, characterised by:

- Adoption of a single linear accelerator (LINAC) suitable both for accelerating protons or carbon ions, built at GSI and identical with respect to that used in the Heidelberg structure;
- Compact design of the injector, which is placed inside the circle of the synchrotron and within the beam extraction and transport line;
- Beam extraction system similar to that of HIMAC and HIT;
- Attempt to reduce transport lines of the beam as much as possible, to meet the economic criteria;
- Possibility to add other treatment rooms in a further step without interfering with the medical routine.

The total investment so far supported was 90 million euros, of which 80% guaranteed by the Italian Health Minister.

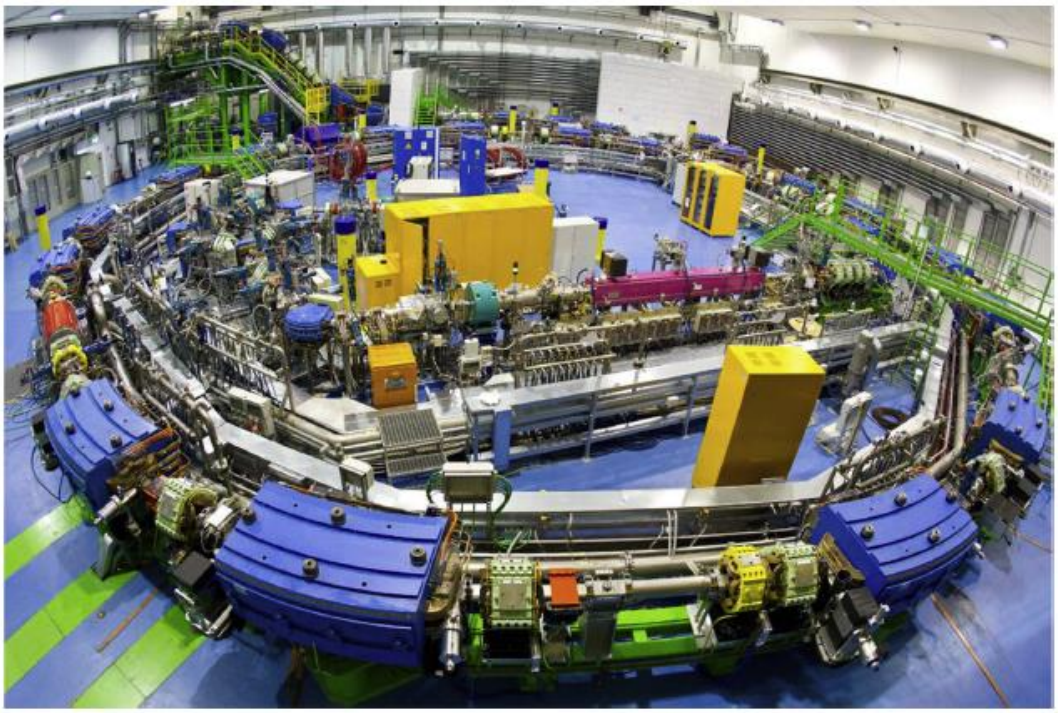

Figure 10. CNAO synchrotron. View of the synchrotron and beam transport lines. Source: Rossi, 2015

CNAO has started in 2014 the normal running phase with patient's treatments authorized by the national health system. At present more than 1600 patients completed the treatment. The pathologies are elective for hadrontherapy and include tumours close to critical organs that cannot receive extra doses, or tumours that are radioresistant and thus not responding to conventional X-ray therapy.

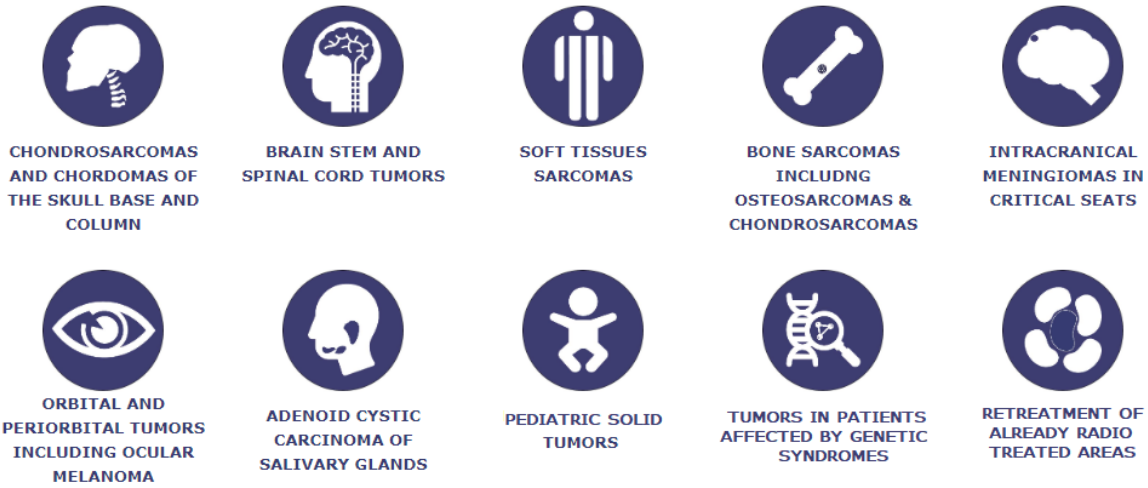

Figure 11. List of pathologies treated at CNAO. Source: www.fondazionecnao.it

The R&D programmes of CNAO are fundamental to keep the centre up-to-date and at the forefront of the fight against cancer.

2.1.1 Clinical workflow at CNAO

Before the treatment, the patient is subjected to a CT scan called "simulation CT" or "planning CT", without diagnostic purposes, but aimed at obtaining images of the site of the lesion to be irradiated. This examination is carried out under the conditions of position and immobilisation that will then be reproduced in each treatment session: in facts, customised devices will be packaged every time to ensure the optimal positioning and immobilisation of each patient, in order to accompany the patient and make the treatment reproducible in every session.

CT represents the current clinical standard in radiotherapy for dose calculation and can be combined with other imaging modalities to improve target definition, such as Magnetic Resonance Imaging (MRI).

On the planning CT (or a combination of image modalities) the clinician identifies and outlines the target volumes and critical organs. Based on the ICRU definition, specific treatment volumes for each type of pathology are identified. Prescription and fractionation doses are specified too, together with the total duration of the treatment, closely correlated to the type of pathology and to the single case. This information constitutes the treatment plan.

The patient, at each fraction, will be repositioned as in the simulation phase, considering also any inter-fractional or intra-fractional change through the safety margins previously deployed. This is realised by means of the Patient Positioning System (PPS) in combination with in-room imaging (Frigerio, 2010).

2.1.2 IN-ROOM IMAGING SETUP AT CNAO

The concept of patient setup is based on positioning and immobilisation. The couch is docked to a 6 degrees of freedom patient positioning device. The PPS drives automatically the patient into the nominal position defined at treatment planning and two independent verification systems are applied for patient setup verification and refinement. A first check is performed by means of an infrared optical tracking system (OTS), that, if needed, computes a correction vector based on markers placed on the patient. Then X-ray projections are acquired by means of a dedicated image-based verification device (Patient Verification System, PVS) and a second correction vector, based on bony anatomy X-ray image registration, is in case calculated.

In Fig. 12, the systems used inside the treatment rooms for positioning patients are shown. The six degrees of freedom robotic pantograph holding the patient couch (PPS), the three infrared cameras of the OTS and the ceiling equipment (PVS) hosting two orthogonal X-ray tubes (faced by two flat panels) are visible. Quality assurance checks are carried out daily to verify the consistency of all patient positioning and verification hardware.

Although the indication of the OTS cannot replace information provided by in-room imaging devices and X-ray image registration, the reported data show that OTS preliminary correction might greatly support image-based refinement and also provide a secondary, independent verification system for patient positioning (Desplanques et al., 2013).

Figure 12. **Patient positioning and verification system inside one of treatment rooms at CNAO.** Source: Rossi, 2015

The central treatment room at CNAO features two fixed beam lines (horizontal and vertical) for proton and carbon ion therapy. This set up required the development of a dedicated imaging system, as commercial solutions turned out to be not compatible. As two beam lines are available in this room, thus potentially allowing more complex treatment geometries, the introduction of 3D volumetric imaging was considered as a key requirement. The imaging system (Fig. 13) was developed in-house by the Bioengineering Unit in collaboration with the Polytechnic of Milan. It consists of a robotic mounted imaging device designed for X-ray projections and cone beam CT (CBCT) acquisitions. A six joints articulated robot Kawasaki ZX-300S) is installed on the room floor and equipped with a custom C-arm tool, integrating a diagnostic kV X-ray tube (Varian A-277) and an amorphous-silicon flat panel detector (Varian PaxScan 4030D). Due to the geometry of the CNAO treatment room, images are acquired few meters out of the treatment isocenter (Iso-

T), thus defining a specific imaging isocentre (Iso-I). This procedure entails patient transport towards Iso-I location and back by means of the PPS.

Figure 13. **Custom robotic in-room imaging (CBCT) installed in the central room of CNAO.** Source: Rossi, 2015

3. CONE BEAM COMPUTED TOMOGRAPHY (CBCT)

Cone Beam CT represents one image modality to perform image-guided radiotherapy and subsequent treatment adaptation with respect to the anatomo-pathological situation of the day. It is currently adopted in different clinical scenarios in radiotherapy and it is of relevant interest among research institutions and commercial companies with still open questions to be solved (Srinivasan et al., 2014).

3.1 OVERVIEW OF CBCT IN RADIOTHERAPY

A schematic illustration of a cone shaped X-ray beam directed towards a flat panel imager through the object (volume of interest) is shown in Fig. 14. Typically, the cone-shaped beam is further collimated to produce rectangular beams.

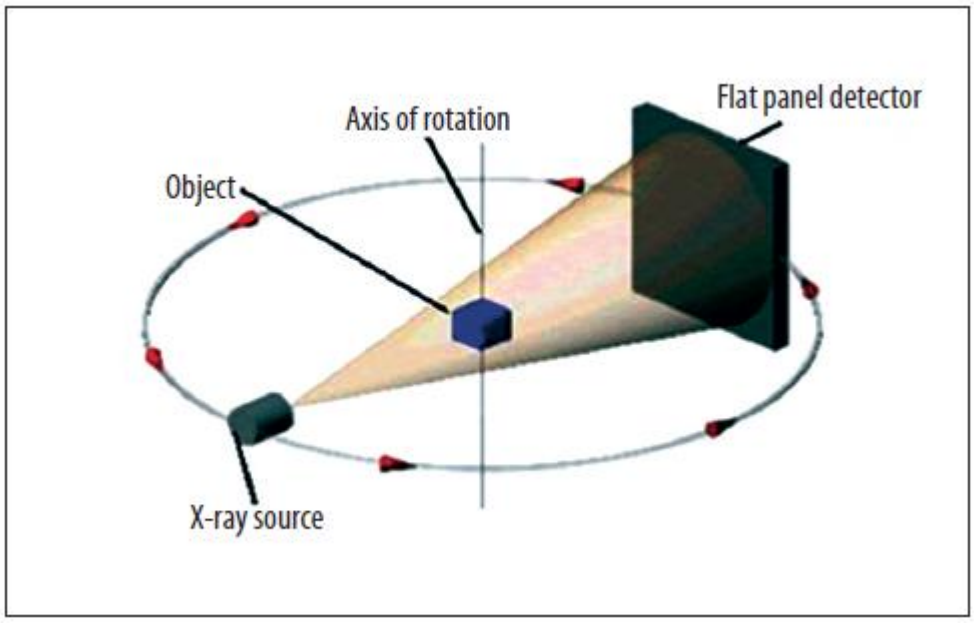

Figure 14. **Schematic illustration of Cone Beam CT geometry.** Source: Srinivasan et al., 2013

CBCT was first commercially available for dentomaxillofacial imaging in 2001 (Mukherji & Miracle, 2009). Since then this technology was found to be promising for radiotherapy applications such as IGRT, as it could reduce patient set-up errors before each treatment session. In-room CBCT acquires images of the patient in the treatment position to verify the patient set-up. Any displacement of the target region (both inter-fractional and intra-fractional movements) during the course of the treatment leads to a lowered dose being delivered to the target. An increase in the target dose is only possible by reducing field margins (ICRU Report 62). Thus, the field margin is the limiting factor in the coverage of the entire tumour and its movements. In order to reduce the field margin, the inter-and intra-fractional tumour motion must be managed.

CBCT as ART tool helps track anatomical changes as well as regression of tumour volume and incorporates them to re-optimize the treatment plan either online or offline during the course of radiotherapy (Nijkamp et al., 2008, Foroudi et al., 2011).

At present, there are three gantry-mounted cone beam devices available. They are the Varian On Board Imager (OBI) (Varian Medical Systems, USA), Elekta XVI (Elekta Oncology Systems, UK) and Siemens (Siemens Medical solutions, Germany) (Fig. 15). The Varian and Elekta systems are kV- CBCT imaging modalities (30–140 kV), in which the kV X-ray source and a kV detector are attached to the LINAC gantry at a 90° offset from the treatment beam. Siemens has developed both kilovoltage cone beam (kVision™) and megavoltage cone beam imaging tools (MVision) (1–6 MV) for patient position verification and adjustments.

Figure 15. Cone Beam systems mounted on medical LINACs. (A) Varian OBI imaging system [courtesy and Copyright ©2007, Varian Medical Systems, Inc.]; (B) Elekta XVI system (courtesy and Copyright© 2008, Elekta AB (publ)); (C) Siemens MVision (courtesy and Copyright© Siemens AG, 2002–2008).

Images produced by kV-CBCT show a superior high-contrast resolution due to the dominance of the photoelectric effect at kV energies. At MV energies, since the dominant interaction is Compton scattering, the image contrast for MV-CBCT images is reduced for several tissue equivalent materials. In order to further understand the advantages, disadvantages and the practical considerations of CBCT in radiotherapy, the hardware and the software components of CBCT are briefly explained below.

3.2 CBCT HARDWARE

3.2.1 X-RAY SOURCE

The x-ray source is either kilovoltage (30–140 kV) or megavoltage (1–6 MV). Travel range of the collimator, the target angle and the focal spot value vary depending on the CBCT design. Once the beam exits the window, it is first modified by a fixed primary collimator followed by two pairs of movable Lead blades which adjust the field size. In addition, Varian uses two custom-designed aluminium filters called “Bow-tie” that equalize X-ray intensity laterally across the detector for two different modes of acquisition. The bow-tie filter is inserted between the source and the patient to reduce intensity variations across the detector.

3.2.2 FLAT PANEL IMAGER (FPI)

The flat-panel imager technology used in CBCT was first investigated by Jaffray and Siewerdsen (Jaffray & Siewerdsen, 2000). This technology is based on fabricating 2D matrix of hydrogenated amorphous silicon (a-Si: H) thin-film transistors (TFTs) on a large area of scintillating material (Thallium doped Caesium Iodide). Such systems demonstrate excellent optical coupling efficiency (the efficiency of converting light photons into electrical signals and in readout signal) and hence improved imaging is possible with high optical absorption, high uniformity over large area and high detective quantum efficiency

(DQE) of ~60% (Srinivasan et al., 2013). These systems produce images with improved soft tissue contrast at acceptable imaging doses.

3.3 CBCT SOFTWARE

Two-dimensional reconstruction methods require the acquisition of multiple axial sections, with a two-dimensional geometry. CBCT, on the other hand, is based on the adoption of a radiation beam with conical geometry that fully invests the region of interest (Fig 16).

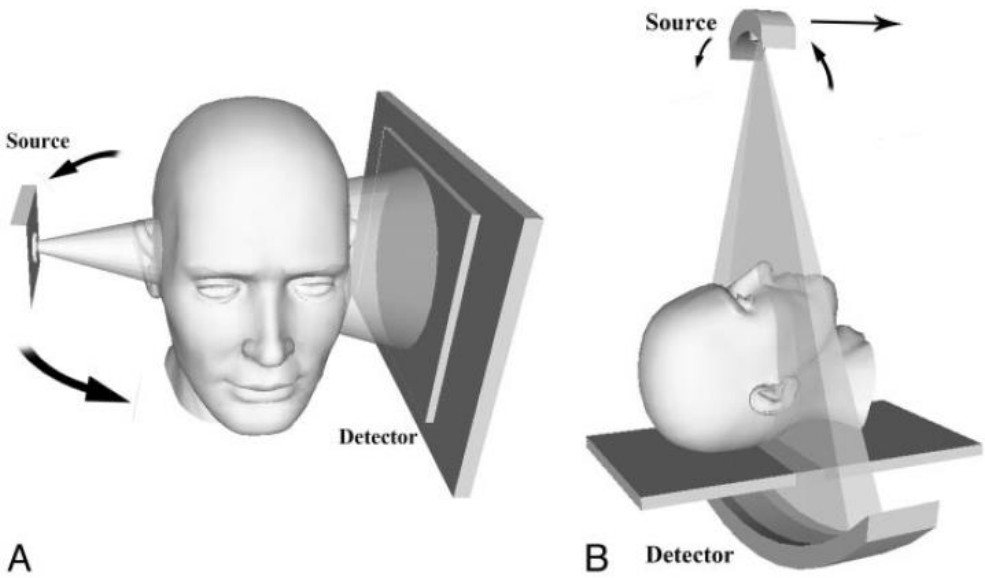

Figure 16. CT geometries. (A) Cone-Beam geometry. (B) Conventional fan-beam CT geometry. Source: Miracle & Mukherji, 2009

In this case, 3D volumetric data can be directly reconstructed from the two-dimensional projection data. This is referred to as cone-beam reconstruction. The Feldkamp, Davis and Kress (FDK) algorithm is the most popular approximate reconstruction technique for cone-beam projections about a fixed isocentre acquired along a circular trajectory (Feldkamp et al., 1984). The FDK algorithm is an extension of the Filtered Back-Projection reconstruction. In this method, the measured cone-beam projections are pre-weighted, filtered and finally back projected along the same ray geometry as initially used for forward projection (Feldkamp et al., 1984). Details of the method will be discussed in Chapter 4.

In current commercial CBCT reconstruction systems, though many algorithms exist, the FDK algorithm is still the most frequently used (Qiu et al., 2012). More recently, iterative reconstruction algorithms have also been investigated for clinical application, such as Simultaneous Algebraic Reconstruction Technique (SART) (Qiu et al., 2012) and alternated direction optimisation methods (ADMM) (Ren et al., 2015). Whenever projection data is limited, for example, iterative algorithms have been shown to have a better performance in CBCT reconstruction than algorithms based on FDK (Qiu et al., 2012). Due to the iterative nature of these algorithms, however, they require intense computations that have prevented their use in clinical practice.

Cone-beam CT image quality is afflicted by artefacts, as explained in Sec. 3.5.1. These artefacts reduce contrast and cause generally incorrect CT numbers. Standard CBCT scans can therefore not be used for dose-recalculation and re-planning of the patient treatment, which is required in ART. Instead, many institutions have adopted diagnostic in-room scanners or acquire regular CT scans throughout the treatment course.

Many methods have been proposed to cope with the shortcomings of CBCT including anti-scatter grids and software-based solutions (Bertram et al., 2008, Rührnschopf et al., 2011a/b, Zhao et al., 2016, Stankovic et al., 2017). Convolution-based methods, in which the scatter is modelled as a convolution of the projections, can be found in routine clinical use (Zhu et al., 2006, Rinkel et al., 2007, Meyer et al., 2009, Sun & Star-Lack, 2010). Several papers have investigated intensity correction based on the planning CT, for example, through Monte-Carlo simulation of the CBCT acquisition process (Mainegra-Hing et al., 2010, Thing et al., 2016, Zollner et al., 2017) or using planning CT as a prior (Niu et al., 2010, Niu et al., 2012, Park et al., 2015). A more recent approach tried to perform projections intensity correction in the projection space by the use of convolutional neural networks (Hansen et al., 2018).

CBCT approach has been proved to be more effective from the point of view of the dose administered to the patient, of the acquisition times and also of the use of the beam. In fact, in addition to respecting the natural conical development of the beam avoiding the use of collimators, a volume is acquired in a time comparable to that of a conventional CT, with a dose release lower than the multi-slice CT of 35% in case of acquisition of a cranial volume and of 49% in case of acquisition of the whole body (Kim et al., 2008).

3.4 CBCT Applications in Radiotherapy

The primary use of CBCT on LINACs is for IGRT. However, it can also be employed for ART as HU values could be obtained through calibration for the use in treatment planning. These applications are discussed below.

3.4.1 CBCT for IGRT

With highly conformal treatment techniques, an advanced imaging modality is required for a precise localization of the target and OARs. CBCT enables radiation therapists to correct for changes of the target position prior to treatment and allows monitoring of complex changes of the patient and tumour anatomy, typically caused by patient's loss of weight and tumour regression (shape/volume changes). Developments in large area flat-panel detectors and computing capacity have made CBCT an ideal, and the most common, platform for high precision 3D IGRT tasks (Jaffray, 2002) and has begun replacing two-dimensional IGRT in order to verify whether the tumour region is encompassed within the planning target volume (PTV) throughout the treatment. Thus, CBCT as IGRT became a popular modality for the verification of patient set-up and tumour position (Moore et al., 2006).

The use of CBCT-based IGRT has improved radiotherapy treatment at various treatment sites, such as prostate, lung and head and neck (Oldham et al., 2005, Guokenberger, Boda-Heggeman et al., 2011). CBCT-based IGRT in prostate phantom studies has shown high accuracy with residual errors <1 mm. However, in clinical situations, the inter-observer variability was >2 mm for cases without implanted markers. The strategy of daily re-planning reduces these uncertainties. The advantage of volumetric IGRT over 2D techniques results from the fact that it helps evaluate OAR geometry. For example, bladder filling enables reduction of the dose delivered to OARs and allows significant reduction in PTV margin from 8 mm to 4 mm (Pawlowski et al., 2010).

3.4.2 CBCT FOR ART

The precision of dose delivery over a treatment course using a single reference can be limited due to changes in the patient's anatomy (weight loss) and the size/extent of the tumour (tumour shrinkage and displacement). Hence, information about the patient and tumour anatomy immediately preceding each treatment fraction is of extreme importance for improving therapy outcome. CBCT has the potential to become a useful tool for online ART (Ding et al., 2007) as it helps to localize the position of the tumour in 3D and register any changes in the anatomy of the tumour or the patient during the treatment. This is done by fusing CBCT images with planning CT images using image registration algorithms (rigid or deformable registration) and evaluating the differences. The dose distribution is recalculated, if necessary, using the treatment planning system or with software provided with the imaging system. Thus, optimal treatment plans can be obtained using CBCT scans adaptively.

Several studies have used CBCT datasets for adaptive plans to reduce the planning and target margins during the course of treatment (Peroni et al., 2012, Landry et al., 2015, Veiga et al., 2015, Seco & Spadea, 2015, Kurz et al., 2016, Hua et al., 2017, Yao et al., 2018). Volumetric image guidance for photon therapy became widely adopted as dose distributions from IMRT turned highly conformal and the radiation delivery less forgiving to patient setup errors; also, it provides more information on tumour and patient anatomical changes, thus facilitating better decision making for adaptive re-planning (Hua et al., 2017). For proton therapy, the advantages of CBCT guidance are well recognised (Mori et al., 2013, Engelsman et al., 2013, Seco & Spadea, 2015), and as said, even more critical than in photon therapy because of the Bragg peak, and despite clinical adoption of volumetric image guidance for proton therapy has been slow compared to its adoption for photon therapy, more recently this technology has been implemented more widely in new facilities. Thus, the rationale for using CBCT as ART is to account for the daily changes in tumour anatomy during dose delivery in order to reduce the volume of normal tissue being irradiated and reduce dose delivered to OARs.

In spite of the increasing use of CBCT for patient set-up verification, the relatively poor image quality of CBCT and particularly significant variability in HU poses problems for its use as an effective tool for ART. Richter et al., 2008, reported that the CBCT geometry

(large volume of X-ray exposure) and associated scatter radiation can cause variations in HU values of CBCT. This fluctuation in HU values affects the accuracy of dose calculation, since the HU values are related to electron density used in dose calculation algorithms. One of the biggest challenges in calculating the dose on CBCT datasets in practice is the issue of limited FOV from CBCT or problems with deformable registration if calculating on adapted planning CT (Richter et al., 2008).

Although studies that investigated CBCT for treatment planning displayed good agreement with PCT of within 1–3% for phantoms and within 2% for prostate patients using deformable image registration, the level of accuracy breaks down with changes in patient/phantom size (Srinivasan et al., 2013, Hatton et al., 2009). Thus, the results cannot be assumed to be the same for all volumes of scanned object and hence there is no uniformly accepted solution so far. This indicates the need for reliable HU calibration curves appropriate for a particular treatment site for planning in order to use CBCT potentially for ART (Srinivasan et al., 2013). This can be achieved by using calibration phantoms that closely match the size of the treatment site to be scanned (e.g. prostate, H and N).

3.5 Concerns in CBCT

The increased use of CBCT in imaging has led researchers to explore patient imaging dose. Cone beam geometry covers a large field of view in one rotation, which contributes to a larger scattered radiation component when compared to fan beam CT. The total amount of detected scattered radiation in CBCT exceeds the primary radiation leading to low HU values in the middle of the reconstructed images. This leads to artefacts which impact image quality, such as homogeneity, contrast and noise in the reconstructed CBCT image. Care should be taken when acquiring CBCT images to keep image artefacts to a minimum by selecting optimal scanning parameters and carefully positioning and stabilizing the patient. Daily images from CBCT deliver significant dose to the patient. Therefore, an accurate knowledge of CBCT dosimetry is essential as the use of this modality increases. Three major concerns in CBCT are discussed: artefacts, image quality and patient dose.

3.5.1 ARTEFACTS: CAUSES AND SOLUTIONS

Some of the most commonly visualised artefacts in CBCT – scatter and noise, beam hardening and motion artefacts – are discussed below.

SCATTER AND NOISE. The CBCT images include a larger amount of scatter when compared to fan beam CT. This has been identified as one of the major limiting factors for the current image quality in flat panel-based CBCT (Siewedersen & Jaffray, 2001, Sharpe, 2006). The larger contribution of scatter in CBCT is due to a larger FOV of cone beam geometry (Yang et al., 2007). This causes the photons to deviate from their original path and increase the incident intensity, leading to artefacts. Scatter is the most severe cause of inhomogeneity artefacts, such as cupping artefact, degradation of contrast and enhancement of noise in CBCT images. Several scatter correction algorithms have been proposed in the literature to control these artefacts (Ning et al., 2004, Siewerdsen et al., 2006, Siewerdsen et al., 2004, Zhu2009]. They can be grouped into three categories: scatter reduction techniques, measurement-based scatter correction and software-based scatter correction. Anti-scatter grids and bow-tie filters are the cone beam scatter reduction methods that have been adopted so far. The techniques used for the measurement-based scatter compensation intend to correct for the scatter effects either before viewing the projections or by post-processing the acquired projections. Finally, the software-based scatter correction adopted convolution-based filtering with the assumption that the distribution of scatter signal in an image is equivalent to a blurred version of primary signal distribution. In spite of these methods being developed, there is currently no uniformly accepted solution.

Noise is an unwanted signal in an image distributed either randomly or non-randomly. Generally, there are two major types of noise in X-ray projections: Gaussian (electrical noise) and Poisson noise (quantum noise). The Poisson noise (fluctuation of photons exiting the object) in CBCT is high because CBCT machines are operated at low tube current values for the purpose of dose reduction. Thus, the signal-to-noise ratio (SNR) is much lower in CBCT than in fan beam CT. When images with such low SNR are reconstructed, inconsistent linear attenuation coefficient values and hence HU numbers are produced. Therefore, low contrast resolution is reduced due to a high noise level (Steinke & Bezak, 2008) leading to loss of diagnostic information.

BEAM HARDENING. An X-ray beam hardens as the low energy components of the polychromatic spectrum suffer from substantial attenuation in the centre of the object, as seen in the image of the homogeneous phantom in Fig. 18A. This would result in a central-to-peripheral grey value gradient in the final image, showing a “cupping” or “capping” artefact, due to the effect and overcorrection, respectively, of beam hardening. Cupping and capping artefacts are compared in Fig. 17.

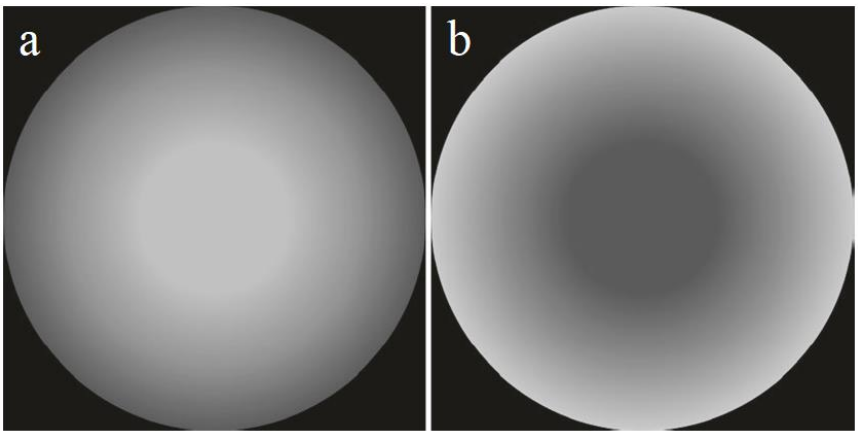

Figure 17. Cupping and capping artefacts. Adapted from Pauwels, 2018

The second type of artefact related to beam hardening is in the form of dark streaks and bands between and around high-density objects in an image, when high atomic number and high-density materials are in the FOV. Larger FOV of cone beam geometry results in recording of high intensity nearly inhomogeneous materials in reconstructed images leading to streak artefact (Density phantom, Fig. 18B). This streak artefact is very similar to that caused by scatter radiation. Built-in scanner features minimize beam hardening. These features include the use of bow-tie filters, calibration of CBCT scanners for different tube voltages and utilization of correction algorithms (Zhu et al., 2009, Wei et al., 2011). The obtained correction factor reduces bands between bone structures and reduces cupping artefacts in the reconstructed images. Fig. 18C shows the corresponding reconstructed slice of a CIRS density phantom acquired from fan-beam 16-slice CT scanner (Philips Medical Systems, Cleveland, Ohio, USA) under similar scanning conditions for comparison purposes.

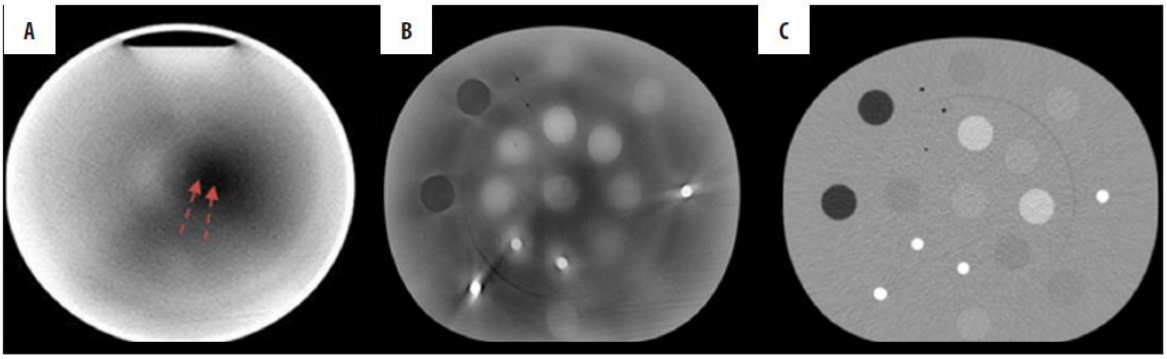

Figure 18. Different CBCT artefacts. (A) A dark smudge (arrows) at the centre of the homogeneous phantom scanned by CBCT, (B) dark streaks around high density inserts seen in CBCT scanned density phantom and (C) planning CT image without streaks. Source: Srinivasan et al., 2014

MOTION AND MISALIGNMENT ARTEFACTS. Apart from the above-mentioned routine CBCT artefacts, motion and/or misalignment artefacts are also a problem in CBCT (Schulze et al., 2011). The limited LINAC gantry rotational speed makes CBCT images more prone to motion artefacts due to an extended acquisition time. In patient scans, the motion of the structures during scanning leads to streaks from high-contrast objects, such as bones and air cavities (Yoo et al., 2007). The blurring (Sonke et al., 2005) or streaking (Baker, 2006) effects due to moving structures are shown in Fig. 19A and 19B, respectively. The large physical displacements cause double contours (Fig. 19C) on the images ("ghost" images). Patient motion artefacts can be reduced by using positioning aids and appropriate protocols to prevent blurring caused by respiratory motion. A misalignment in the source-to-detector position relative to the stationary object causes inconsistencies during the back projection process leading to blurring of the images. This kind of misalignment errors can be minimized by appropriate quality assurance of the mechanical stability of the systems.

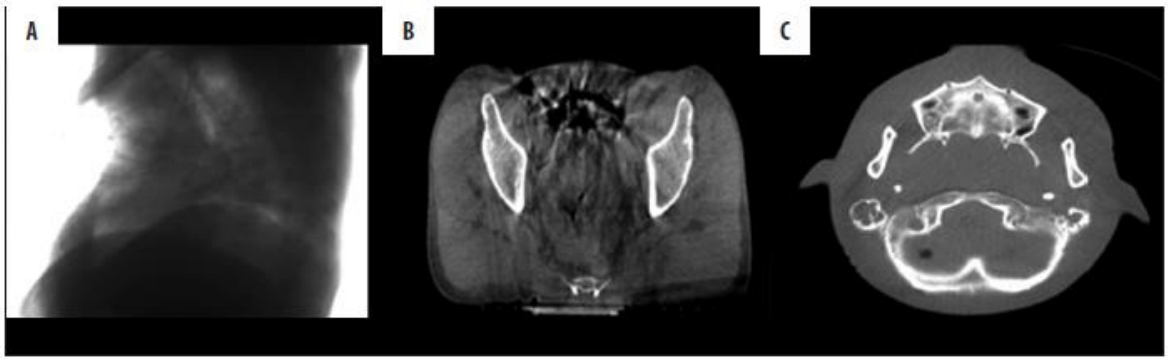

Figure 19. **Movement artefacts in CBCT.** (A) Blurring induced by breathing motion, (B) streaks induced by the movement of bowel gas and (C) double contours induced by patient movement during CBCT acquisition process. Source: Srinivasan et al., 2014

ALIASING ARTEFACTS. In cone beam geometry, the number of rays reaching per voxel decreases linearly with an increase in the distance of the voxel from the source. As a result, voxels that are closest to the source collect more rays than those located near the detector. This under-sampling of data by the divergence of the cone beam (Schulze et al., 2011) leads to misregistration of information. This results in line patterns in CBCT datasets, called aliasing artefacts, where lines seem to diverge from the centre towards the periphery (Figure 23A). Aliasing may also be introduced by crude interpolation during back-projection in approximating the length of the ray that traverses the voxel. This artefact is greatly reduced by using more sophisticated projection and back-projection techniques (Mueller et al., 1999). It can be further reduced by carrying out a larger number of projections per rotation and using a better interpolation method conforming more closely to the physical measurement conditions. However, the need of massive computational power prevents these methods from being used in commercial scanners.

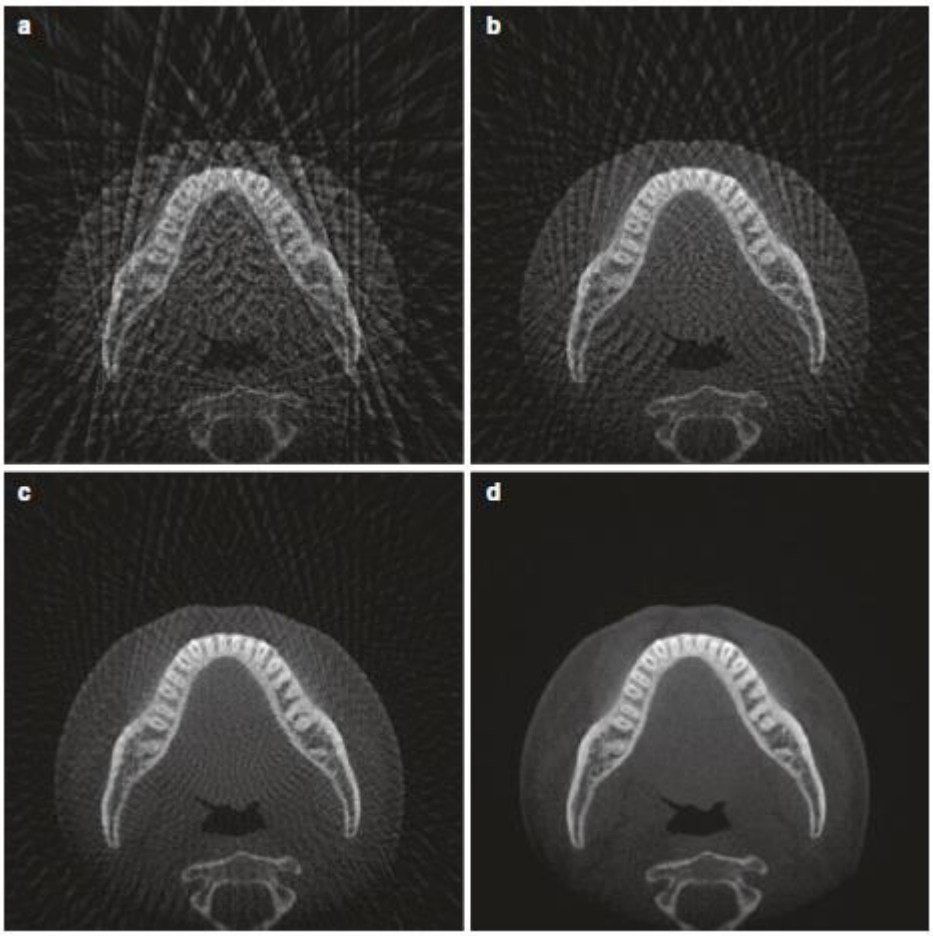

Figure 20. Aliasing artefact due to image subsampling. Source: Pauwels, 2018

In general, many technical developments are in progress in order to reduce these cone beam artefacts. As most of the errors occur during reconstruction, an effective approach to avoid these artefacts is by using sophisticated algorithms that account for large FOV volumes. The use of Iterative reconstruction techniques that can handle more complex models and accommodate assumptions regarding the statistical fluctuation of the acquired projections could greatly reduce the artefacts and provide cone beam reconstructions with improved noise characteristics. However, iterative methods take hours to complete as compared to a few minutes for FDK. Thus, the clinical use of iterative reconstructions can be feasible only by increasing the computational speed to the order of a minute.

In conclusion, there are several methods to reduce these artefacts as much as possible, although they also depend on the hardware and the method of reconstruction itself. For

these reasons, the compensation of these artefacts is still an open issue, both from the point of view of image quality but above all to be able to perform ART using the CBCT itself.

3.5.2 IMAGE QUALITY

CBCTs are used to assess patient positioning at the time of treatment through image registration. Therefore, image quality parameters of these devices, such as high-contrast resolution, low-contrast resolution, contrast-to-noise ratio, image uniformity and noise, are of great importance. Current CBCT systems have limitations due to image resolution and sensitivity of the detector. Projection geometry (Scarfe & Farman, 2007) is also an issue because of the lower number of cone beam projections from circular orbits and from approximations used in the reconstruction algorithm. The smaller number of projections from a circular orbit in the cone beam geometry is insufficient for an accurate reconstruction of the volume. Furthermore, due to computational limitations, all currently available CBCT machines make use of an FDK reconstruction algorithm, which simply approximates the line integral without computing the original distance that the ray traverses between the source and the detector.

Although the kV CBCT technique is clinically well-established, intensified scatter artefacts lower image quality and hence the diagnostic information. Image quality studies (Kamath et al., 2011, Elstrøm et al., 2011] for the different CBCT acquisition modes have been performed to find parameters that diminish image quality. A comprehensive study of the relation between the dose and image quality in low-dose CBCT (Yan et al., 2012) showed that 72.8 mAs is a safe dose level for visualizing low-contrast objects, while 12.2 total mAs is sufficient for detecting high-contrast objects of diameter >3 mm. Therefore, CBCT image quality acts as a potential limiting factor in terms of patient dose.

Recently, more and more proton therapy system vendors equip their gantries with CBCT imaging systems intended for patient positioning (Rit et al., 2016, Veiga et al, 2016). The acquired CBCT images provide information on the position of bony anatomy, the gross volume changes, and the position of the patient on the treatment couch. But among other aspects, due to high scatter contribution (Siewerdsen & Jaffray, 2001), image quality is typically insufficient for accurate dose calculation in IMPT, even if rescaling the image

intensities (Kurz et al., 2015). Nevertheless, several groups have recently shown that CBCTs can be used for reliable proton dose calculation by utilizing deformable image registration (DIR) of the planning CT (pCT) to the daily CBCT, yielding a so-called virtual CT (vCT) (Peroni et al., 2015, Landry et al., 2015, Veiga et al., 2015). Alternatively, it has also been suggested to use the DIR-based vCT as a prior for scatter correction of CBCT projections (Niu et al., 2010, Niu et al., 2012). Promising results for protons have been obtained with this method, using phantom data and a single prostate patient (Park et al., 2015); the method has furtherly been validated on four prostate cancer patients by Kurz et al., 2016, that found this procedure an interesting approach to enable and extend the applicability of CBCT-based adaptive IMPT to sites where the accuracy of DIR might be limited, e.g. due to pronounced anatomical changes. In Chapter 4, the method is tested on the CNAO dataset.

3.6 AIM OF THE WORK

The purpose of this work is to analyse and test the analytic CBCT reconstruction technique adopted clinically at the National Centre for Oncological Hadrontherapy in Pavia and compare this with iterative approaches presented in the literature, aiming at evaluating the quality of the reconstructed images. For the same reason, a method of 2-dimensional projections correction present in literature was also tested. This acts on the already acquired projections before image reconstruction, thus potentially providing improved CBCT quality. The thesis is comprehensive of quantitative evaluation performed both on physical/digital phantoms as well as on patients' data. The final goal consists in providing a comparative analysis to support the clinical practice.

4. EXPERIMENTAL PART

The experimental part of this thesis consisted of two sub-sections:

I. A comparative analysis of the algorithm presently employed in the clinical practice at CNAO with respect to other reconstruction algorithms, both for a physical phantom and patient data; a validation of the clinically-used algorithm is also performed on a digital phantom
II. Preliminary testing of a 2D shading correction algorithm on CNAO patient dataset.

Dataset characteristics

The imaging system involved consists of a robotic mounted imaging device designed for cone-beam CT acquisitions. Six joints articulated robot (Kawasaki ZX-300S) is installed on the room floor and equipped with a custom C-arm tool, integrating a diagnostic kV X-ray tube (Varian A-277) and an amorphous-silicon flat panel detector (Varian PaxScan 4030D). About 600 projective images are acquired, during a 220° gantry rotation around the patient. The C-arm is moved at 5.4°/sec while the FPD (Fuzzy-Proportional-Derivative) controller captures images at 15 Hz frame rate, thus sampling the covered CBCT fan with a 0.36° step. Under these settings the complete gantry rotation for a single CBCT acquisition takes 40.7 s. In order to limit the computational workload, the images are acquired at halved FPD resolution (1024 × 768 pixels, 387.7 × 388.0 μm pitch). The geometry calibration is obtained by processing image-by-image the stack of projections acquired over the CBCT rotation, thus generating a geometry look-up table at FPD frame rate resolution. There is no hardware synchronisation line between the beginning of gantry motion and the start of FPD frame grabber, that is instead software triggered. As a consequence, images are not expected to be captured at reproducible angles in subsequent acquisitions, due to communication delays and variable panel start-up time. Thus, using the calibration information, images are labelled at runtime during acquisitions by linearly interpolating the geometry look-up table to obtain the geometry parameters at any gantry angle. Labelled images are provided to the reconstruction module. The INSIGHT TOOLKIT (ITK) software (www.itk.org) and the RECONSTRUCTION TOOLKIT software

(www.openrtk.org) have been used in most of the experimental part, along with MATLAB software (www.mathworks.com). The reconstruction method currently implemented at CNAO consists of the Feldkamp–Davis–Kress algorithm (Feldkamp et al., 1984) implemented in RTK and adapted to work with CNAO data. The reconstructed CBCT field-of-view is an isocentric box featuring a dimension of 220 × 220 × 220 mm with voxel size 1 × 1 × 1 mm.

The dataset used in this work consists of a physical phantom and patients' data. The physical phantom is the CatPhan® 600 (The Phantom Laboratory, Salem, NY). Patients' data consists of thirteen patients, all treated in extra-cranial districts, in particular twelve in the pelvic region and one in the abdominal region.

A CT acquisition associated to each CBCT patient data is also available. CT images are acquired with a conventional commercial CT scanner (Siemens SOMATOM Sensation Open CT scanner) with a resolution of 0.98 × 0.98 × 2 mm.

All the computations have been performed on a Windows 10 workstation, 64-bit, CPU Intel Xeon W-2123, 3.60 GHz. The reconstructions are GPU-based, and the GPU is nVidia Quadro P5000. CUDA version is 10.0.

4.1 3D APPROACH: COMPARATIVE ANALYSIS OF DIFFERENT RECONSTRUCTION ALGORITHMS

Alternative reconstruction methods have been evaluated and compared with the clinically adopted FDK method, to investigate possible improvements in CBCT image quality with regard to the data available at CNAO. These reconstructions were performed using functions implemented ad hoc in RTK, following a preliminary step of choosing the best parameters for each method. The tested methods are all iterative and have been chosen since in some cases it is necessary to reduce the number of projections in order to lower the imaging dose. Thus, the small amount of projections data makes the reconstruction problem challenging, and the proposed solutions to handle limited-angle situations typically involve iterative reconstruction methods (Mory, 2014). The FDK method

currently implemented at CNAO and the alternative methods tested are explained in the following sections.

In general, given noise-free data, an exact reconstruction algorithm produces a result where the difference to the real object can be made arbitrarily small by increasing both the detector resolution and the number of projections (Turbell, 2001). As for fan-beam reconstruction, there also exist exact algorithms for cone-beam data. In some cases, however, exact algorithms have some important shortcomings and approximate algorithms are preferred. An example of this is the case of truncated data: exact algorithms assume that the entire object is located within the FOV. This is clearly not feasible in medical tomography. The simplicity of FDK method has made it the most used algorithm for cone-beam reconstruction, and another important advantage is that is handles truncated data in longitudinal direction (Turbell, 2001).

4.1.1 FELDKAMP DAVIS KRESS (FDK) ALGORITHM

In the original form, FDK assumed the cone-beam data to come from a planar detector (Fig. 21, 22). It is not exact in the sense that the reconstruction result will deviate somewhat from the measured object regardless of the measurement resolution: in facts, it approximates the conic beam with a series of fan-beams, but for moderate cone-angles, these differences are small and often acceptable, as flat panels for medical use are not so extended.

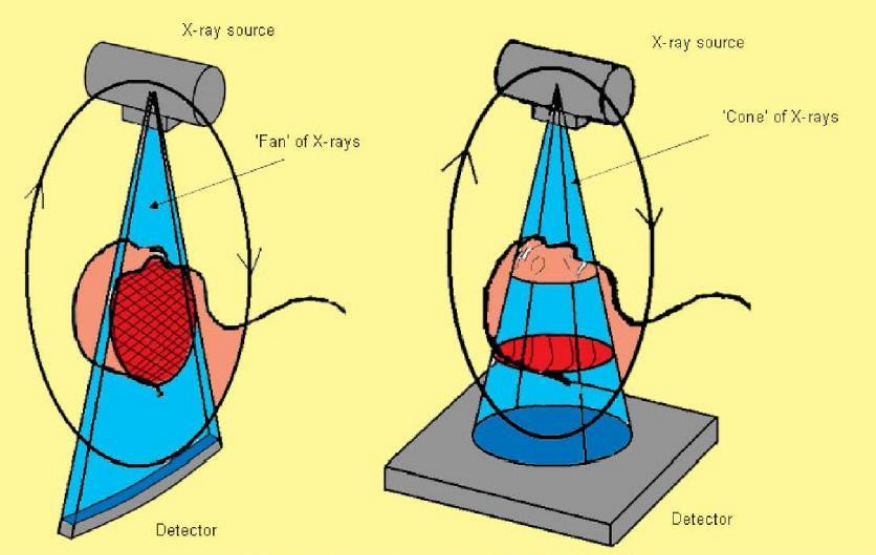

Figure 21. Fan-beam and Cone-beam compared.

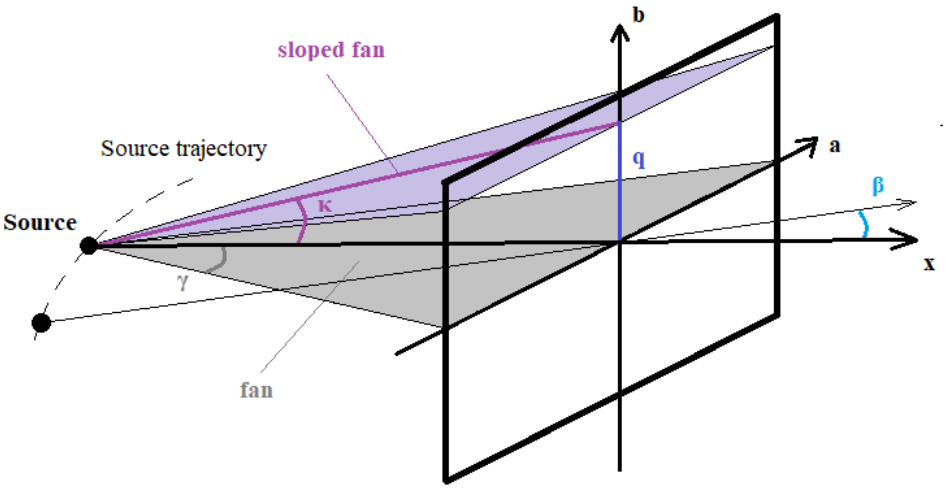

Figure 22. FDK reconstruction geometry. The FDK algorithm approximates the conic beam as a series of fan beams in the longitudinal direction. Adapted by Turbell, 2001

We define the projection angle as β, and the fan-angle as γ. R is defined as the source-detector distance. The projection data is called $p(\beta, a, b)$ where a and b are coordinates depicted in Fig. 22, and given by

$$a = R \cdot \tan\gamma \quad \text{and} \quad b = \frac{q}{\cos\gamma}$$

The cone-angle, κ, is defined as

$$\kappa = \arctan\frac{q}{R} = \arctan\frac{b}{\sqrt{R^2 + a^2}}$$

The reconstruction is a filtered back-projection very similar to the two-dimensional algorithm, and the projection data are handled row by row. In addition to the convolution with the ramp filter, $g^P(\gamma)$ (in our case with Hann windowing) a pre-weighting factor is applied, yielding

$$\tilde{p}(\beta, a, b) = \left(\frac{R}{\sqrt{R^2 + a^2 + b^2}} \cdot p(\beta, a, b)\right) \cdot g^P(\gamma)$$

The pre-weighting factor is a geometrical correction for rays crossing obliquely the object: since the distance to cover is longer, they undergo a higher attenuation. This is considered by multiplying their contribution by the cosine of both the fan-angle γ and the elevation angle κ, in facts

$$\frac{R}{\sqrt{R^2 + a^2 + b^2}} = \frac{R}{\sqrt{R^2 + a^2}} \cdot \frac{\sqrt{R^2 + a^2}}{\sqrt{R^2 + a^2 + b^2}} = \cos\gamma \cdot \cos\kappa$$

The pre-weighted and filtered projections are then back-projected into the reconstruction volume as

$$f_{FDK}(x, y, z) = \int_0^{2\pi} \frac{R^2}{U(x, y, \beta)^2} \cdot \tilde{p}(\beta, a, b) \cdot d\beta$$

where

$$a(x, y, \beta) = R \cdot \frac{-x\sin\beta + y\cos\beta}{R + x\cos\beta + y\sin\beta}$$

$$b(x, y, z, \beta) = z \cdot \frac{R}{R + x\cos\beta + y\sin\beta}$$

In the discrete case, the integral is naturally replaced by a sum over the projections angle. Note that in medical applications the projections angle may cover a range of values that is less than a complete rotation.

The factor $U(x, y, \beta)$ only depends on the distance between the source and the reconstructed voxel projected onto the central ray as

$$U(x, y, \beta) = R + x\cos\beta + y\sin\beta$$

then

$$\frac{R^2}{U(x, y, \beta)^2} = \frac{R^2}{(R + x\cos\beta + y\sin\beta)^2} = b^2 \cdot \frac{1}{z^2}$$

Therefore, this term corrects for the decrease of intensity with the squared distance between the focal spot and the reconstructed voxel projected onto the central ray and so it is independent of the *z*-coordinate of the voxel.

The implemented version performs also other corrections, as a weighting of image projections to handle off-centred panels in tomography reconstruction. They are not fully descripted here since they are not the object of this analysis, and also because the same pipeline has been applied for all the reconstruction methods, substituting each time only the reconstruction algorithm.

4.1.2 SIMULTANEOUS ALGEBRAIC RECONSTRUCTION TECHNIQUE (SART)

The implementation of the algorithm is based on the method descripted by Andersen and Kak in (Andersen & Kak, 1984). This method and all the other tested algorithms are iterative. To better understand how SART works, imagine dealing with a dataset made of one original image f made of two voxels, called f_1 and f_2, and only two projections, called p_1 and p_2, so that

$$p_1 = w_{11} \cdot f_1 + w_{12} \cdot f_2$$

$$p_2 = w_{21} \cdot f_1 + w_{22} \cdot f_2$$

that is, in compact form

$$\vec{p}_i = \vec{w}_i \cdot \vec{f}$$

where w_{ij} weights the contribution of each component of f in each projection and exploits how the ray crosses the volume. Projections are measured and f has to be estimated, but if the number of projections and the number of unknowns is not the same, as it happens in clinical applications, the equation system has not a unique solution and an iterative algorithm is needed. Therefore, the Algebraic Reconstruction Technique starts from an arbitrary initial guess and then, iteration after iteration, updates the estimate in the following way:

$$\vec{f}^{n+1} = \vec{f}^{n} + \vec{w}_i \cdot \frac{\vec{p}_i - \vec{w}_i \cdot \vec{f}^{n}}{\vec{w}_i^{T} \cdot \vec{w}_i}$$

At each iteration (n):

1) Projections of the actual reconstructed volume $\vec{f}^{n}$ are simulated ($\vec{w}_i \cdot \vec{f}^{n}$)
2) The difference between the real projection data available ($\vec{p}_i$) and the actual simulated projection is computed to extract the error that guides the correction
3) The error is normalised to have an error that is independent from whatever unit of measure of $\vec{w}_i$
4) The correction is weighted and applied to the old estimate to obtain a new one.

In particular, in Simultaneous–ART implementation the individual i correction terms are computed in the same fashion, but these terms are then saved until all rays in that view have been considered, and the average correction to each picture element is computed and added to form the updated image only in the end. This optimises the computational load and speeds up the convergence. A schematic representation of the method is reported in Fig. 23.

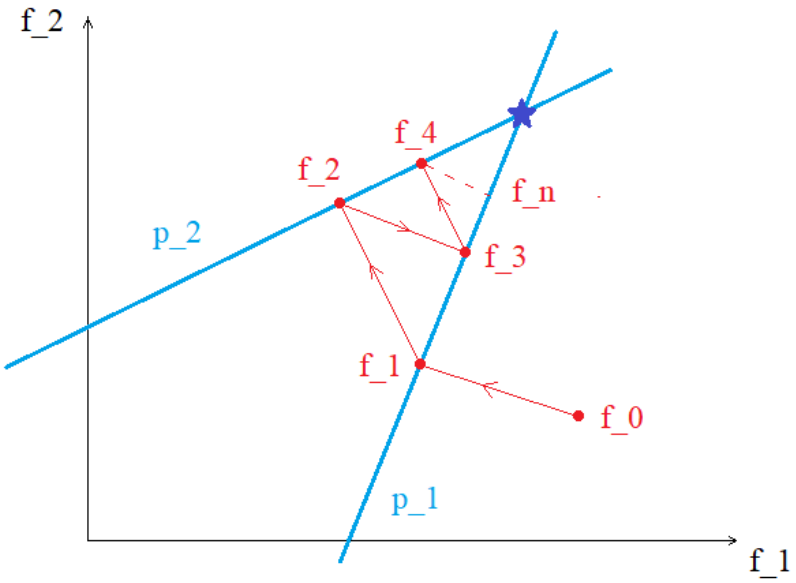

Figure 23. **SART schematic representation.** The two projections in the easy example mentioned at the beginning are shown in blue. They are a linear combination of original image values; therefore, they are represented by lines (more in general, hyperplanes) in the image values space. Their intersection represents the problem's solution, i.e. the value **f** of the reconstructed image that satisfies all the **p** components. The algorithm starts from an initial, arbitrary guess f^0, and scans all the data relying on the distance between the actual guess and the following projection (red lines).

4.1.3 Ordered Subset SART (OS–SART)

OS–SART is a variation of SART method that groups projection data into an ordered sequence of subsets. The main idea of ordered subset methods is to partition the dataset into several subsets. It is crucial to find an effective way for the partitioning. In each iteration, we hope that the image is improved as much as possible with a lower computational cost. Hence, each subset should contain as much complementary tomographic information as possible (Pan et al., 2006, Qiu et al., 2012); in facts, in Fig. 23 it has been showed that SART reconstruction relies on the orthogonality between data to converge from the initial guess to the solution, and poor orthogonality leads to slow convergence, as it is schematically represented in Fig. 24. One of the natural subset partitions is formulated by dividing the projection data according to the projection angles, in order to optimise the convergence. Furthermore, subsets must have a relatively small size for computational balance.

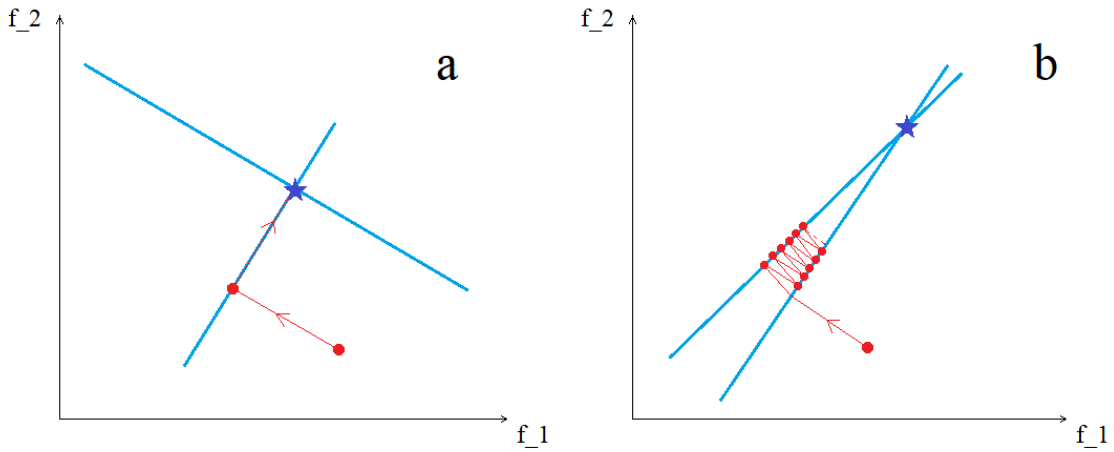

Figure 24. **Orthogonality of projection data.** Full orthogonality between projections (a) leads to a fast convergence, with only one step. Poor orthogonality (b) causes very slow convergence.

An iteration of OS–SART is defined as a single pass through all the subsets, in each subset using the current estimate to initialise the application of SART with that data subset.

4.1.4 Alternating Direction Method of Multipliers (ADMM)

The last two algorithms tested in this work lay in the field of compressive sensing. The promise of compressive sensing is the exploitation of compressibility to achieve high quality image reconstruction with less data (Graff & Sidky, 2015). It is a signal processing technique for efficiently acquiring and reconstructing a signal, by finding solutions to undetermined linear systems. This is based on the principle that, through optimisation, the sparsity of a signal can be exploited to recover it from far fewer samples than required by the Shannon-Nyquist sampling theorem. The signal is therefore required to be sparse in some domain.

A signal is said to be N–sparse in a certain basis if it has at most N non-zero coefficient in this basis. Numerical methods have been developed to recover a signal from far fewer – adequately performed – measurements than what is dictated by the Nyquist criterion, under the sparsity assumption. Real signals are never exactly sparse in bases we use, but they may be in a certain well-chosen basis (Mory, 2014).

Constraining the solution to be sparse in a certain basis enforces a certain form of regularity, and rules out irregular solutions. Thus, it is often referred to as regularisation.

Depending on the chosen "sparsifying" transform we have:

- Sparsity of the gradient: Total Variation minimisation (ADMM–TV)
- Sparsity on a wavelet basis: Wavelet transform (ADMM–W)

The general idea is that ADMM minimises a cost function $J(f)$ defined as

$$J(f) = \left|\left|G(Rf - p)\right|\right|_2^2 + RT$$

where the first one is the fidelity term, which considers that the reconstruction must be coherent with the projections, and the second one is the regularisation term that prevents overfitting, that in this case may depend on TV or wavelet decomposition coefficients. In facts, in RTK implementation ADMM is combined with the Augmented Lagrangian Method (ALM) because it allows to use wavelets regularisation too. Here the TV approach is analysed, but ADMM–W works exactly the same except for the computation of the regularisation term.

The method is divided in three main steps (Afonso et al., 2011, Patel et al., 2012, Ramani & Fessler, 2012):

1) Problem reformulation

$$\arg\min_f J(f) = \left|\left|G(Rf - p)\right|\right|_2^2 + \alpha \cdot TV(f)$$

is a non-constrained optimisation problem equivalent to the constrained problem

$$\begin{cases} (\hat{f}, \hat{g}) = \arg\min_{f,\,g} \left|\left|G(Rf - p)\right|\right|_2^2 + \alpha \sum_{v=1}^{V} \left|\left|g(v)\right|\right|_2 \\ subject\ to\ g = \nabla f \end{cases}$$

2) AL (Augmented Lagrangian) iterative minimisation

$$\min_{f,g} \ \left|\left|G(Rf - p)\right|\right|_2^2 + \alpha \sum_{v=1}^{V} \left|\left|g(v)\right|\right|_2 + \beta \cdot \left|\left|\nabla f - g - d_k\right|\right|_2^2$$

non constrained, where $\beta \cdot \left|\left|\nabla f - g - d_k\right|\right|_2^2$ is a term added to control the difference between ∇f and g, and d_k is initially set to zero.

3) Update of d_k at each iteration

Minimisation with respect to f and g is performed by finding first the best f with g fixed, and then finding the best g with f fixed. This "splitting" of the problem gives rise to the method's name. In total, each iteration consists of

$$\begin{cases} f_{k+1} = \arg\min_f \ \left|\left|G(Rf - p)\right|\right|_2^2 + \beta \cdot \left|\left|\nabla f - g - d_k\right|\right|_2^2 \\ g_{k+1} = \arg\min_g \ \alpha \cdot \sum_{v=1}^{V} \left|\left|g(v)\right|\right|_2 + \beta \cdot \left|\left|\nabla f_{k+1} - g - d_k\right|\right|_2^2 \\ d_{k+1} = d_k - \nabla f_{k+1} + g_{k+1} \end{cases}$$

As said before, RT depends either on TV or wavelet decomposition. For TV, we assume that images with excessive details present high TV, and according to this principle, keeping low TV of the image removes details and increases sparsity preventing overfitting. Total variation is computed as (Mory, 2014)

$$TV(f) = \sum_{v=1}^{V} \sqrt{[\nabla_x f(v)]^2 + \left[\nabla_y f(v)\right]^2 + [\nabla_z f(v)]^2}$$

A wavelet is a wave-like oscillation with an amplitude that begins at zero, increases, and then decreases back to zero; the Daubechies wavelet is a particular family of wavelets that takes the name from its inventor (Fig. 25). In mathematics, a wavelet series is a representation of a function by a certain orthonormal basis generated by a "mother" wavelet, useful for multiresolution analysis, that works in a similar way with respect to Fourier transform except that the signal is decomposed in a sum of properly weighted wavelets instead of sinusoids. When wavelet transform is involved, the idea is that an image is sparse if few coefficients of the Daubechies wavelet transform are non-zero (Guerquin-Kern et al., 2009).

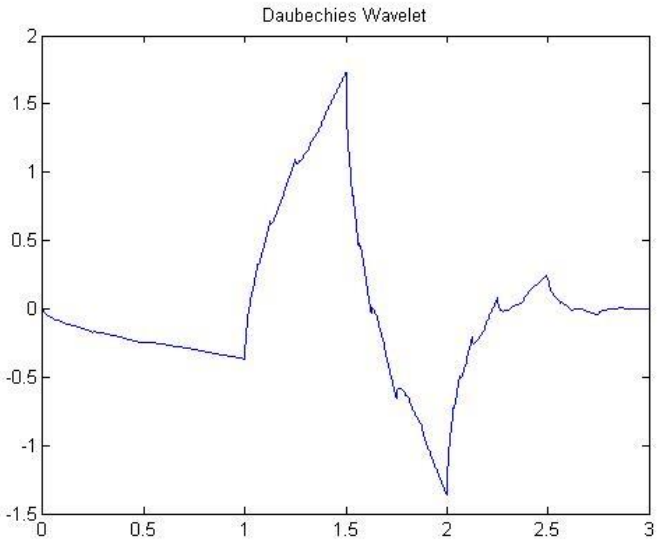

Figure 25. Daubechies mother wavelet.

4.2 PHANTOM STUDY

4.2.1 DIGITAL PHANTOM: GEOMETRICAL VALIDATION OF CNAO RECONSTRUCTION METHOD

Fig. 26 shows the general workflow of this first validation phase. The geometry of the reconstruction method currently employed at CNAO has been tested by means of a virtual Shepp-Logan phantom, carrying out the following steps:

1) Create a virtual Shepp-Logan phantom.
2) Create virtual projections of the phantom.
3) Reconstruct the obtained virtual projections.
4) Compare the original volume with the reconstructed one.

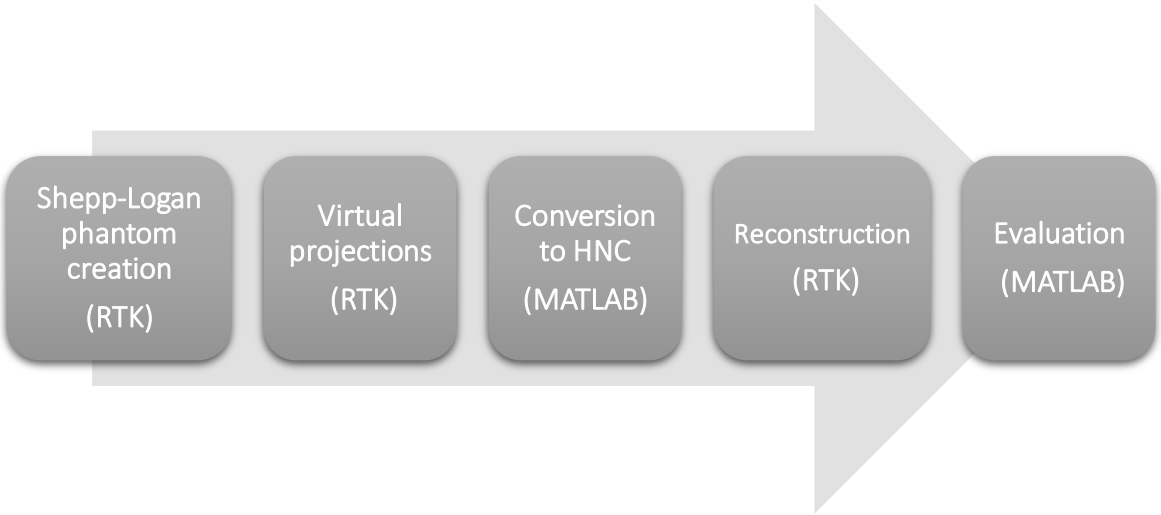

Figure 26. Validation phase workflow.

Implementation details

The phantom was generated using functions already implemented in RTK, in order to obtain a starting volume with the same spacing and offset characteristics of the volumes reconstructed at CNAO, which was our ground truth. Subsequently the projections of the same phantom were simulated in RTK too, performing a forward projection. The geometry of these projections – Source to Isocenter Distance (SID), Source to Detector Distance (SDD), Source to Axis Distance (SAD, the radiation source to gantry rotation axis distance), in plane and out of plane angles for all projections, and gantry angle, offset coordinates for each projection – was passed to the forward projection algorithm by means of a geometry file, taken from a real sample patient data, in order to be as accurate as possible in reproducing real geometrical conditions. The outcome of this step was a stack of projections included in a single 3D volume. Then, the original volume was retrieved starting from these virtual projections using CNAO reconstruction software. The complete, detailed description of the FDK reconstruction method is reported in Sec. 4.1. After that, the original and reconstructed volumes were overlapped to visually assess the agreement between the two from a geometrical point of view.

4.2.2 PHYSICAL PHANTOM: RECONSTRUCTIONS QUALITY EVALUATION

To evaluate the quality of the investigated reconstruction algorithms, a physical phantom acquired with the in-room imaging system at CNAO was used. The analysis was carried out using the Catphan©600 phantom. The purpose of this analysis was to preliminarily investigate the performance of the algorithms, and to choose the best parameters to be used for each on them.

A series of quality measures based on the actual literature regarding Catphan©600 CBCT reconstruction were chosen. These measures are five: signal-to-noise ratio (SNR), contrast-to-noise ratio (CNR), integral nonuniformity, Uniformity Index (UI), and a Spatial Resolution Index (SRI).

A. The Signal-to-noise ratio was derived to compare the level of a desired signal to the level of the background noise. It was evaluated using the CTP486 uniformity module of Catphan©600 (Garayoa & Castro, 2013). Five regions of standard 1 cm^2 were considered, one in the centre and four in the cardinal points of the image, as could be seen in Fig. 27. For each region, mean value m and standard deviation σ are computed, and then SNR is calculated as

$$SNR = \frac{|m_i|}{\sigma_i}$$

(i: centre, north, south, east, west). SNR for each method is the mean over all the five regions.

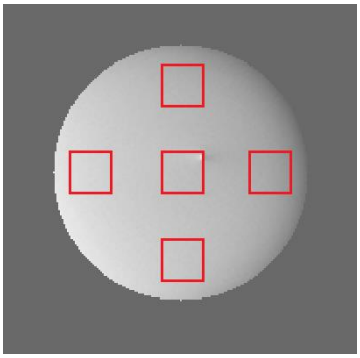

Figure 27. **Uniformity CTP486 module.** The image is reconstructed with the FDK method. Regions used in metrics computation are visible in red.

B. Contrast-to-noise ratio was computed using module CTP404 (Fig. 28a) to measure the ability to distinguish between two areas of interest. Classically, CNR is evaluated using the low-contrast test module CTP515 (Fig. 28b), but it was not clearly visible in our reconstructions, so since the aim was only to compare different reconstruction methods an arbitrary insert in CTP404 was chosen. CNR is computed as (Garayoa & Castro, 2013)

$$CNR = \frac{|m_i - m_b|}{\sqrt{\sigma_i^2 + \sigma_b^2}}$$

where i corresponds to the insert, b to the background measured in a region next to the insert, m denotes the mean value of corresponding ROI and σ its standard deviation.

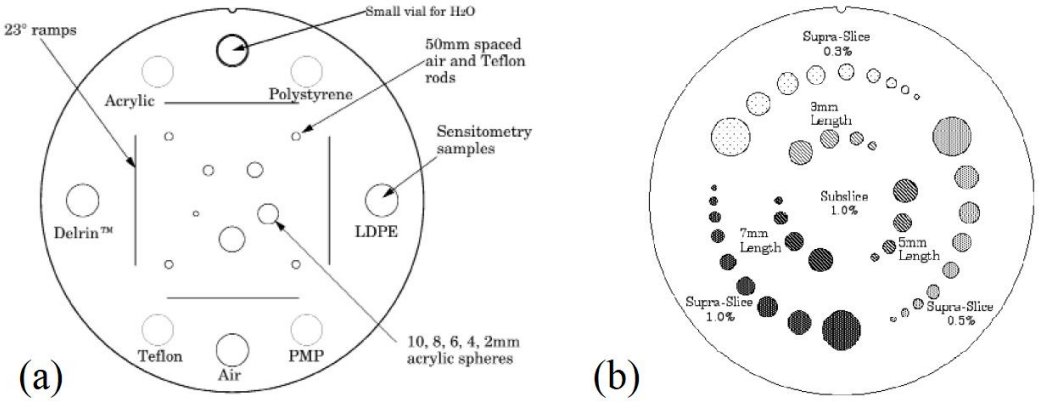

Figure 28. **(a) Module CTP404 and (b) module CTP515.** Adapted by Catphan©600 manual.

C. Uniformity was assessed in module CTP486 too. There is no universally accepted value for field uniformity (Bissonnette et al., 2008), that in this case was assessed using the same five regions involved in SNR computation. Their mean pixel values were used to calculate the integral nonuniformity using

$$Integral\ nonuniformity = \frac{CBCT_{max} - CBCT_{min}}{CBCT_{max} + CBCT_{min}}$$

where $CBCT_{\max}$ and $CBCT_{\min}$ are the maximum and the minimum values, respectively, of the pixels over the five areas.

D. The amount of capping or cupping artefacts was evaluated, for each method, using a Uniformity Index (Bissonnette et al., 2008) (UI, %) defined by the maximum percent difference between each of the peripheral areas and the central area; a positive UI indicates cupping, while a negative UI indicates capping

$$UI = \frac{100 \cdot \left(CT_{periphery} - CT_{centre}\right)}{CT_{centre}}$$

E. The last metric assesses the spatial resolution of the method. It has been applied to analyse the high resolution CTP528 module (Fig. 29). Since no universally accepted index exists, and since both the Catphan©600 manual and the actual literature only perform qualitative analysis on this module, considering only the capability to discern a line pattern or not and taking highest visible frequency as a value for spatial resolution, we tried to create a quantitative metric to score also the accuracy in sensing the line patterns dimensions.

The reconstructed CTP528 slice has been manually segmented for each method. A circular profile on the binary slice is computed. The profile is concentric to the circle on which the patterns are located, and the result is an array of zeros and ones that respectively represents the presence of background or the presence of a line insert. Resolution of this array has been taken equal to the resolution of the reconstructed image (1 mm) as first approximation, even if the circle cuts the pixels obliquely, so that for example a series of three 1 means an insert with a measured

width of 3 mm. The array was visually inspected for each method, and a Spatial Resolution Index (SRI, %) was measured as

$$SRI_i = \left(1 - \frac{|V_{mis} - V_r|}{V_r}\right) \cdot 100$$

$$SRI = \sum_{i=1}^{N} SRI_i$$

where $i = 1, \dots, N$ indicates the number of patterns that we were able to segment.

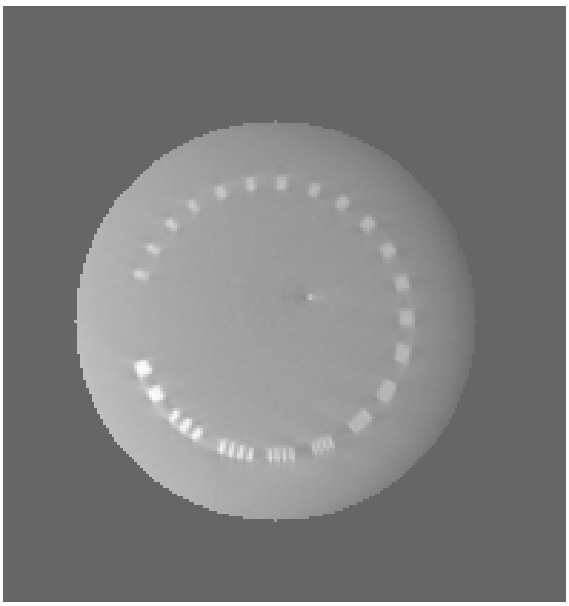

Figure 29. CTP528 module. FDK reconstruction.

For each reconstruction method, different combinations of parameters were tested: changing one parameter at a time, and keeping fixed all the others, default values were tested both for increase and decrease. These metrics were evaluated each time, and the value corresponding to the reconstruction with the best performance was chosen for each parameter. Details on the different parameters in the algorithms and the values set could be found in Appendix 2.

4.3 Patient Study

To compare the behaviour of the different reconstruction algorithms, some similarity measures for CBCT volumes with respect to a reference volume, in this case the planning CT, were chosen. These measurements have been shown to be good for this type of comparison (Skerl et al., 2006), even if their quality depends on the anatomical site considered, the imaging modalities involved, and it is itself a research topic. The chosen similarity measures are easy to implement and are currently used in clinics for full-reference image quality assessment, i.e. that technique that assesses the quality of an image comparing it with a reference golden standard.

Previously, patients' CBCTs were aligned on the corresponding planning CTs relying on MATLAB, following an automatic rigid registration which was finally adjusted by a manual alignment. Volumes of interest were also extracted from the CT data, to compare performance of the algorithms in the regions surrounding particular organs or near the area to be irradiated. The starting volumes (CT, CBCT) were cropped identically before the comparison in order to remove as much as possible the artefacts at the edges on the CBCT volume. For the organs of interest, the structures segmented by the clinicians on the planning CT – that, practically, are represented by binary masks built on the CT volume – were analysed, therefore the registration of the CBCTs on the CTs meant that also these volumes were already registered with the CBCT reconstructions.

We considered Mutual Information (MI), Normalised Mutual Information (NMI), Pearson Correlation Coefficient (PCC) as quality metrics after masking the two images.

Mutual Information in information theory measures how much a variable brings information about one another. It is computed as (Cover, 1991)

$$MI(X;Y) = \int_Y \int_X p(x,y) \cdot \log \frac{p(x,y)}{p(x) \cdot p(y)} \cdot dx\, dy$$

where X and Y are the two images compared, $p(x,y)$ is the joint probability density function and $p(x)$, $p(y)$ are the marginal probability density functions of the two images. The normalised version (NMI) is computed as (Han, 1978)

$$NMI(X;Y) = \frac{mutual\ information}{joint\ entropy} = \frac{MI(X;Y)}{H(X,Y)}$$

Last, the Pearson Correlation Coefficient is a measure of dependence between two variables, that is computed as

$$\rho_{PEARS}(X,Y) = \frac{cov(X,Y)}{\sigma_X \cdot \sigma_Y}$$

where $cov(X,Y)$ is the covariance between the images and σ_X, σ_Y are the standard deviations of the two images.

For all the patients also PCC with respect to planning CT at the level of the Planned Target Volume (PCC_PTV) was computed. For the twelve pelvic patients we evaluated also PCC in the Sigma region (PCC_S), in the Rectum region (PCC_R) and in the Bladder region (PCC_B), as it was specified by the clinicians that these organs are particularly important when treating the pelvic region (Fig. 30).

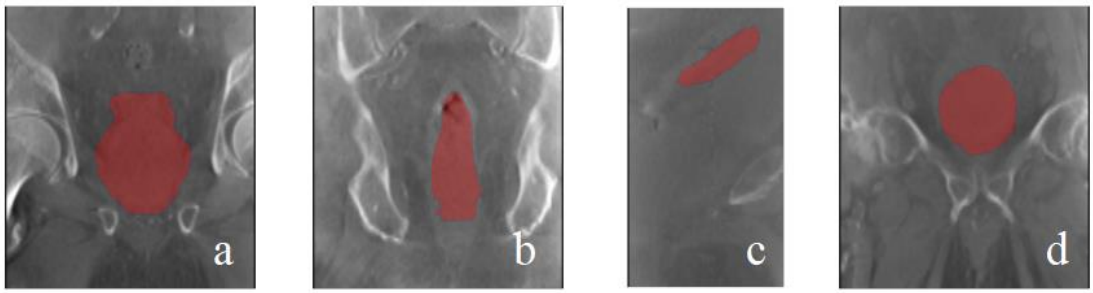

Figure 30. **Internal structures of interest.** In red it is reported an example of (a) PTV, (b) Rectum, (c) Sigma and (d) Bladder, overlaid on the corresponding CBCT.

After computation, for each metric, the values referring to all patients were grouped in vectors divided by reconstruction method (for example, MI_FDK, MI_SART…), each of them previously tested to be normal or not using Lilliefors normality test (unknown mean and variance). Those marked as normal were analysed using the T-test to check for significant differences between vectors representing the same metric evaluated for different methods. For the same reason, Friedman test was performed on non-normal metrics. A significance level of 0.05 has been considered in all these considerations.

4.4 2D Approach: Projections Shading Correction

A CBCT shading correction algorithm using pre-operative CT as a prior was performed using a previously validated and published method (Niu et al., 2010, Kurz et al., 2016, Stankovic et al., 2017, Hansen et al., 2018). Low spatial frequency deviations in the measured projections, such as the detection of scatter and beam hardening (Zollner et al., 2017), are estimated on the basis of a prior virtual CT (vCT) derived by registration of the planning CT (pCT) to the daily $CBCT_{orig}$. In this thesis, the implementation of such an approach represents a preliminary study, since some steps need a calibration step that has not been performed yet. The main steps are:

1. DIR of the pCT to the daily $CBCT_{orig}$, yielding the so-called vCT as a prior;
2. For pelvic patients, an additional step is required to correct the high-contrast geometry mismatching that comes from gas pockets inside the patient (Niu et al., 2012), since DIR is not able to compensate them and still has to be optimised for pelvic region. The gas pocket correction workflow is:
   2.1. Identify gas pockets in the pCT and CBCT images. From the registered pCT and CBCT images, generate binary masks by setting voxel values to 1 or 0 if below or above a certain threshold. Thresholds are empirically chosen resting on the values of the voxels that correspond to air in the images.
   2.2. Fill and create pockets in the pCT based on CBCT geometry. After comparing the two masks generated in step (1), the volume where pCT has gas pockets but CBCT does not is filled with the linear attenuation coefficient of soft tissues – empirically chosen, too – and then, identify the volume where pCT has no gas pockets but CBCT does, and set these voxels to zero.
3. Forward projections of the vCT (P_{vCT}) are calculated according to the CBCT geometry. For this, the vCT CT numbers (in HU) are previously converted to attenuation coefficients μ as in Park et al., 2015: $\mu = (HU + 1024)/2^{16}$. P_{vCT} are converted to intensity as follows:
$$I_{vCT} = 2^{16} \cdot e^{-P_{vCT}}$$
and are assumed to be free of scatter and other deviations.
4. The low spatial frequency deviations I_{SCA} in the measured projections are estimated in intensity domain as the difference of the vCT forward projections (I_{vCT}) and the

scaled measured projections ($I_{CBCT_{orig}}$) plus a generous smoothing (f, according to Niu et al., 2010) accounting for the low spatial frequency of these deviations, that in our case is composed by a median filtering (using a 50 pixels squared window) plus a gaussian filtering (standard deviation = 0.6):

$$I_{SCA} = f(CF \cdot I_{CBCT_{orig}} - I_{vCT})$$

5. The estimated low-frequency deviations are subtracted from the scaled measured projections in intensity domain, resulting in a set of corrected projections

$$I_{CBCT_{corr}} = CF \cdot I_{CBCT_{orig}} - I_{SCA}$$

A further transformation was also performed in the original literature approach, which we decided not to implement since proper calibration with respect to the CT would have been required. This does not affect our analysis since at the moment a one-by-one correspondence between the CT and CBCT voxel values (i.e. calibrate CBCT on Hounsfield Unit values) has not been taken into consideration.

6. Corrected projections are then reconstructed with the FDK algorithm implemented at CNAO.

CF is a scaling factor depending on the mAs of the CBCT protocol, i.e. (Park et al., 2015):

$$CF = \frac{mAs_{ref}}{mAs}$$

CF is required to rescale $I_{CBCT_{orig}}$ to an intensity level that matches I_{vCT} so that the corrected projections will provide accurate HU values after reconstruction. The projection intensity ($I_{CBCT_{orig}}$) is linearly correlated with the exposure current-time product (mAs) applied during the CBCT scan. Therefore, we can assume that a reference mAs (mAs_{ref}) exists that allows for the best HU accuracy of the corrected and reconstructed $CBCT_{corr}$ without any intensity rescaling (corresponding to CF = 1). This reference value was empirically determined in Park et al., 2015, and then further validated (Kurz et al., 2016) referring to Elekta CBCT imaging system, but this kind of calibration has not been performed on Varian hardware yet. Therefore, the value provided by literature is used in this preliminary analysis too, yielding to a CF = 1.3 (CBCT settings 29 mA for pelvis, 30 mA for thorax, with an estimated time s = 66.7 ms obtained dividing total acquisition time by the number of projections).

After correction, global values of MI, NMI and PCC with respect to the planning CT were recalculated on the corrected CBCTs with the same modalities.

5. RESULTS AND DISCUSSION

5.1 PHANTOM STUDY

5.1.1 DIGITAL PHANTOM

The comparison between the original phantom and the reconstructed version could be seen in Fig. 31. The overlap is also displayed. Since a practical calibration for converting HU in CBCT values or vice versa has not been performed yet, it was not possible to compute a geometrical profile on the two images for quantitative analysis, but it is clearly visible the geometry matching between the original phantom and the volume reconstructed in RTK starting from the virtual projections.

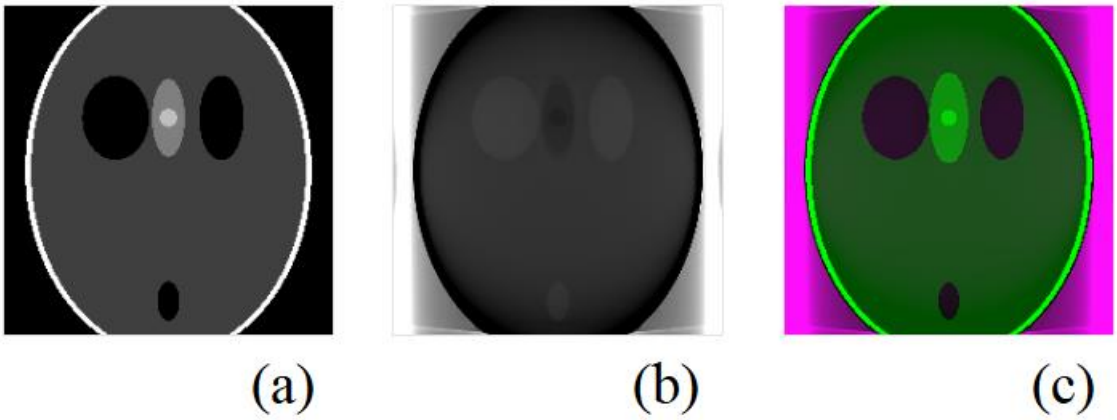

Figure 31. **Digital phantom.** (a) Original phantom, (b) FDK reconstruction and (c) overlay of the two.

5.1.2 PHYSICAL PHANTOM

Results for SNR and CNR are reported in Tab. 1.

Method	SNR	CNR
FDK	39.29	2.00
SART	5.43	0.72
OS–SART	23.23	1.34
ADMM–TV	33.98	1.05
ADMM–W	34.92	0.36

Table 1. Signal-noise ratio and contrast-noise ratio for each reconstruction method.

FDK showed the best performance in terms of signal and contrast-to-noise ratio, having the highest values for such indices. All the other methods present similar values, except for SART that is affected by a very low signal-to-noise ratio. This high level of noise could be appreciated in Fig. 32b, where a representation of the uniformity module for each of the tested methods is showed.

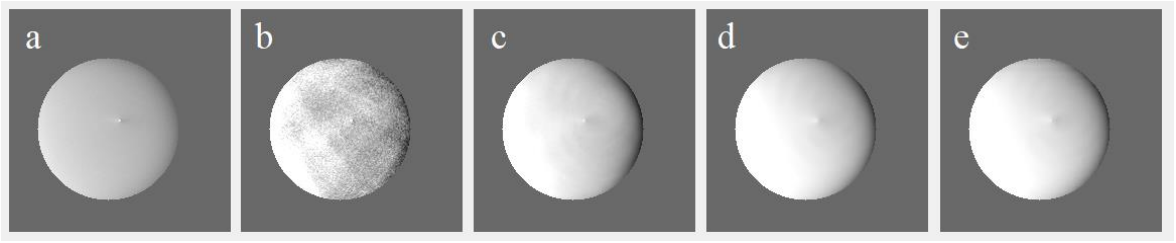

Figure 32. Uniformity module reconstructed with different algorithms. (a) FDK, (b) SART, (c) OSSART, (d) ADMMTV, (e) ADMMW.

Results for the integral non-uniformity and the UI evaluated on the reconstructions of the physical phantom are displayed in Tab. 2.

Method	Integral non-uniformity	UI (%)
FDK	0.296	25.26
SART	0.560	23.07
OS–SART	0.454	28.90
ADMM–TV	0.404	30.00
ADMM–W	0.400	29.39

Table 2. Integral non-uniformity and Uniformity Index for each method.

As it could be concluded also visually, SART is the method that performs worst in terms if field uniformity. This agrees with the results of integral non-uniformity, as it owns the highest value for this index. UI seems in contrast with this statement, as SART is characterised by the lowest UI too. Recalling how this index is computed, a low UI means poor difference in CBCT values between a region in the centre of the image and peripheral regions, therefore it is better to keep this index as low as possible; however, looking at the different reconstructions of the uniformity module in Fig. 32, it is easy to see that SART reconstruction is highly affected by noise, which occurs in the same way in all the regions of the selected slice, deteriorating in a similar way both the centre and the periphery of the image. This results in a globally lower UI; however, this is not due to a better image quality, but to a widespread noise that mitigates the differences in shading of the image centre with respect to the periphery. This effect is not present in all the other reconstructions. Considering all these observations we can say that FDK is the method that presents the best performance also in terms of field uniformity, as its UI is the lowest after SART. All methods present a positive UI that means that they are all affected by cupping artefact.

In Fig. 33 the line pair resolution module is showed for each reconstruction algorithm.

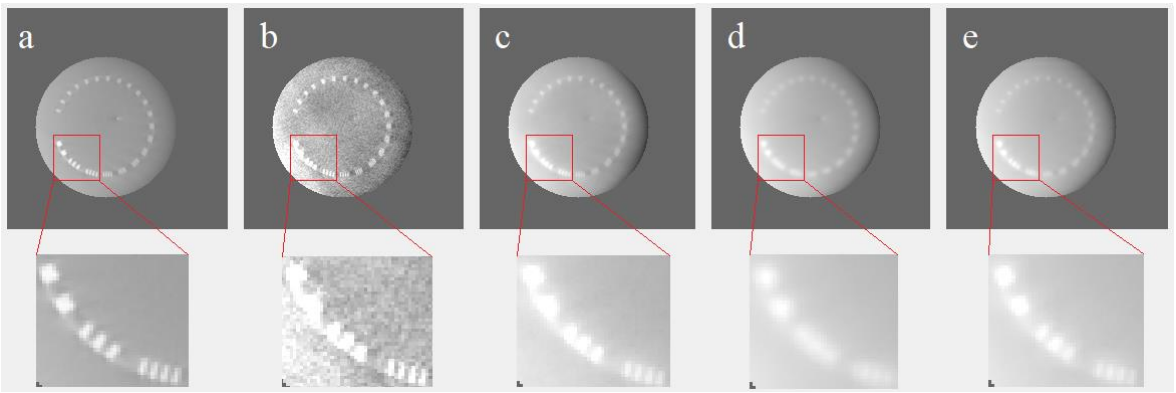

Figure 33. CTP528 spatial resolution module reconstructed with different algorithms. (a) FDK, (b) SART, (c) OSSART, (d) ADMMTV, (e) ADMMW. A detail of the lower resolution line pairs is displayed for each method.

Noise in SART reconstruction could be appreciated also here. All the iterative reconstruction methods present a certain degree of blurring of the line pairs, and this confirms also the results on contrast in Tab. 1. Spatial resolution metric for all the methods is reported in Tab. 3.

Method	Recognised patterns	Accuracy in spatial resolution
FDK	4	73.71 %
SART	4	66.64 %
OS–SART	4	72.05 %
ADMM–TV	1	10 %
ADMM–W	4	63.71 %

Table 3. Spatial resolution results.

Patterns are considered to be recognised when it is possible to clearly distinguish – and therefore, segment – the individual lines that constitutes the pattern. In this case, ADMMTV is the method that shows the worst spatial resolution due to the high level of blurring that characterises its reconstruction, as it could be also seen in Fig. 33. All the other methods performed similarly, with FDK at top. It has to be noticed that the line pairs were manually segmented, so even if this metric seems to be in agreement with the qualitative evaluation that could be visually made looking at the different reconstructions, the quantitative accuracy computed remains highly dependent on the segmentation capabilities of the operator. However, no automatic segmentation method was found to be successful for this purpose.

This first analysis suggests that FDK performs better than all the other presented methods, but a further investigation on patients' dataset is necessary in order to examine the capability of the different algorithms to deal with problems affecting real data, particularly regarding inter-fraction variability. For each patient, CBCT reconstructions are compared with a planning CT that is acquired in a different moment with respect to CBCT projections, and this arises new issues to be considered.

5.2 Patient Study

Fig. 34 and 35 show some sample reconstructions.

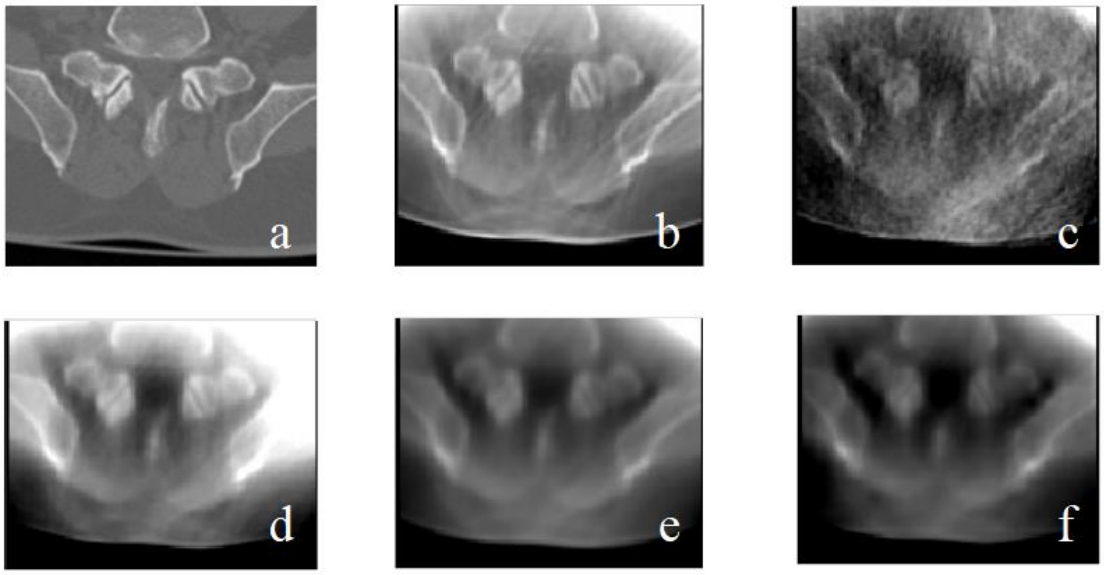

Figure 34. **Example of axial view for different methods.** (a) planning CT, (b) FDK, (c) SART, (d) OS–SART, (e) ADMM–TV, (f) ADMM–W.

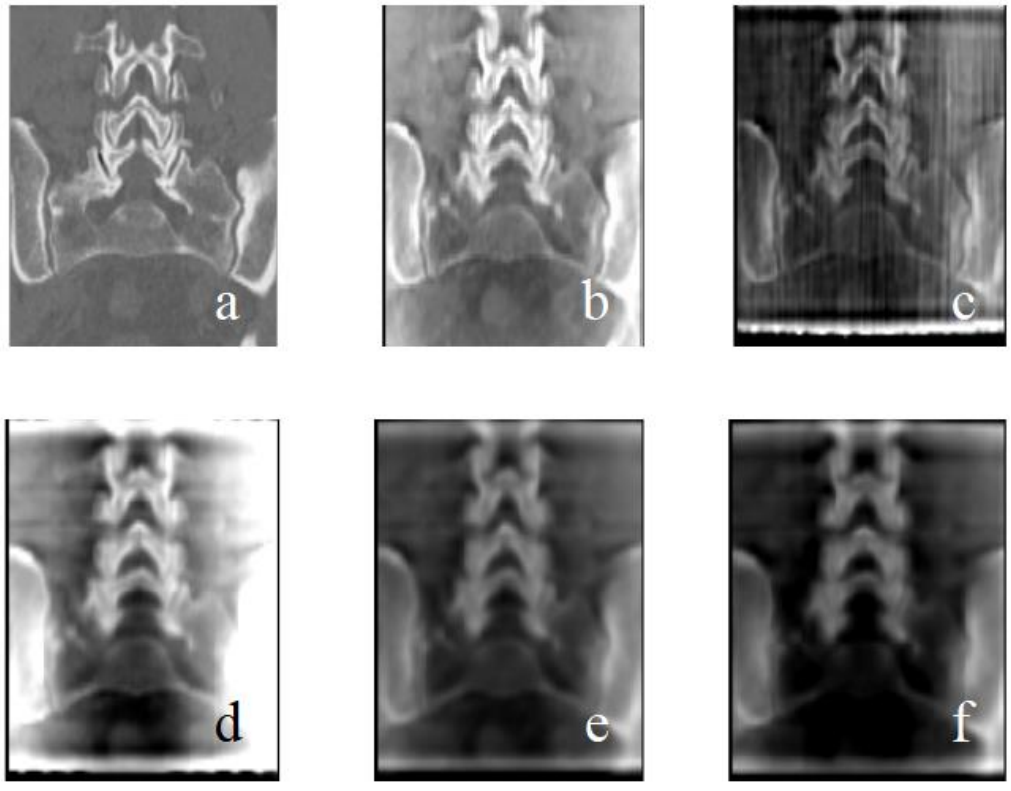

Figure 35. **Example of coronal view for different methods.** (a) planning CT, (b) FDK, (c) SART, (d) OS–SART, (e) ADMM–TV, (f) ADMM–W.

Globally, under the considered conditions, the SART method is characterised by a high degree of noise in the reconstructed image, due to the presence of a line artefact that is propagated by the iterative method (Fig. 36). This artefact is intrinsic in the acquisition since a central metallic spot is present on the detector panel, thus affecting the projection acquisition itself. Future analyses will be based on removing this artefact directly from CBCT projections.

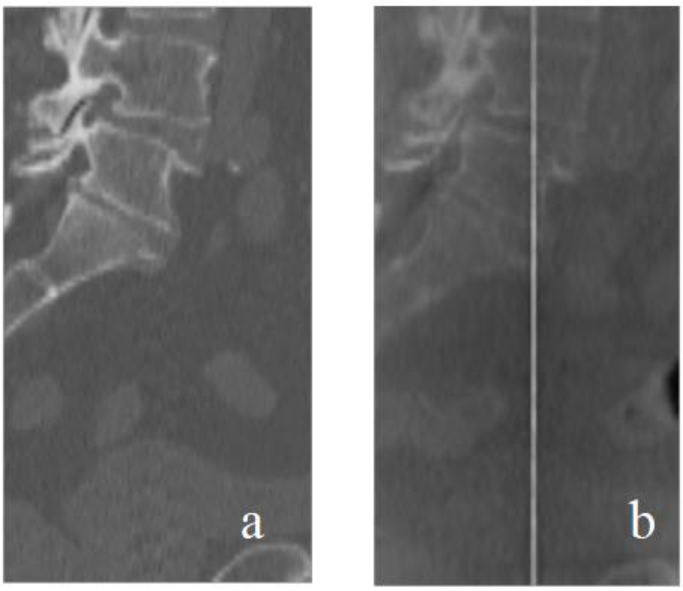

Figure 36. Line artefact. In the reconstructed CBCT (b) appears a line artefact that is not present in planning CT (a) and that propagates in SART method.

In other iterative methods this artefact is not so pronounced, since each of them performs a certain type of regularisation during the reconstruction. Apart from SART, the other methods here also show a higher degree of image blurring with respect to FDK, that visually lowers the quality. Further artefacts also appear at the edges of the image, due to a different manipulation of the projection data that is by its nature truncated in longitudinal direction, as previously said.

Statistical analysis showed that all the metrics populations are not normal with a p-value less than 0.05, except for NMI and PCC evaluated on the global reconstructed volumes, that are normal with p-values of 0.054 and 0.252 respectively, therefore each metric has been evaluated accordingly.

Mutual Information (MI)

Friedman test for MI showed that the only method that results significantly different from others is the SART method (p-value = 3.94e-05). Other algorithms do not show significant differences. Median along with interquartile range (IQR) for each method is reported in Tab. 4.

Patient	MI_FDK	MI_SART	MI_OSSART	MI_ADMMTV	MI_ADMMW
P1	0.60	0.15	0.30	0.26	0.25
P2	0.21	0.13	0.22	0.22	0.20
P3	0.20	0.15	0.22	0.24	0.24
P4	0.71	0.24	0.25	0.25	0.26
P5	0.62	0.38	0.47	0.48	0.47
P6	0.29	0.19	0.31	0.31	0.29
P7	0.51	0.28	0.37	0.39	0.41
P8	0.38	0.27	0.27	0.27	0.27
P9	0.36	0.18	0.31	1.88	0.30
P10	0.48	0.15	0.18	0.19	0.18
P11	0.34	0.18	0.28	0.25	0.26
P12	0.31	0.14	0.14	0.16	0.15
P13	0.16	0.16	0.14	0.20	0.19
Median ± IQR	**0.36 ± 0.27**	0.18 ± 0.10	0.27 ± 0.10	0.25 ± 0.11	0.26 ± 0.10

Table 4. Mutual Information computed on global CBCT reconstructions.

MI_SART shows a lower median with respect to other reconstruction methods, and its difference is due only to its significantly lower performance, as it could be visually verified looking at the different reconstructions in Fig. 34, 35. The other methods do not show a significant difference in global MI, and FDK performs best.

One of the main reasons why SART has significantly lower performance, according to us, is the presence of the line artefact in the projections (Fig. 36). Since the method scans the projections one by one, correcting each time the reconstructed volume to be consistent to them, the presence of the line artefact affects the entire reconstructed volume, generating the vertical bands that are clearly visible in Fig. 34, 35. This happens since no

regularisation is applied. This problem is strongly mitigated, if not completely removed, in the OS–SART variant, where a convenient grouping of the projections manages to neutralise the artefact. ADMM reconstructions show capacities comparable to OS–SART because they lean on other regularisations.

Normalised Mutual Information (NMI)

T-test results for global NMI are reported in Fig. 37.

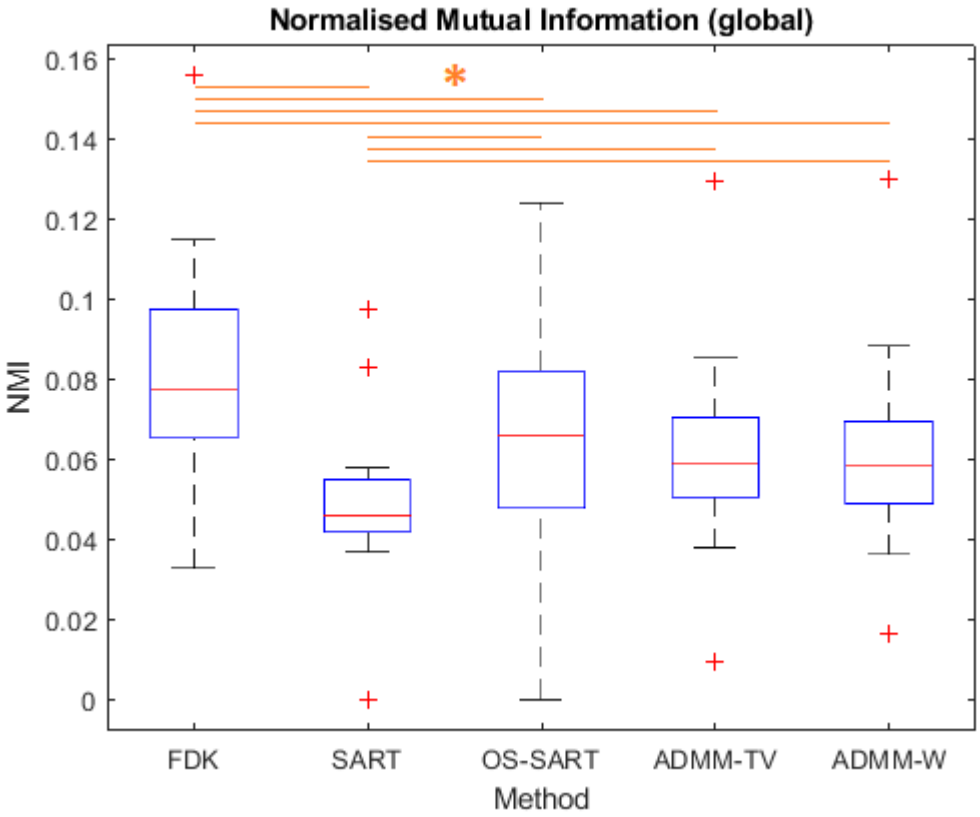

Figure 37. **T-test results for NMI.** Pairs exhibiting a significant difference are marked with an orange line.

Complete data on global NMI, means and standard deviations are reported in Tab. 5.

Patient	NMI_FDK	NMI_SART	NMI_OSSART	NMI_ADMMTV	NMI_ADMMW
P1	0.076	0.040	0.069	0.059	0.059
P2	0.060	0.037	0.054	0.056	0.051
P3	0.055	0.051	0.049	0.053	0.053
P4	0.096	0.058	0.066	0.066	0.066
P5	0.156	0.097	0.124	0.129	0.130
P6	0.068	0.054	0.085	0.072	0.072
P7	0.115	0.083	0.084	0.086	0.088
P8	0.079	0.052	0.054	0.052	0.052
P9	0.077	0.044	0.071	0.068	0.066
P10	0.101	0	0	0.009	0.017
P11	0.090	0.044	0.081	0.070	0.069
P12	0.067	0.046	0.043	0.045	0.043
P13	0.033	0.043	0.034	0.038	0.036
Mean ± std	**0.083 ± 0.031**	0.050 ± 0.023	0.063 ± 0.030	0.062 ± 0.028	0.062 ± 0.027

Table 5. Global NMI data.

NMI_FDK is significantly different with respect to all the other methods, and the higher mean states that it performs significantly better with respect to all the other methods regarding global NMI with planning CT.

This data confirms what has been observed in MI: FDK performs best, while SART is still the method with lowest performance. All the other iterative methods are comparable.

Pearson Correlation Coefficient (PCC)

T-test results for global PCC are reported in Fig. 38.

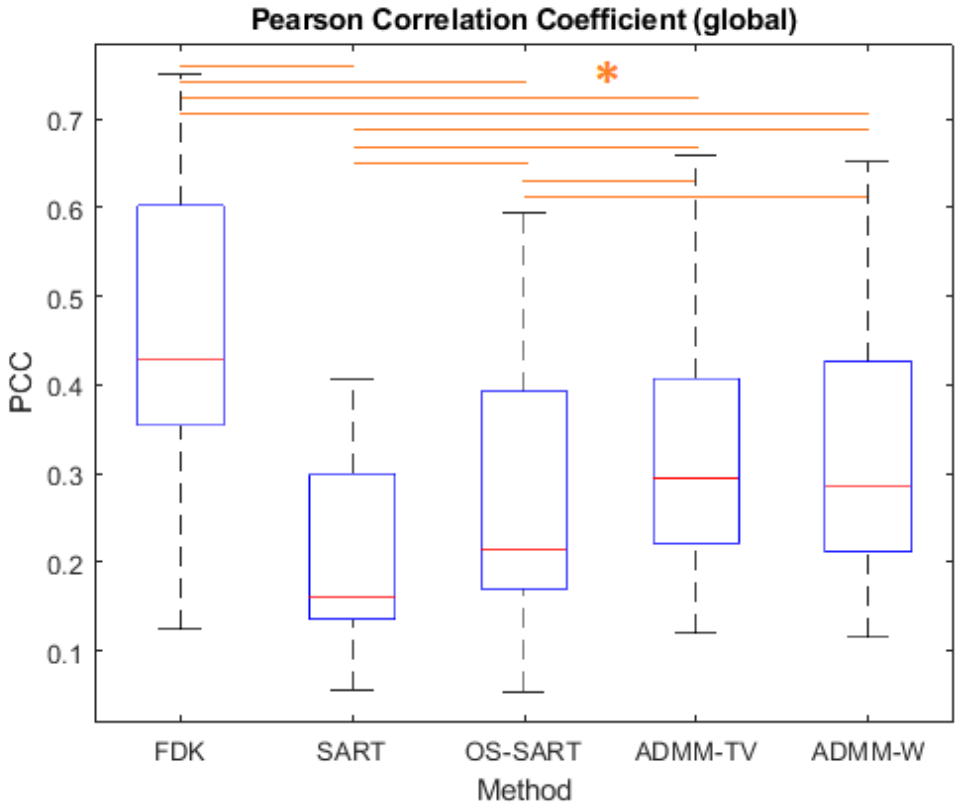

Figure 38. T-test results for PCC. Pairs exhibiting a significant difference are marked with an orange line.

Complete PCC data, means and standard deviations are reported in Tab. 6.

Patient	PCC_FDK	PCC_SART	PCC_OSSART	PCC_ADMMTV	PCC_ADMMW
P1	0.39	0.15	0.21	0.30	0.29
P2	0.23	0.16	0.18	0.21	0.21
P3	0.13	0.14	0.14	0.18	0.17
P4	0.62	0.35	0.39	0.39	0.41
P5	0.75	0.41	0.59	0.66	0.65
P6	0.43	0.24	0.30	0.37	0.37
P7	0.60	0.31	0.46	0.54	0.53
P8	0.60	0.27	0.41	0.47	0.47
P9	0.39	0.30	0.33	0.36	0.36
P10	0.68	0.06	0.05	0.12	0.12
P11	0.55	0.13	0.21	0.27	0.26
P12	0.41	0.10	0.18	0.28	0.27
P13	0.25	0.16	0.15	0.23	0.21
Mean ± std	**0.46 ± 0.19**	0.21 ± 0.11	0.28 ± 0.15	0.34 ± 0.15	0.33 ± 0.15

Table 6. Complete global PCC data.

PCC_FDK is significantly different with respect to all the other methods, and the higher mean states that it performs significantly better. SART and OSSART have significantly lower performances regarding global PCC. ADMM–TV and ADMM–W are comparable.

PCC at the level of the Planned Target Volume (PCC_PTV) and Sigma (PCC_S)

Quantitative evaluation metrics were also performed in the tumour volume (i.e. in the PTV). Specifically, Friedman test for PCC_PTV and PCC_S showed that there are no significant differences between the reconstruction methods in these regions (p-value 0.23 and 0.34 respectively).

Median and IQR for each method are reported in Tab. 7. Complete data for each patient is reported in Appendix 3.

Method	**PCC_PTV FDK**	**PCC_PTV SART**	**PCC_PTV OSSART**	**PCC_PTV ADMMTV**	**PCC_PTV ADMMW**
Median ± IQR	0.28 ± 0.32	0.24 ± 0.33	0.27 ± 0.31	0.27 ± 0.30	0.27 ± 0.30
Method	**PCC_S_FDK**	**PCC_S_SART**	**PCC_S_OSSART**	**PCC_S_ADMMTV**	**PCC_S_ADMMW**
Median ± IQR	0 ± 0.22	0 ± 0.21	0 ± 0.22	0 ± 0.22	0 ± 0.22

Table 7. Summary of the results for PTV (PCC_PTV) and Sigma (PCC_S).

All the methods are comparable in proximity of these regions. The fact that medians are all equal to zero for PCC_S is due to the reduced dimensions of the area (see Fig. 30), that sometimes lead to zeroes in similarity indexes computed at sigma level.

PCC evaluated on rectum (PCC_R)

Friedman test on the PCC_R showed significant differences (p-value = 0.008). SART method is significantly different from both FDK and ADMMTV. No other differences

have been found. PCC_R median and IQR is reported for each method in Tab. 8. Complete data is reported in Appendix 3.

Method	PCC_R_FDK	PCC_R_SART	PCC_R_OSSART	PCC_R_ADMMTV	PCC_R_ADMMW
Median ± IQR	**0.40 ± 0.52**	0.09 ± 0.33	0.34 ± 0.42	0.38 ± 0.42	0.38 ± 0.42

Table 8. Results of the PCC evaluated at the level of the Rectum (PCC_R).

This data confirms the previous considerations: all the iterative methods except SART are comparable and perform worse than FDK on the available data. In this case, the difference between SART and the other ones is highly amplified.

PCC evaluated on bladder (PCC_B)

Friedman test reported significant differences in algorithms performance with a p-value of 1.52×10^{-6}. In Fig. 39 the results of the multiple comparison test. A 5% significance level has been considered.

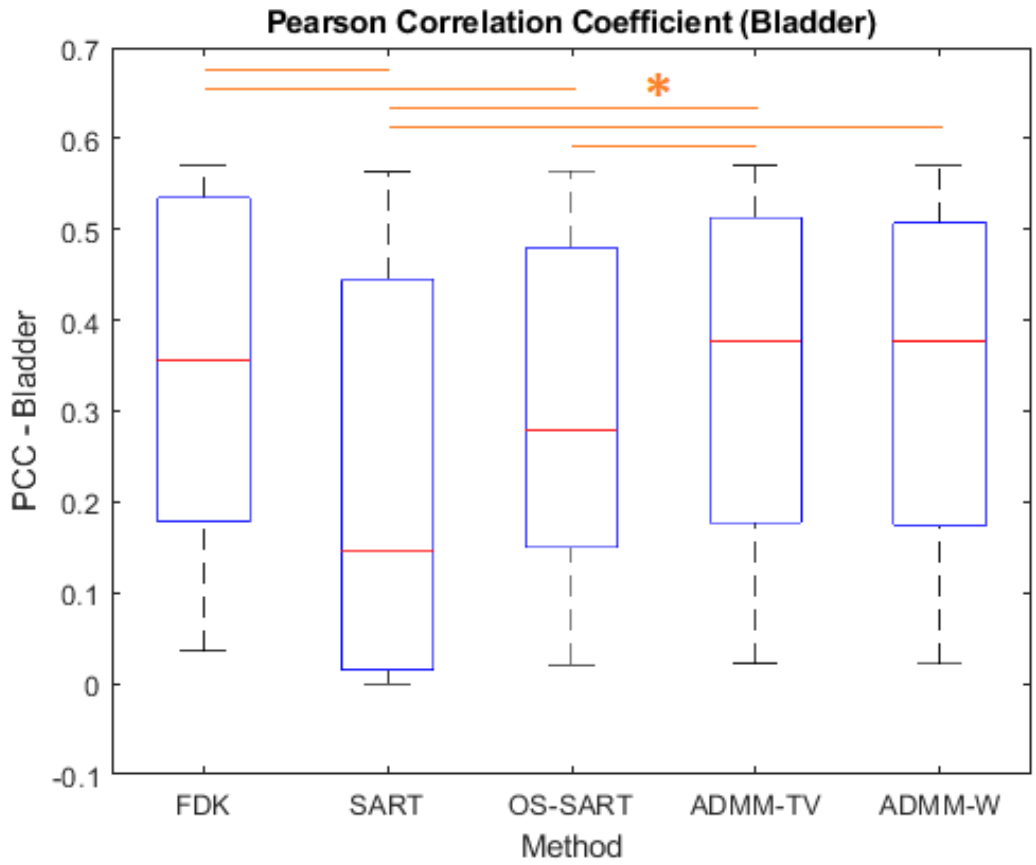

Figure 39. **Friedman test results for PCC evaluated in the Bladder.** Pairs exhibiting a significant difference are marked with an orange line.

Medians and IQRs are reported in Tab. 9. Complete data is reported in Appendix 3.

Method	PCC_B_FDK	PCC_B_SART	PCC_B_OSSART	PCC_B_ADMMTV	PCC_B_ADMMW
Median ± IQR	0.36 ± 0.36	0.15 ± 0.43	0.21 ± 0.33	**0.38 ± 0.34**	**0.38 ± 0.33**

Table 9. **Results on the PCC at the level of the Bladder**.

Interestingly, in this case FDK is not the method with the highest index. ADMM methods both show a higher median, even if statistics does not highlight significant differences between FDK and such algorithms.

In Fig. 40, an FDK and an ADMM–W reconstructions are cropped around the same region to evaluate soft tissues discrimination.

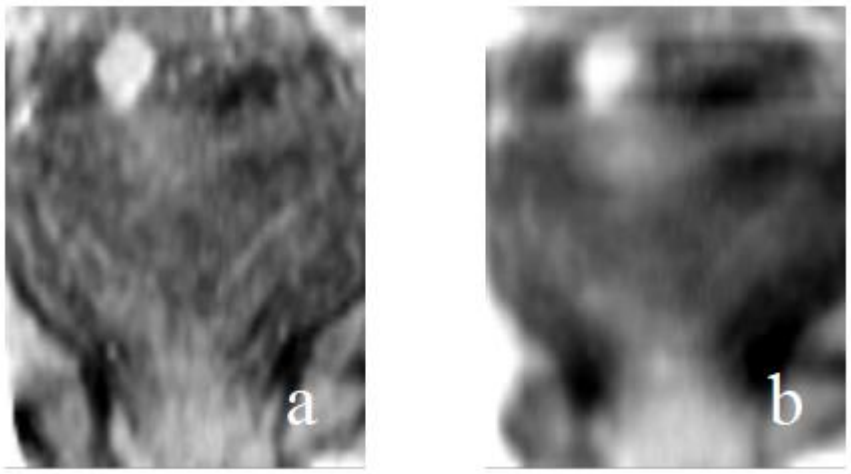

Figure 40. Detail on soft tissues. (a) FDK reconstruction and (b) corresponding ADMM-W reconstruction.

As it could be seen, even if ADMM–W is characterised by a blurring effect in bony regions, the area displayed in the figure suggests that ADMM methods may exhibit a higher contrast in correspondence of soft tissues with reduced noise. Similar considerations are valid also for ADMM–TV.

The introduction of GPU implementation keeps the running time very low for all the reconstruction methods tested. In particular, with the chosen parameters, FDK requires less than 30 seconds; SART, OS–SART and ADMM–TV are in the order of the minute; ADMM–W requires one minute and a half.

Therefore, in this work some alternative iterative reconstruction methods to the classic FDK algorithm were tested and evaluated. From the results obtained, none of the alternative reconstruction methods is significantly better than the algorithm currently implemented at CNAO, that has been proven to be the most effective and efficient in the present conditions.

The considered metrics all seem to be consistent with the results that can be evaluated looking at the reconstructions. PCC has been chosen also to evaluate soft structures since, in our opinion, it presents less zeroes linked to the modest dimensions of the regions considered, and also puts in evidence the different characteristics of the methods in a more complete and correct manner. However, there is no consensus on which the best

representative metric is to evaluate a CBCT reconstruction, even if considering the planning CT as a reference. In this work, we considered some similarity metrics that are considered to be the most appropriate to compare CT and CBCT (Skerl et al, 2006), but at the same time easy to implement and fast to compute to keep the computational demand as low as possible. In any case, it is not clear if the similarity measure that performs best on images of the pelvis would also be the best for other body sites, such as the head or the thorax, as the behaviour of a similarity measure depends not only on the imaging modality but also on image content and image degrading effects. A further investigation on clusters of CNAO patients grouped on the basis of the anatomical district involved could suggest a different metric for each region of the body, even if it has been demonstrated that a combination of different metrics generally leads to high accuracy in similarity evaluation (Skerl et al., 2006).

5.3 2D PROJECTIONS SHADING CORRECTION

After evaluating that no alternative methods showed significantly better performance than the implemented FDK, the correction strategy has been tested on projection data and the FDK reconstruction before and after the correction have been compared. This represents a preliminary analysis, taking into consideration that each step of the method needs a proper optimisation.

In Fig. 41, a sample projection is showed, together with the corresponding virtual CT projection, the estimated scattering, and the corrected projection. The histograms of the different volumes are represented in Fig. 42.

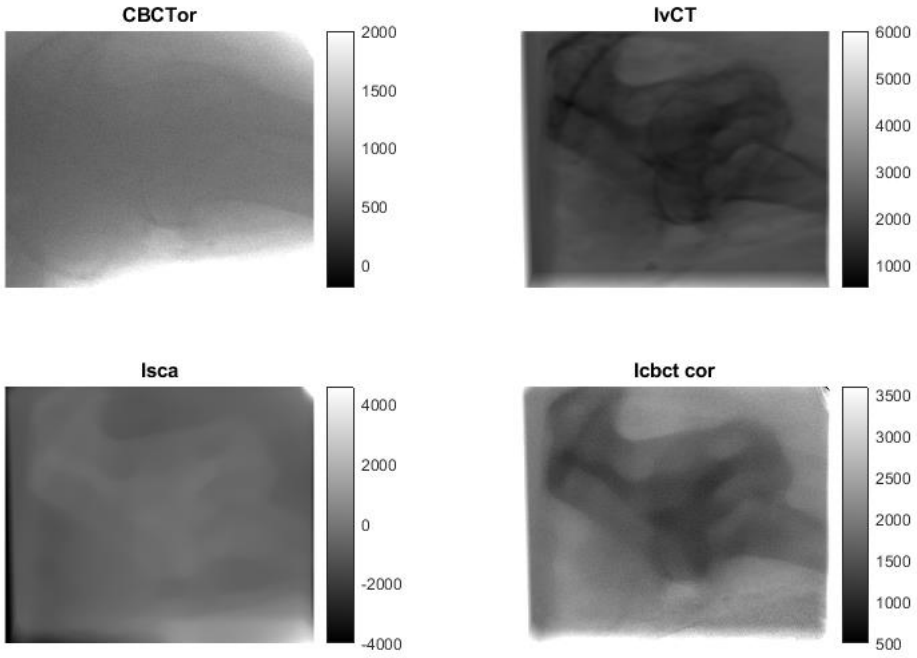

Figure 41. **Projection correction steps.** CBCTor = original CBCT projection, IvCT = virtual CT projection, Isca = estimated scatter, Icbct cor = corrected CBCT projection.

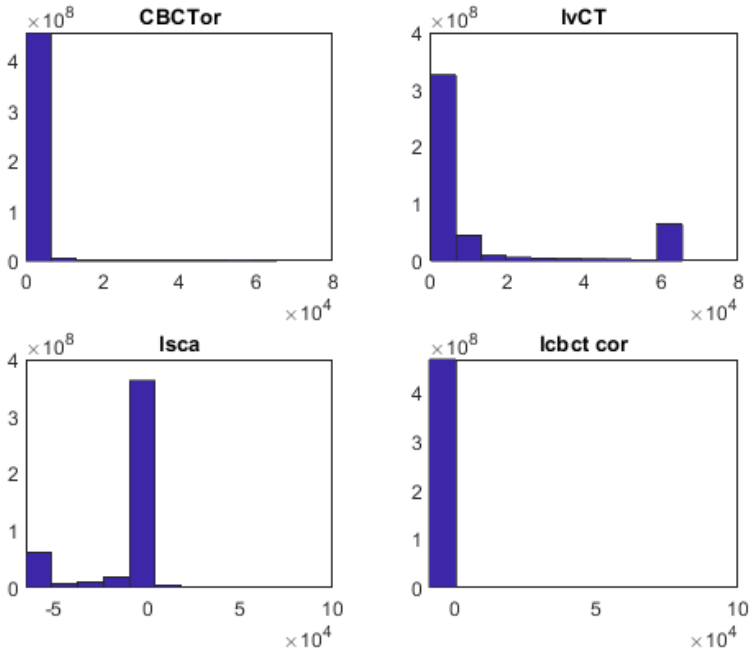

Figure 42. **Histograms of the different volumes.**

A comparison between the original planning CT, and the FDK reconstructions before and after the correction are reported in Fig. 40. The main challenge in this method is to correct the original CBCT reconstruction without altering it. To do so, a proper calibration of the parameters involved in the correction is mandatory. The literature (Niu et al., 2010, Niu et al., 2012, Park et al., 2015) takes into consideration the Elekta CBCT hardware, and no similar analysis have been found regarding Varian system. In this preliminary investigation, the calibration factor that weights the CT contribution found on the Elekta hardware has been used, but this is obviously an approximation, since the Varian CBCT hardware could return a different value. This represent an example, but all the stages of this workflow need a further analysis and optimisation, including the quality of the deformable image registration between CT and CBCT, that strongly affects the effectiveness of the method, especially in those cases where a large deformation of internal organs occurs.

The views that benefit the most from this correction are the sagittal and the coronal ones. In Fig. 43 and 44 it can be observed how the artefacts due to the gantry are attenuated, and how the anatomy near the spinal region is clearer in the corrected reconstruction. The overall image appears to be less noisy and the soft tissues are better contrasted.

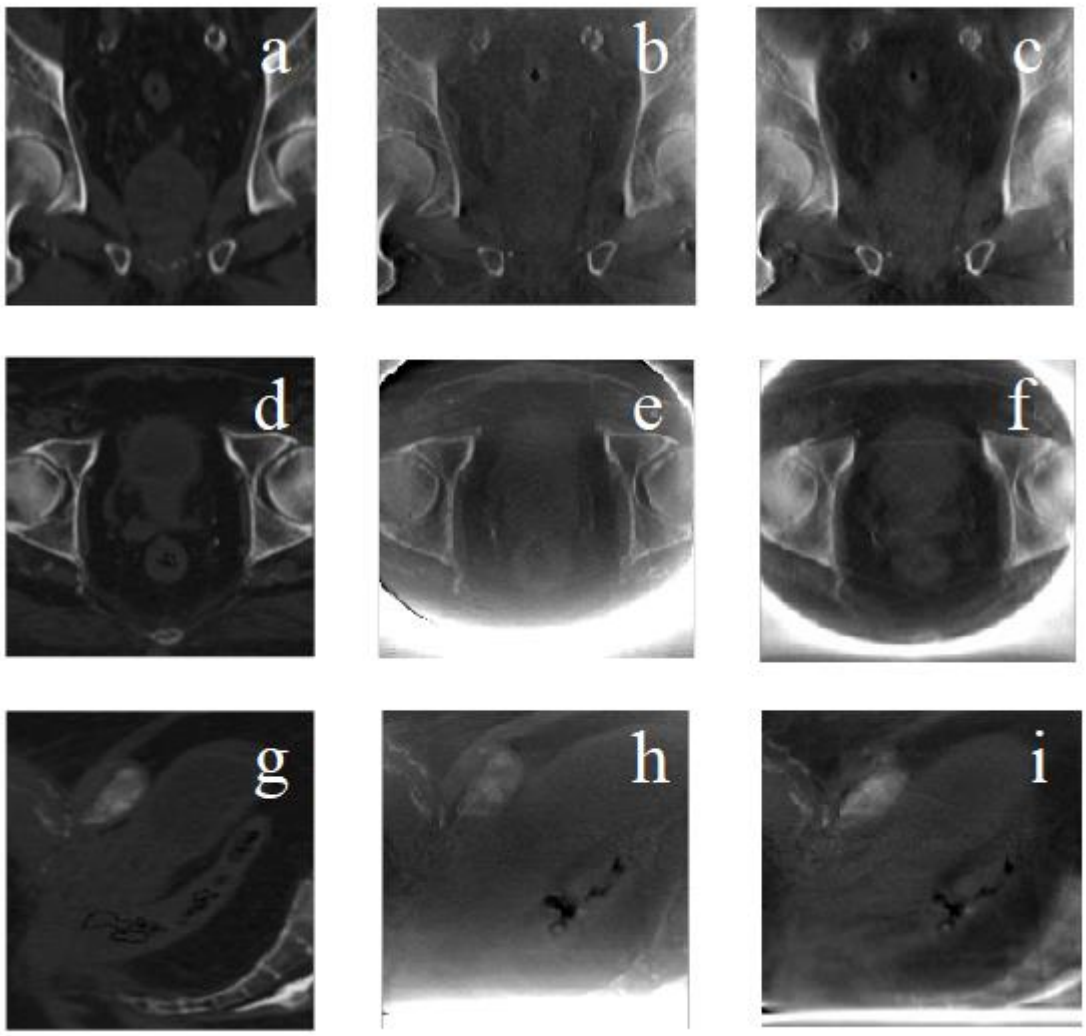

Figure 43. **Sample correction**. (a), (d), (g) are the virtual CT views; (b), (e) and (h) are the original CBCT; (c), (f) and (i) represent the corrected CBCT.

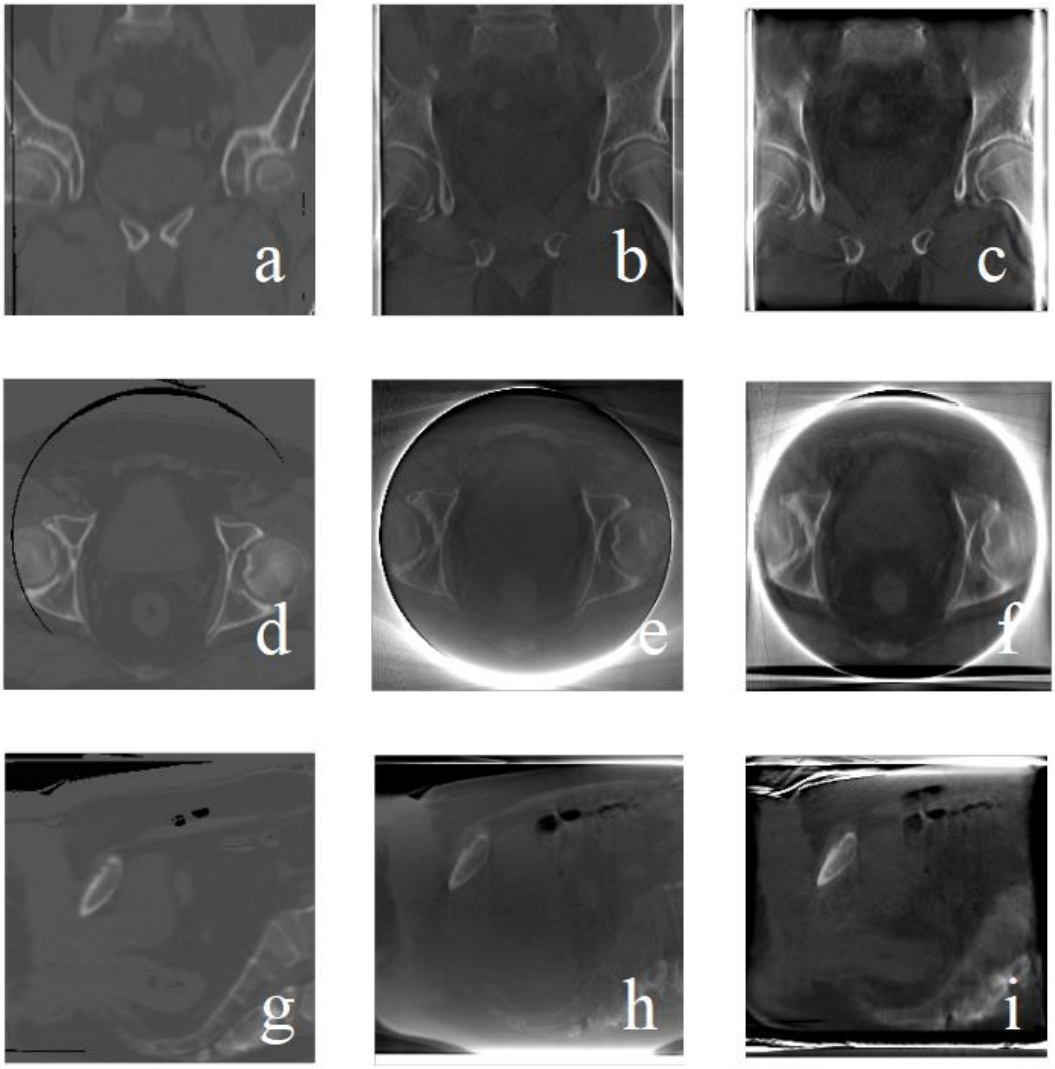

Figure 44. Sample correction. (a), (d), (g) are the virtual CT views; (b), (e) and (h) are the original CBCT; (c), (f) and (i) represent the corrected CBCT. In this case the artefacts at the edges are clearly visible, as well as the false gas pockets in the virtual CT created to match CBCT.

In Fig. 45, a detail on a rectum before and after the gas pockets correction is reported. In this case, a further step to compensate the presence of air pockets in the planning CT that weren't present in the corresponding CBCT was necessary, since the deformable registration algorithm at present is not able to manage such differences in gas filling of internal organs (Niu et al., 2010, Niu et al., 2012). Skipping this step means the generation of false gas pockets in the corrected CBCT solely due to their presence in the planning CT, and this at the moment is the only way to solve this issue.

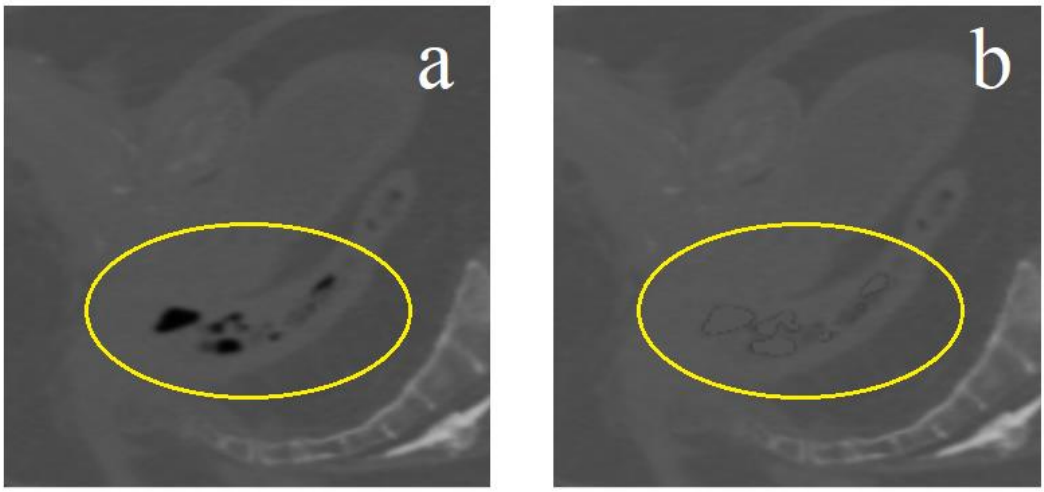

Figure 45. **Gas pockets correction.** (a) Air pockets in the original planning CT and (b) corresponding corrected region in the virtual CT.

In Tab. 10, the values of global MI, NMI and PCC for FDK reconstructions after the 2D projections shading corrections are reported for comparison purposes. When the value after correction is higher, it is reported in bold.

Patient	MI_CORR	NMI_CORR	PCC_CORR
P1	0.44	**0.09**	0.33
P2	**0.39**	**0.08**	0.21
P3	**0.50**	**0.10**	**0.24**
P4	**0.89**	**0.15**	0.23
P5	0.62	**0.17**	**0.78**
P6	**0.62**	**0.14**	**0.54**
P7	0.44	**0.12**	0.35
P8	**0.75**	**0.15**	**0.63**
P9	**0.53**	**0.11**	**0.40**
P10	0.34	0.09	0.22
P11	0.20	0.04	0.0
P12	**0.45**	**0.08**	0.18
P13	**0.58**	**0.14**	0.15

Table 10. **Global MI, NMI and PCC evaluated on the corrected FDK reconstructions**.

The results of this method on CNAO data are only preliminary since all the phases of the pipeline must be individually tested and optimised. In fact, the method is obviously strongly influenced by the quality of the deformable registration between the planning CT and the reconstructed CBCT. This is an important problem when analysing the pelvic region, since a recurrent issue in these cases is the presence of organs such as the rectum or bladder that can undergo important geometric variations, or in the specific example of the rectum, can be filled with air or not. Identifying a deformable registration algorithm that takes these problems into account and is able to correct them still needs to be better investigated and optimised.

Furthermore, in this work the conversion shown in Park et al., 2015, has been followed, but a true calibration on the devices under examination has not yet been carried out, and as already mentioned it is an important future development to be considered not only for a problem of reconstruction quality, which the clinician can use to better identify the structures of interest immediately before treatment, but for all previously listed ART applications, in particular with regard to dose recalculation, which relies heavily on estimated HU values starting from CBCT.

Also, the calibration factor used is a literature value that has not been validated on the system in use by CNAO, and this could certainly be a possible way to improve the efficiency of the correction, since the literature that involves this type of correction largely uses Elekta devices, but a similar analysis on Varian systems is not yet present.

For a preliminary evaluation of the corrected reconstructions, the global indices used to compare the different reconstruction algorithms have been recalculated. This is obviously a first approach, but we must consider that clearly this measure is affected by bias, since using the CT as a prior certainly helps to improve the coefficients that correlate this planning CT to the reconstructed CBCT, but it is a way to verify the behaviour of the method on CNAO data and here it is exploited to emphasize the need to define so-called "blind" metrics for reconstruction quality, i.e. metrics that do not refer to a reference image, as do the "full reference" methods mentioned in this work (MI, NMI, correlation coefficients). These first results, according to those in the literature, seem to be promising, even if it has to be noticed that the main limit of it, apart from the need to optimise the whole process, is that the algorithm has a fairly high computational cost, since the

correction of around 600 projections requires a time in the order of an hour for each patient, and also the process should be made automatic if implemented for clinical use.

6. CONCLUSIONS

Hadrontherapy is an oncological treatment that is gaining more and more importance in recent years, and consequently a series of technologies designed to guarantee precise and efficient treatments are constantly developing. In this work different CBCT reconstruction algorithms alternative to the FDK method implemented at CNAO have been tested. No significant evidence of an improvement with respect to the clinically implemented method was found, but some results suggest that a further optimisation of the iterative reconstructions parameters, which today represents an entire field of research by itself, could lead to an improvement in some characteristics of the reconstructed image, first of all image contrast near organs at risk. A clinical opinion in this sense could guide the choice of an alternative method, for example only to visualise some regions of interest constituted by soft tissues, especially in some anatomical regions where organs may be subjected to relevant inter-fractional changes. Additionally, a method present in the literature was tested for the correction of the CBCT projections before image reconstruction. Although a great effort must still be made to optimise all the phases of the method – and in particular to obtain a reliable calibration between the CBCT values and the planning CT HUs – the results seem promising. These suggest an improvement of the quality of the reconstructed image, which could potentially be at the basis for the implementation of an ART workflow directly performed on the CBCT reconstruction itself. This correction is worth further investigation.

APPENDIX 1 – UPDATED LIST OF CENTRES DELIVERING HADRONTHERAPY

Country	Who, Where	Particle	Start of treatment
Austria	MedAustron, Wiener Neustadt	p&C-ion	2017
Austria	MedAustron, Wiener Neustadt	C-ion	2017
Canada	TRIUMF, Vancouver	p	1995
Czech Rep.	PTC Czech r.s.o., Prague	p	2012
China	WPTC, Wanjie, Zi-Bo	p	2004
China	IMP-CAS, Lanzhou	C-ion	2006
China	SPHIC, Shanghai	p	2014
China	SPHIC, Shanghai	C-ion	2014
China	SPHIC, Shanghai	p&C-ion	2014
Denmark	Dansk Center for Partikelterapi, Aarhus	p	2019
England	Clatterbridge	p	1989
England	Proton Partner's Rutherford CC, Newport	p	2018
England	The Christie Proton Therapy Centre, Manchester	p	2018
France	CAL/IMPT, Nice	p	1991, 2016
France	CPO, Orsay	p	1991, 2014
France	CYCLHAD, Caen	p	2018
Germany	HZB, Berlin	p	1998
Germany	RPTC, Munich	p	2009
Germany	HIT, Heidelberg	p	2009, 2012
Germany	HIT, Heidelberg	C-ion	2009, 2012
Germany	WPE, Essen	p	2013
Germany	UPTD, Dresden	p	2014
Germany	MIT, Marburg	p	2015
Germany	MIT, Marburg	C-ion	2015
India	Apollo Hospitals PTC, Chennai	p	2019
Italy	INFN-LNS, Catania	p	2002
Italy	CNAO, Pavia	p	2011
Italy	CNAO, Pavia	C-ion	2012
Italy	APSS, Trento	p	2014
Japan	HIMAC, Chiba	C-ion	1994, 2017
Japan	NCC, Kashiwa	p	1998
Japan	HIBMC, Hyogo	p	2001

Japan	HIBMC, Hyogo	C-ion	2002
Japan	PMRC2, Tsukuba	p	2001
Japan	Shizuoka Cancer Centre	p	2003
Japan	STPC, Koriyama-City	p	2008
Japan	GHMC, Gunma	C-ion	2010
Japan	MPTRC, Ibusuki	p	2011
Japan	Fukui Prefectural Hospital PTC, Fukui City	p	2011
Japan	Nagoya PTC, Nagoya City, Aichi	p	2013
Japan	SAGA-HIMAT, Tosu	C-ion	2013
Japan	Hokkaido Univ. Hospital PBTC, Hokkaido	P	2014
Japan	Aizawa Hospital PTC, Nagano	P	2014
Japan	i-Rock Kanagawa Cancer Center, Yokohama	C-ion	2015
Japan	Tsuyama Chuo Hospital, Okayama	P	2016
Japan	Hakuhokai Group Osaka PT Clinic, Osaka	P	2017
Japan	Kobe Proton Center, Kobe	P	2017
Japan	Narita Memorial Proton Center, Toyohashi	P	2018
Japan	Osaka Heavy Ion Therapy Center	C-ion	2018
Poland	IFJ PAN, Krakow	P	2011, 2016
Russia	ITEP, Moscow	P	1969
Russia	JINR2, Dubna	P	1999
Russia	MIBS, Saint-Petersburg	P	2018
South Africa	NRF, iThemba Labs	P	1993
South Korea	KNCC, Ilsan	P	2007
South Korea	Samsung PTC, Seoul	P	2016
Sweden	The Skandion Clinic, Uppsala	P	2015
Switzerland	CPT, PSI, Villigen	P	1984, 1996, 2013, 2018
Taiwan	Chang Gung Memorial Hospital, Taipei	P	2015
Netherlands	UMC PTC, Groningen	P	2018
Netherlands	HollandPTC, Delft	P	2018
Netherlands	ZON PTC, Maastricht	P	2019
USA, CA	J. Slater PTC, Loma Linda	P	1990
USA, CA	UCSF-CNL, San Francisco	P	1994
USA, MA	MGH Francis H. Burr PTC, Boston	P	2001
USA, TX	MD Anderson Cancer Center, Houston	P	2006
USA, FL	UFHPTI, Jacksonville	P	2006
USA, OK	ProCure PTC, Oklahoma City	P	2009

USA, PA	Roberts PTC,UPenn, Philadelphia	P	2010
USA, IL	Chicago Proton Center, Warrenville	P	2010
USA, VA	HUPTI, Hampton	P	2010
USA, NJ	ProCure Proton Therapy Center, Somerset	P	2012
USA, WA	SCCA ProCure Proton Therapy Center, Seattle	P	2013
USA, MO	S. Lee Kling PTC, Barnes Jewish Hospital, St. Louis	P	2013
USA, TN	ProVision Cancer Cares Proton Therapy Center, Knoxville	P	2014
USA, CA	California Protons Cancer Therapy Center, San Diego	P	2014
USA, LA	Willis Knighton Proton Therapy Cancer Center, Shreveport	P	2014
USA, FL	Ackerman Cancer Center, Jacksonville	P	2015
USA, MN	Mayo Clinic Proton Beam Therapy Center, Rochester	P	2015
USA, NJ	Laurie Proton Center of Robert Wood Johnson Univ. Hospital, New Brunswick	P	2015
USA, TX	Texas Center for Proton Therapy, Irving	P	2015
USA, TN	St. Jude Red Frog Events Proton Therapy Center, Memphis	P	2015
USA, AZ	Mayo Clinic Proton Therapy Center, Phoenix	P	2016
USA, MD	Maryland Proton Treatment Center, Baltimore	P	2016
USA, FL	Orlando Health PTC, Orlando	P	2016
USA, OH	UH Sideman CC, Cleveland	P	2016
USA, OH	Cincinnati Children's Proton Therapy Center, Cincinnati	P	2016
USA, MI	Beaumont Health Proton Therapy Center, Royal Oak, Detroit	P	2017
USA, FL	Baptist Hospital's Cancer Insitute PTC, Miami	P	2017
USA, DC	MedStar Georgetown University Hospital PTC, Washington D.C.	P	2018
USA, TN	Provision CARES PTC, Nashville	P	2018
USA, GA	Emory Proton Therapy Center, Atlanta	P	2018
USA, OK	Stephenson Cancer Center, Oklahoma	P	2019

APPENDIX 2 – RECONSTRUCTIONS PARAMETERS

FDK RECONSTRUCTION

Name	Description	value
AIR_THRESHOLD	The scatter correction algorithm implemented in RTK is based on the work of Boellaard et al., 1997. It assumes a homogeneous contribution of scatter which is computed depending on the amount of tissues traversed by x-rays. The parameter sets the air threshold on projection images. The threshold is used to evaluate which part of the x-rays have traversed the patient.	16000
SPR	Sets the scatter-to-primary ratio on projection images. This is used to measure the scatter level on the projection image from the total measure signal. The primary dose is that part of the transmission or exit dose delivered by photons that has reached a given point without interaction. The scattered dose is defined as the remaining part of the transmission or exit dose, which is caused by scattered radiation. The Scatter to Primary Ratio (SPR) is defined as the energy of the scattered radiation (S) divided by the energy of primary beam (P) striking the same point on the imaging device. If the SPR equals 1 there is as much scatter radiation as there is primary radiation forming the image of the object being radiographed.	0.999
HANN_CUT_FREQ	One might want to use a Hann windowing of the ramp filter to reduce the noise amplification effect of high-pass filtering. Note that the argument is a cut-off frequency, so smaller values mean more smoothing.	0.4
HANN_CUT_FREQ_Y	Same on y axis	0.4
SUBSET OF PROJECTIONS	Set the number of cone-beam projection images processed simultaneously. Default is 4.	16
STREAMING CHANNELS	Pipeline object to control data streaming for large datasets. This will divide the output into several pieces, and call the upstream pipeline for each piece, tiling the individual	1

	outputs into one large output. This reduces the memory footprint for the application since each filter does not have to process the entire dataset at once. This filter will produce the entire output as one image, but the upstream filters will do their processing in pieces.	

SART AND OS–SART RECONSTRUCTIONS

Number Of Iterations	Set the number of iterations. Default is 3.	1
Lambda	Set the convergence factor. Default is 0.3.	0.3
Back-Projection Filter	Set the backprojection filter type. 0: voxel based 1: Joseph 2: cuda voxel based 3: cuda raycast 4: Joseph attenuated	2
Forward Projection Filter	Set the forward projection filter type. 0: Joseph 1: cuda raycast 2: Joseph attenuated	1
Number Of Projections Per Subset	Set the number of projections per subset. Default is 1.	6

ADMM–TV RECONSTRUCTION

Alpha	Set alpha coefficient.	100
Beta	Set beta coefficient.	1500
AL iterations	Set the number of iterations for Augmented Lagrangian step.	6
CG iterations	Set the number of iterations for Conjugate Gradient step.	2

ADMM–W RECONSTRUCTION

Number Of Levels	Set the number of levels for wavelet decomposition.	3
Set Order	Set order of wavelet decomposition.	3

APPENDIX 3 – DETAIL OF THE INDEXES EVALUATED ON STRUCTURES OF INTEREST

PCC EVALUATED ON PTV

Patient	PCC_PTV_FDK	PCC_PTV_SART	PCC_PTV_OSSART	PCC_PTV_ADMMTV	PCC_PTV_ADMMW
P1	0	0	0	0	0
P2	0.13	0	0.05	0.12	0.12
P3	0.39	0.51	0.37	0.39	0.39
P4	0.35	0.24	0.29	0.30	0.30
P5	0.29	0.30	0.29	0.29	0.29
P6	0.06	0.07	0.07	0.07	0.07
P7	0.05	0.07	0.06	0.05	0.05
P8	0.41	0.34	0.42	0.40	0.40
P9	0.21	0.23	0.20	0.23	0.23
P10	0.63	0.61	0.62	0.63	0.63
P11	0	0	0	0	0
P12	0.28	0.36	0.27	0.27	0.27
P13	0.37	0.42	0.37	0.37	0.37

PCC EVALUATED ON SIGMA

Patient	PCC_S_FDK	PCC_S_SART	PCC_S_OSSART	PCC_S_ADMMTV	PCC_S_ADMMW
P1	0.280	0.266	0.277	0.278	0.277
P2	0	0	0	0	0
P3	0	0	0	0	0
P4	0	0	0	0	0
P5	0	0	0	0	0
P6	0.157	0.159	0.162	0.158	0.158
P8	0.479	0.480	0.473	0.477	0.478
P9	0.013	0.014	0.008	0.008	0.008
P10	0	0	0	0	0
P11	0	0	0	0	0
P12	0.686	0.702	0.683	0.684	0.684
P13	0	0	0	0	0

PCC EVALUATED ON THE RECTUM

Patient	PCC_R_FDK	PCC_R_SART	PCC_R_OSSART	PCC_R_ADMMTV	PCC_R_ADMMW
P1	0.54	0.06	0.37	0.47	0.47
P2	0.39	0.27	0.33	0.38	0.38
P3	0.64	0.63	0.65	0.65	0.65
P4	0	0	0	0	0
P5	0	0.42	0.47	0.44	0.42
P6	0	0	0	0	0
P8	0.50	0.02	0.14	0.35	0.32
P9	0.46	0.46	0.46	0.46	0.46
P10	0.15	0	0.04	0.09	0.08
P11	0.41	0.16	0.34	0.39	0.38
P12	0.59	0.12	0.43	0.55	0.54
P13	0	0.03	0	0	0

PCC EVALUATED ON THE BLADDER

Patient	PCC_B_FDK	PCC_B_SART	PCC_B_OSSART	PCC_B_ADMMTV	PCC_B_ADMMW
P1	0.57	0.56	0.56	0.57	0.57
P2	0.57	0.56	0.56	0.57	0.57
P3	0.36	0.36	0.36	0.36	0.36
P4	0.35	0	0.31	0.40	0.40
P5	0.15	0.03	0.09	0.13	0.13
P6	0.54	0.53	0.54	0.54	0.54
P8	0.46	0	0.23	0.40	0.40
P9	0.09	0.10	0.09	0.10	0.10
P10	0.27	0.24	0.25	0.25	0.25
P11	0.04	0	0.02	0.02	0.02
P12	0.21	0.08	0.21	0.23	0.22
P13	0.53	0.19	0.42	0.49	0.48

BIBLIOGRAPHY

Afonso, M. V., Bioucas-Dias, J. M., Figueiredo, M. A. T. (2011). An augmented lagrangian approach to the constrained optimization formulation of imaging inverse problems. *IEEE Transactions on Image Processing, 20*(3): 681–695.

Amaldi, U., Tosi, G. (1991). Per un centro di teleterapia con adroni. *Vol. TERA 91/1 GEN*, 1.

Amaldi, U., Kraft, G. (2005). Radiotherapy with beams of carbon ions. *Reports on Progress in Physics, 68*(8):1861–1882.

Amaldi, U., Magrin, G. (2010). *The path to the Italian national centre for ion therapy*. Vercelli, Italy, Edizioni Mercurio.

Andersen, A. H., Kak, A. C. (1984). Simultaneous Algebraic Reconstruction Technique (SART): A superior implementation of the ART algorithm. *Ultrasonic Imaging, 6*(1): 81–94.

Badano, L., Benedikt, M., Bryant, P. J., Crescenti, M., Holy, P., Knaus, P., Meier, A., Pullia, M., Rossi, S. (1999). Proton–Ion Medical Machine Study (PIMMS). Part I, *CERN/PS,* 10:2000–007.

Badano, L., Benedikt, M., Bryant, P. J., Crescenti, M., Holy, P., Knaus, P., Meier, A., Pullia, M., Rossi, S. (2000). Proton-Ion Medical Machine Study (PIMMS) – Part II. *CERN/PS,* 7.

Baker, G.R. (2006). Localization: conventional and CT simulation. *Brit J Radiol,, 79*(Special Issue 1), S36–S49.

Barry, A., Loredana, M., Eva, B. (2012). *Biomedical physics in radiotherapy for cancer*. Collingwood (VIC): CSIRO Publishers.

Bertram, M., Sattel, T., Hohmann, S., Wiegert, J. (2008). Monte-Carlo scatter correction for cone-beam computed tomography with limited scan field-of-view. *Proc. SPIE 6913, Medical Imaging 2008: Physics of Medical Imaging*, 69131Y. 2008. San Diego, CA.

Bissonnette, J., Moseley, D. J. and Jaffray, D. A. (2008). A quality assurance program for image quality of cone-beam CT guidance in radiation therapy. *Med. Phys.*, *35*: 1807-1815.

Boda-Heggemann, J., Lohr, F., Wenz, F., Flentje, M., Guckenberger, M. (2011). kV cone-beam CT-based IGRT. *Strahlenther Onkol*, *187*(5), 284–291.

Boellaard, R., van Herk, M., Mijnheer, B. J. (1998). A convolution model to covnvert transmission dose images to exit dose distributions. *Med. Phys.*, *24:* 189–199.

Brock, K. K., Sharpe, M. B., Dawson, L. A., Kim, S. M., Jaffray, D. A. (2005). Accuracy of finite element model-based multi-organ deformable image registration. *Med. Phys. 32*, 1647–1659.

Castelli, J., Simon, A., Lafond, C., Perichon, N., Rigaud, B., Chajon, E., De Bari, B., Ozsahin, M., Bourhis, J., de Crevoisier, R. (2018). *Acta Oncol.*, *57*(10): 1284–1292.

Coutrakon, G., Cortese, J., Ghebremedhin A., Hubbard, J., Johanning, J., Koss, P., Maudsley, G., Slater, C. R., Zuccarelli, C., Robertson, J. (1997). Microdosimetry spectra of the Loma Linda proton beam and relative biological effectiveness comparisons. *Medical Physics,24*:1499–1506.

Cover, T.M., Thomas, J.A. (1991). *Elements of Information Theory* (Wiley ed.).

Cuttone, G., Cirrone, G. A. P., Di Franco, G., La Monaca, V., Lo Nigro, S., Pittera, S., et al. (2011). CATANA protontherapy facility: the state of art of clinical and dosimetric experience. *Eur Phys J Plus* 126:1–7.

Desplanques, M., Tagaste, B., Fontana, G., Pella, A., Riboldi, M., Fattori, G., Donno, A., Baroni, G., Oreccchia, R. (2013). A comparative study between the imaging system and the optical tracking system in proton therapy at CNAO. *J Radiat Res July 54*(Suppl. 1):129e35.

Dickie, C., Parent, A., Griffin, A. M., Wunder, J., Ferguson, P., Chung, P. W., Craig, T., Sharpe, M., Becker, N., Shultz, D., Catton, C. N., O'Sullivan, B. (2017). The value of adaptive preoperative radiotherapy in management of soft tissue sarcoma. *Radiother Oncol., 122*(3): 458–463.

Ding., G. X., Duggan, D. M., Coffey, C. W., Deeley, M., Hallahan, D. E., Cmelak, A., Malcom, A. (2007). A study on adaptive IMRT treatment planning using kV cone-beam CT. *Radiother Oncol., 85*(1): 116–125.

Durante, M., Orecchia, R., Loeffler, J. S. (2017). Charged-particle therapy in cancer: clinical uses and future perspectives. *Nature Reviews Clinical Oncology, 14*(8), 483–495.

Elstrøm, U. V., Muren, L. P., Petersen, J. B. B., Grau, C. (2011). Evaluation of image quality for different kV cone-beam CT acquisition and reconstruction methods in the head and neck region. *Acta Oncol 50*(6): 908–17.

Engelsman, M., Schwarz, M., Dong, L. (2013). Physics controversies in proton therapy. *Semin Radiat Oncol* 23: 88–96.

Fattori, G. (2010). *Implementazione e validazione di metodi di registrazione automatica per il posizionamento e monitoraggio del paziente in adroterapia* (Master thesis).

Frigerio, A. (2011). *La gestione strategica della manutenzione e i flussi informativi in edifici caratterizzati da un'elevata specificità e complessità: il caso CNAO* (Master thesis).

Feldkamp, L. A., Davis, L. C., Kress, J. W. (1984). Practical cone-beam algorithm. *J Opt Soc Am A 1*(6): 612–19.

Foroudi, F., Wong, J., Kron, T. et al. (2011). Online adaptive radiotherapy for muscle-invasive bladder cancer: results of a pilot study. *Int J Rad Oncol Biol Phys 81*(3): 765–71

Garayoa, J., Castro, P. (2013). A study on image quality provided by a kilovoltage cone-beam computed tomography. *J Appl Clin Med Phys 14*(1): 3888.

Graff G., Sidky E. Y. (2015). Compressive sensing in medical imaging. *Appl. Opt. 54*(8): C23–C44.

Groh, B.A., Siewerdsen, J.H., Drake, D. G., Wong, J. W., Jaffray, D.A. (2002). A performance comparison of flat-panel imager-based MV and kV cone-beam CT. *Med Phys 29*(6): 967–75.

Guerquin-Kern, M., Van De Ville, D., Vonesch, C., Baritaux, J. C., Pruessmann, K. L., Unser, M. (2009). Wavelet-regularized reconstruction for rapid MRI. *IEEE International Symposium on Biomedical Imaging: 193–196.*

Han, T. S. (1978). Nonnegative entropy measures of multivariate symmetric correlations, *Information and Control* 36, 133–156.

Hansen, D. C., Landry, G., Kamp, F., Li, M., Belka, C., Parodi, K, Kurz, C. (2018). ScatterNet: A convolutional neural network for cone-beam CT intensity correction. *Med Phys 45*(11): 4916–4926.

Hatton, J., McCurdy, B., Greer, P. B. (2009). Cone beam computerized tomography: the effect of calibration of the Hounsfield unit number to electron density on dose calculation accuracy for adaptive radiation therapy. *Phys. Med. Biol., 54*(15): N329–46.

Hua, C., Yao, W., Kidani, T., Tomida, K., Ozawa, S., Nishimura, T., et al. (2017). A robotic C-arm cone beam CT system for image-guided proton therapy: design and performance. *Br J Radiol*. 90: 20170266.

ICRU Report 62. (1999). Prescribing, recording, and reporting photon beam therapy. Bethesda (MD).

Jaffray D. A., Siewerdsen, J. (2000). Cone-beam computed tomography with a flat-panel imager: Initial performance characterization. *Med. Phys. 27*(6): 1311–23.

Jaffray, D. A., Siewerdsen, J. H., Wong, J. W., & Martinez, A. A. (2002). Flat-panel cone-beam computed tomography for image-guided radiation therapy. *International Journal of Radiat. Oncol. Biol. Phys., 53*(5), 1337–1349.

Jaffray, D. A., Dawson, L. A. (2007). Advances in image-guided radiation therapy. *J Clin Oncol 25*(8): 938–46.

Jaffray, D. A., Lindsay, P. E., Brock, K. K., Deasy, J. O., Tome, W. A. (2010). Accurate accumulation of dose for improved understanding of radiation effects in normal tissue. *Int. J. Radiat. Oncol. Biol. Phys.* 76, S135–S139.

Jaffray, D. A. (2012). Image-guided radiotherapy: from current concept to future perspectives. *Nat Rev Clin Oncol* 9: 688–699.

Jakel, O., Kramer, M. (1998). Treatment planning for heavy ion irradiation. *Physica Medica*, 14:53–62.

Jermann, M. (2015). Particle therapy statistics in 2014. *Int. J. Part. Ther.*, 2: 50–54.

Definition of volumes. (2010). *J ICRU 10*(1):41-53.

Kamath, S., Song, W., Chvetsov, A. et al. (2011). An image quality comparison study between XVI and OBI CBCT systems. *J Appl Clin Med Phys 12*(2): 3435

Karger, C. P., Peschke, P. (2018). RBE and related modeling in carbon-ion therapy. *Phys. Med. Biol.* 63, 01TR02.

Kim, S., Yoshizumi, T. T., Toncheva, G., Yoo, S., Yin, F. F. (2008). Comparison of radiation doses between cone-beam ct and multi detector ct: Tld measurements. *Radiat Prot Dosimetry, 132*(3):339–345.

Kurz, C., Dedes, G., Resch, A., Reiner, M., Ganswindt, U., Nijhuis, R., Thieke, C., Belka, C., Parodi, K., Landry, G. (2015). Comparing cone-beam CT intensity correction methods for dose recalculation in adaptive intensity modulated photon and proton therapy for head and neck cancer. *Acta Oncol.* 54, 1651–1657.

Kurz, C. , Kamp, F. , Park, Y. , Zöllner, C. , Rit, S. , Hansen, D. , Podesta, M. , Sharp, G. C., Li, M. , Reiner, M. , Hofmaier, J. , Neppl, S. , Thieke, C. , Nijhuis, R. , Ganswindt, U. , Belka, C. , Winey, B. A., Parodi, K. and Landry, G. (2016). Investigating deformable image registration and scatter correction for CBCT-based dose calculation in adaptive IMPT. *Med. Phys., 43*: 5635-5646.

Landry, G., Dedes, G., Zollner, C., Handrack, J., Janssens, G., de Xivry, J. O., Reiner, M., Paganelli, C., Riboldi, M., Kamp, F., Sohn, M, Wilkens, J. J., Baroni, G., Belka, C., and Parodi, K. (2015). Phantom based evaluation of CT to CBCT image registration for proton therapy dose recalculation. *Phys. Med. Biol. 60*, 595–613.

Landry, G., Nijhuis, R., Dedes, G., Handrack, J., Thieke, C., Janssens, G., Orban de Xivry, J., Reiner, M., Kamp, F., Wilkens, J., J., Paganelli, C., Riboldi, M., Baroni, G., Ganswindt, U., Belka, C., and Parodi, K. (2015). Investigating CT to CBCT image registration for head and neck proton therapy as a tool for daily dose recalculation. *Med. Phys. 42*, 1354–1366.

Langen, K.M., Jones, D.T. (2001). Organ motion and its management. *Int J. Radiat. Oncol. Biol. Phys. 50*, 265–268.

Lim-Reinders, S., Keller, B. M., Al-Ward, S., Sahgal, A., Kim, A. (2017). Online adaptive radiation therapy. *Int J Radiat Oncol Biol Phys, 99*(4): 994–1003.

Mainegra-Hing, E., Kawrakow, I. (2010). Variance reduction techniques for fast monte carlo CBCT scatter correction calculations. *Phys Med Biol. 55*: 4495–4507.

Meyer M, Kalender WA, Kiriyakou Y. A fast and pragmatic approach for scatter correction in flat-detector ct using elliptic modelling and iterative optimization. Phys Med Biol. 2010;55:99–120.

Miracle, A. C., Mukherji, S. K. (2009). Conebeam CT of the head and neck, part 1: physical principles. *AJNR Am J Neuroradiol. 30*(6): 1088–95.

Moore, C.J., Amer, A., Marchant, T., Sykes, J.R., Davies, J., Stratford, J., McCarthy, C., MacBain, C., Henry, A., Price, P., Williams, P.C. (2006). Developments in and experience of kilovoltage x-ray cone beam image-guided radiotherapy. *Br J Radiol 79*(Sp. Iss. SI): S66–78.

Mori S, Zenklusen S, Knopf AC. Current status and future prospects of multi-dimensional image-guided particle therapy. *Radiol Phys Technol* 2013; 6: 249–72.

Mory, C. (2014). Cardiac C-Arm Computed Tomography. PhD thesis.

Mory, C., Janssens, G., Rit, S. (2016). Motion-aware temporal regularization for improved 4D cone-beam computed tomography. *Phys. Med. Biol. 61*(18): 6856.

Mueller, K., Yagel, R., Wheller, J.J. (1999). Fast implementations of algebraic methods for three-dimensional reconstruction from cone-beam data. *IEEE Trans Med Imaging 18*(6): 538–48.

Mueller, K., Yagel, R., Wheller, J.J. (1999). Anti-aliased three-dimensional cone-beam reconstruction of low-contrast objects with algebraic methods. *IEEE Trans Med Imaging 18*(6): 519–37.

Mukherji, S.K., Miracle, A.C. (2009). Cone-beam CT of the head and neck, Part 2: clinical applications. *Am J Neuroradiol 30*(7): 1285–92.

Nijkamp, J., Pos, F.J., Nuver, T.T., de Jong, R., Remeijer, P, Sonke, J. J., Lebesque, J. V. (2008). Adaptive radiotherapy for prostate cancer using kilovoltage cone-beam computed tomography: first clinical results. *Int J Rad Oncol Biol Phys 70*(1): 75–82.

Ning, R., Tang, X., Conover, D. (2004). X-ray scatter correction algorithm for cone beam CT imaging. *Med Phys 31*(5): 1195–202.

Niu, T., Sun, M., Star-Lack, J., Gao, H., Fan, Q., Zhu, L. (2010). Shading correction for on-board cone-beam CT in radiation therapy using planning MDCT images. *Med. Phys. 37*, 5395–5406.

Niu, T., Al-Basheer, A., Zhu, L. (2012). Quantitative cone-beam CT imaging in radiation therapy using planning CT as a prior: First patient studies. *Med. Phys. 39*, 1991–2000.

Oldham, M., Létourneau, D., Watt, L., Hugo, G., Yan, D., Lockman, D., Kim, L. H., Chen, P. Y., Martinez, A., Wong, J. W. (2005). Cone-beam-CT guided radiation therapy: a model for on-line application. *Radiother Oncol 75*(3): 271–78

Paganetti, H. (2012). Range uncertainties in proton therapy and the role of Monte Carlo simulations. *Phys. Med. Biol. 57*, R99–R117.

Pan, J., Zhou, T., Han, Y., Jiang, M. (2006). Variable weighted ordered subset image reconstruction algorithm. *Int J Biomed Imaging, 2006*: 10398.

Y.-K. Park, G. C. Sharp, J. Phillips, and B. A.Winey. (2015). Proton dose calculation on scatter-corrected CBCT image: Feasibility study for adaptive proton therapy. *Med. Phys. 42*, 4449–4459.

Particle Therapy Co-Operative Group (PTCOG), https://www.ptcog.ch/.

Patel, V. M., Maleh, R., Gilbert, A. C., Chellappa, R. (2012). Gradient-based image recovery methods from incomplete Fourier measurements. *IEEE Transactions on Image Processing, 21*(1): 94–105.

Pauwels, R. (2018). What Is CBCT and How Does It Work? *Maxillofacial Cone Beam Computed Tomography*, © Springer International Publishing.

Pawlowski, JM, Yang, ES, Malcolm, AW et al. (2010). Reduction of dose delivered to organs at risk in prostate cancer patients via image-guided radiation therapy. *Int J Rad Oncol Biol Phys 76*(3): 924–34.

M. Peroni, D. Ciardo, M. F. Spadea, M. Riboldi, S. Comi, D. Alterio, G. Baroni, and R. Orecchia. (2012). Automatic segmentation and online virtual CT in head-and-neck adaptive radiation therapy. *Int. J. Radiat. Oncol., Biol., Phys.* 84, e427–e433.

Qiu, W., Pengpan, T., Smith, N. D., Soleimani, M. (2013). Evaluating iterative algebraic algorithms in terms of convergence and image quality for cone beam CT. *Comput Methods Programs Biomed. 109*(3): 313–22.

Ramani, S., Fessler, J. A. (2012). A splitting-based iterative algorithm for accelerated statistical X-ray CT reconstruction. *IEEE Trans Med Imaging. 31*(3): 677 – 688.

Ren, D., Zhang, H., Zhang, D., Zuo, W. (2015). Fast total-variation based image restoration based on derivative alternated direction optimization methods. *Neurocomputing* 170: 201– 212.

Richter A, Hu Q, Steglich D, et al. (2008). Investigation of the usability of conebeam CT data sets for dose calculation. *Rad Oncol 3*(1): 42.

Ruhrnschopf, E.P., Klingenbeck, K. (2011). A general framework and review of scatter correction methods in x-ray cone-beam computerized tomography. Part 1: scatter correction approaches. *Med Phys. 38*: 4296.

Ruhrnschopf, E.P., Klingenbeck, K. (2011). A general framework and review of scatter correction methods in x-ray cone-beam computerized tomography. Part 2: scatter estimation approaches. *Med Phys. 38*: 5186.

Rinkel, J., Gerfault, L., Esteve, F., Dinten, J.M. (2007). A new method for x-ray scatter correction: first assessment on a cone-beam ct experimental setup. *Phys Med Biol.* 52:4633.

Rit, S., Clackdoyle, R., Keuschnigg, P., Steininger, P. (2016). Filtered backprojection reconstruction for a cone-beam computed tomography scanner with independent source and detector rotations. *Med. Phys. 43*, 2344–2352.

Rossi, S. (2015). The National Centre for Oncological Hadrontherapy (CNAO): Status and perspectives. *Phys Med. 31*(4): 333–51.

Scarfe W, Farman A. (2007). Cone beam computed tomography: a paradigm shift for clinical dentistry. *Australas Dental Prac* 102–10.

Schulze, R., Heil, U., Gross, D., Bruellmann, D. D., Dranischnikow, E., Schwanecke, U., Schoemer, E. (2011). Artefacts in CBCT: a review. *Dentomaxillofac Radiol 40*(5): 265–73.

Seco, J., Spadea, M.F. (2015). Imaging in particle therapy: state of the art and future perspective. *Acta Oncol 54*: 1254–8.

Sharpe, M.B., Moseley, D.J., Purdie, T.G., Islam, M., Siewerdsen, J. H., Jaffray, D. A. (2006). The stability of mechanical calibration for a kV cone beam computed tomography system integrated with linear accelerator. *Med Phys 33*(1): 136–44.

Skerl, D., Tomazevic, D., Likar, B., Pernus, F. (2006). Evaluation of similarity measures for reconstruction-based registration in image-guided radiotherapy and surgery. *Int J Radiat Oncol. Biol. Phys. 65*(3): 943–53.

Siewerdsen, J.H., Jaffray, D.A. (2001). Cone-beam computed tomography with a flat-panel imager: magnitude and effects of x-ray scatter. *Med Phys 28*(2): 220–31.

Siewerdsen, J.H., Moseley, D. J., Bakhtiar, B., Richard, S., Jaffray, D.A. (2004). The influence of antiscatter grids on soft-tissue detectability in cone-beam computed tomography with flat-panel detectors. *Med Phys 31*(12): 3506–15.

Siewerdsen, J.H., Daly, M.J., Bakhtiar, B., Moseley, D. J., Richard, S., Keller, H., Jaffray, D. A. (2006). A simple, direct method for x-ray scatter estimation and correction in digital radiography and cone-beam CT. *Med Phys 33*(1): 187–97.

Sonke, J., Zijp, L., Remeijer, P., van Herk, M. (2005). Respiratory correlated cone beam CT. *Med Phys 32*(4): 1176–86.

Srinivasan, K., Mohammadi, M., Shepherd, J. (2013). Cone beam computed tomography (CBCT) for adaptive radiotherapy treatment planning. *J Med Biol Eng 34*(4): 377–385.

Srinivasan, K., Mohammadi, M., Shepherd, J. (2014). Applications of linac-mounted kilovoltage Cone-beam Computed Tomography in modern radiation therapy: A review. *Pol J Radiol., 79*: 181–193.

Stankovic, U., van Herk, M., Ploeger, L. S., Sonke, J.J. (2014). Improved image quality of cone beam ct scans for radiotherapy image guidance using fiber interspaced antiscatter grid. *Med Phys. 41*(6): 061910.

Stankovic, U., Ploeger, L.S., Herk, M., Sonke, J.J. (2017). Optimal combination of anti-scatter grids and software correction for CBCT imaging. *Med Phys. 44*: 4437–4451.

Steinke, M.F., Bezak, E. (2008). Technological approaches to in-room CBCT imaging. *Australas Phys Eng Sci Med 31*(3): 167–79.

Sun, M., Star-Lack, J.M. (2010). Improved scatter correction using adaptive scatter kernel superposition. *Phys Med Biol. 55*: 6695.

Thing, R.S., Bernchou, U., Mainegra-Hing, E., Hansen, O., Brink, C. (2016). Hounsfield unit recovery in clinical cone beam CT images of the thorax acquired for image guided radiation therapy. *Phys Med Biol. 61*:5781–5802.

Tian, X., Liu, K., Hou, Y., Cheng, J., & Zhang, J. (2017). The evolution of proton beam therapy: Current and future status. *Molecular and clinical oncology*, *8*(1), 15–21.

Turbell, H. (2011). *Cone-Beam reconstruction using filtered backprojection*. PhD thesis.

Valentin, J. (2003) Relative biological effectiveness (RBE), quality factor (Q), and radiation weighting factor (wR*). ICRP Publication 92, Ann ICRP 2003. 33*:1–121.

Veiga, C., Alshaikhi, J., Amos, R., Loureno, A. M., Modat, M., Ourselin, S., Royle, R., McClelland, J. R. (2015). Cone-beam computed tomography and deformable registration-based dose of the day calculations for adaptive proton therapy. *Int. J. Part. Ther. 2*, 404–414.

Veiga, C., Janssens, G., Teng, C. L., Baudier, T., Hotoiu, L., McClelland, J. R., Royle, G., Lin, L., Yin, L., Metz, J., Solberg, T. D., Tochner, Z., Simone, C. B., McDonough, J., Teo, B. K. K. (2016). First clinical investigation of CBCT and deformable registration for adaptive proton therapy of lung cancer. *Int. J. Radiat. Oncol., Biol., Phys. 95*, 549–559.

Wei, Z., Guo-Tao, F., Cui-Li, S., Yan-Fang, W., Cun-Feng, W., Da-Quan, C., Jie-Min, Q., Xiao, T., Rong-Jian, S., Long, W. (2011). Beam hardening correction for a cone-beam CT system and its effect on spatial resolution. *Chin Phys C, 35*(10): 978

Wilson, R.R. (1946). Radiological use of fast protons. *Radiology, 47*(11): 487-491.

Yan, D., Vicini, F., Wong, J., Martinez, A. (1997). Adaptive radiation therapy. *Phys Med Biol 42*(1): 123–32.

Yan, D., Jaffray, D. A., Wong, J. W. (1999) A model to accumulate fractionated dose in a deforming organ. *Int. J. Radiat. Oncol. Biol. Phys. 44*, 665–675.

Yan, H., Cervino, L., Jia, X., Jiang, S.B. (2012). A comprehensive study on the relationship between the image quality and imaging dose in low-dose cone beam CT. *Phys Med Biol, 57*(7): 2063–80.

Yang, Y., Schreibmann, E., Li, T. (2007). Evaluation of on-board kV cone beam CT (CBCT)-based dose calculation. *Phys Med Biol, 52*: 685–705.

Yao, W., Krasin, M. J., Farr, J. B., Merchant, T. E. (2018). Feasibility study of range-based registration using daily cone beam CT for intensity-modulated proton therapy. *Med Phys. 45*(3): 1191–1203.

Yoo, S., Kim, G., Hammoud, R. et al. (2007). A quality assurance program for the On-Board Imager®. In: Magjarevic R, Nagel JH (eds.), *World Congress on Medical Physics and Biomedical Engineering 2006. IFMBE Proceedings. 14*. Springer Berlin Heidelberg.

Zhao, W., Vernekohl, D., Zhu, J., Wang, L., Xing, L. (2016). A model-based scatter artifacts correction for cone beam CT. *Med Phys. 43*: 1736–1753.

Zhu, L., Bennett, N.R., Fahrig, R. (2006). Scatter correction method for x-ray ct using primary modulation: theory and preliminary results. *IEEE Trans Med Imag. 25*:1573.

Zhu, L., Wang, J., Xing, L. (2009). Noise suppression in scatter correction for cone-beam CT. *Med Phys, 36*(3): 741–52.

Zhu, L., Xie, Y.Q., Wang, J., Xing, L. (2009). Scatter correction for cone-beam CT in radiation therapy. *Med Phys 36*(6): 2258–68.

Zollner, C., Rit, S., Kurz, C., Vilcher-Freixas, G., Kamp, F., Dedes, G., Belka, C., Parodi, K, Landry, G. (2017). Decomposing a prior-CT-based cone-beam CT projection correction algorithm into scatter and beam hardening components. *Phys Imaging Radiat Oncol. 3*:49–52.